PHOTONIC CRYSTALS AS FUNCTIONAL MIRRORS FOR SEMICONDUCTOR LASERS

Stephen Arthur Moore

A Thesis Submitted for the Degree of PhD
at the
University of St. Andrews

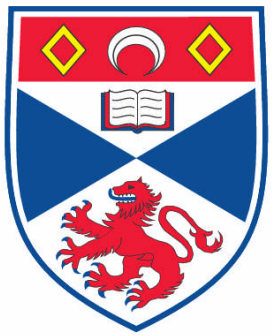

2008

Photonic Crystals as Functional Mirrors for Semiconductor Lasers

Stephen A. Moore

Thesis submitted for the degree of Doctor of Philosophy

September 1, 2008

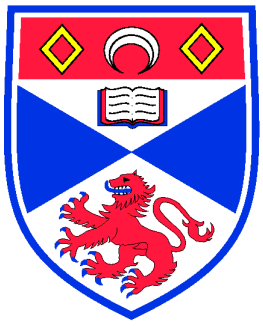

University of St Andrews

for my parents, Maurice and Victoria Moore

DECLARATIONS

I, Stephen A. Moore, hereby certify that this thesis, which is approximately 40000 words in length, has been written by me, that it is the record of work carried out by me and that it has not been submitted in any previous application for a higher degree.

I was admitted as a research student in September, 2004 and as a candidate for the degree of Doctor in Pholosophy in September, 2004; the higher study for which this is a record was carried out in the University of St Andrews between 2004 and 2008.

Stephen A. Moore July 2008

I hereby certify that the candidate has fulfilled the conditions of the Resolution and Regulations appropriate for the degree of Doctor in Philosophy in the University of St Andrews and that the candidate is qualified to submit this thesis in application for that degree.

Thomas F. Krauss July 2008

In submitting this thesis to the University of St Andrews we understand that we are giving permission for it to be made available for use in accordance with the regulations of the University Library for the time being in force, subject to any copyright vested in the work not being affected thereby. We also understand that the title and the abstract will be published, and that a copy of the work may be made and supplied to any bona fide library or research worker, that my thesis will be electronically accessible for personal or research use unless exempt by award of an embargo as requested below, and that the library has the right to migrate my thesis into new electronic forms as required to ensure continued access to the thesis. We have obtained any third-party copyright permissions that may be required in order to allow such access and migration, or have requested the appropriate embargo below. The following is an agreed request by candidate and supervisor regarding the electronic publication of this thesis:

Access to Printed copy and electronic publication of thesis through the University of St Andrews.

Stephen A. Moore Thomas F. Krauss July 2008

ACKNOWLEDGMENTS

I would like to thank my supervisor Prof. Thomas Krauss for giving me the opportunity to undertake this research and for his constant guidance and input.

I would also like to thank the current and past members of the Microphotonics Research Group who helped create a friendly and stimulating research environment. In particular, I would like to thank Dr Liam O'Faolain, Dr Andreas Vasdekis, Dr Tim Karle, Dr Michael Flynn and Dr Tom White for their time and contributions. I would also like to thank Dr David O'Brien, Mr Christopher Reardon, Dr Douglas M^{c}Robbie, Dr Michael Settle and Dr Steven Neil for their help, assistance and suggestions.

Particular thanks goes to Mr George Robb and Mr Steven Balfour for their essential work of maintaining a plethora of laboratory equipment.

I am also grateful to EPSRC for their generous funding that allowed me to undertake this research and helps keep the UK at the forefront of scientific research.

Lastly I would like to thank Mum, Dad, Claire and Jenny for their never ending encouragement and support.

ABSTRACT

In recent years, interest has grown in the research fields of semiconductor lasers and photonic crystals. This thesis looks at integrating photonic crystals into existing semiconductor laser technology to act as functional laser mirrors.

The majority of the research is conducted on a quantum-dot material system. The surface recombination velocity of a GaAs based quantum-dot material is shown to be a similar value to InP material. This allows the creation of fine photonic crystal structures in the laser design without high threshold current penalties.

The spectral reflection properties of a one dimensional photonic crystal is studied and found to be an unsuitable candidate for a stand-alone laser mirror, due to its low reflectivity.

A two-dimensional photonic crystal W3 defect waveguide is successfully integrated as a quantum-dot laser mirror. Single fundamental mode output is achieved with a typically multi-mode 20 μm wide laser mesa, highlighting the mode selective property of the mirror.

A similar two-dimensional mirror is studied for its potential as a dispersion compensating mirror for mode-locked lasers. Initial theoretical analysis shows pulse compression for a suitably designed mirror. Experimental continuous-wave results for the same mirror structure demonstrate the tuning of mirror reflectivity with photonic crystal hole radius.

A hybrid silicon-organic photonic crystal laser is demonstrated with output in the visible spectrum. This design is a new type of silicon emitter.

PUBLICATIONS ARISING FROM THIS WORK

Written Publications

- S. A. Moore, L. O'Faolain, T. P. White and T. F. Krauss, "Photonic crystal laser with mode selective mirrors," Optics Express **16,** 1365–1370 (2008).
- S. A. Moore, L. O'Faolain, M. A. Cataluna, M. B. Flynn, M. V. Kotlyar and T. F. Krauss, "Reduced surface sidewall recombination and diffusion in quantum-dot lasers," Photonics Technology Letters **8,** 1861–1863 (2006).
- A. E. Vasdekis, S. A. Moore, A. Ruseckas, T. F. Krauss, I. D. W. Samuel and G. A. Turnbull, "Silicon based organic semiconductor laser," Applied Physics Letters **91,** 051124 (2007).
- "Silicon/organic hybrid laser produces red light," Laser Focus World **43,** (10), 37–41 (2007).
- "Organic semiconductors aid quest for silicon laser," Optics & Lasers Europe **154,** 21–24 (2007).

Conferences

- S. A. Moore, T. Stomeo, L. OFaolain, M. Kamp, H. Benisty and T. F. Krauss, "Wavelength and mode control in semiconductor lasers with photonic crystal waveguides," LPHYS, Trondheim (2008).
- S. A. Moore, L. O'Faolain, M. A. Cataluna, M. V. Kotlyar, N. Tripathi, R. Wilson and T. F. Krauss, "Fabrication Techniques for Active Photonic Crystal Devices," PECS VI, Crete (2005).

- S. A. Moore, L. OFaolain, T. Karle and T. F. Krauss, "Monolithic Integration of a Semiconductor Optical Amplifier with Periodic Passive Structures," EPIXnet Winterschool, Pontresina (2006).

- S. A. Moore, L. OFaolain, T. Karle and T. F. Krauss, "Integration of Active and Periodic Passive Structures," Rank Prize Awards, Lake District (2006).

- A.E. Vasdekis, S.A. Moore, A. Ruseckas, T.F. Krauss, I.D.W. Samuel and G.A. Turnbull, "An Organic Semiconductor Laser on Silicon," SPIE Photonics Europe, Stasbourg (2008).

CONTENTS

1. INTRODUCTION

Semiconductor lasers are the most common type of laser in production today with applications ranging from the simple laser pointer to optical storage in CD and DVD ROMs to light sources for telecommunications. Some applications require just a simple directional beam whereas others require stringent spectral and modal properties. The first laser diodes were fabricated almost 50 years ago [1, 2, 3] and the field has grown steadily since. One of the more recent advances has been the development of quantum-dot laser diodes in the mid 1990s which has resulted in record low thresholds.

The field of photonic crystal research has also advanced significantly in the past decade with applications including high Q cavities, slow light research, photonic circuits and photonic crystal lasers.

This report explores the functionality that a photonic crystal can provide as a semiconductor laser mirror. By careful design, the photonic crystal mirror can provide useful spectral and modal properties in addition to reflection. Before I begin, I give a brief overview of the field of photonic crystal lasers.

1.1 Photonic Crystal Lasers - State of the Art

In 1996, my supervisor, Thomas Krauss, showed that two-dimensional photonic crystals with a band-gap at operational wavelengths as low as 800 nm could be fabricated by etching holes into a semiconductor waveguide material [4](figure 1.1). The waveguide structure provides optical confinement in the transverse plane, negating the necessity of a three dimensional crystal. This development opened up the possibility of the integration of such structures with other optoelectronic devices, such as semiconductor lasers. Soon after, the use of a bulk two dimensional photonic crystal as a semiconductor laser mirror was first demonstrated [5]. They used a hexagonal lattice of air holes in a GaAs/AlGaAs quantum-well material as one mirror of an

edge emitting laser. They estimated a modal reflectivity of 50 % for the crystal. Simulations have shown that this reflectivity can be increased to almost 100 % [6]. However, Krauss et al. also showed that a one-dimensional deeply

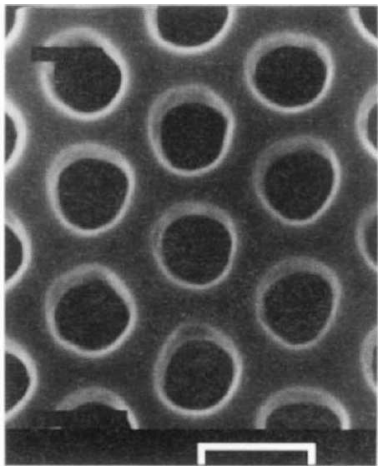

Fig. 1.1: Scanning electron microscope (SEM) image of air holes in an AlGaAs waveguide, taken from the first demonstration of a two dimensional photonic crystal band gap at near-infrared wavelengths [4].

etched PBG structures could perform equally well as a laser mirror [7]. This implied that for a high reflecting laser mirror, a simple deeply etched Bragg mirror would suffice. However, two-dimensional crystals still have significant potential for spectrum and mode control due to their high design flexibility.

The PBG mirrors discussed above are broadband, that is, they will reflect any mode with a frequency that lies within the band-gap. The high index contrast required for the photonic crystal also supports multiple transverse modes in the laser ridge.

A photonic crystal defect waveguide is formed when a row of holes (or rods) is removed from a perfect lattice. Lasers incorporating such defect structures were first reported in 2002 by Happ et al [8]. They integrated a W3 (three missing rows of holes) and a W5 into a as-cleaved facet laser cavity (figure 1.2). This formed a coupled cavity laser that produced single longitudinal mode output with a 35 dB side-mode suppression ration (SMSR). However, the device did not address the multiple transverse mode behaviour of deeply etched laser waveguides.

An InP mode-selective photonic crystal laser was demonstrated in more re-

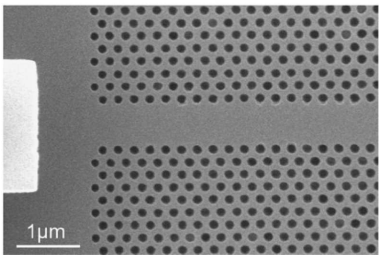

Fig. 1.2: SEM image of a ridge waveguide butt coupled to a W3 photonic crystal waveguide, taken from [8].

cent work [9, 10]. The design included a photonic crystal defect waveguide that acts as a distributed feedback component and a PBG bulk photonic crystal end mirror (figure 1.3). The devices exhibit single transverse mode behaviour as only the fundamental mode is reflected by the photonic crystal defect waveguide. The low surface recombination velocity of InP allows the fabrication of deeply etched holes close to the narrow gain section without compromising device performance. However, the narrow width of the gain section makes fabrication of the top contact difficult and devices have only been shown to lase under pulsed excitation.

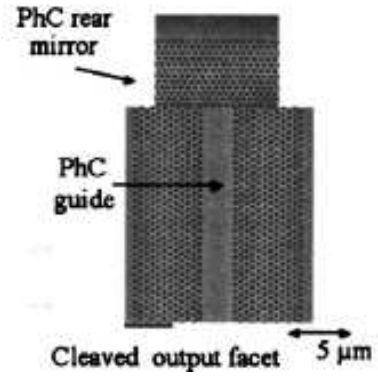

Fig. 1.3: SEM overview of device structure used in [9].

Lasers incorporating photonic crystal point defect structures have also been developed. In addition to high reflectivity, these defect structures can introduce modal filtering to a laser device. Lasing from a photonic crystal single point-defect was first demonstrated via optical pumping, in 1999 [11]. There

has been much further research into these devices [12]. This type of laser potentially exhibit a very low threshold current, but is of little relevance to the large area devices studied throughout this report.

1.2 Research Outline

The above research tends to focus on the drive for low threshold, single mode lasers for the specific application miniaturised light sources for photonic circuits. The research in this report takes a slightly different approach with the question: What functionality can photonic crystals add to existing semiconductor laser designs?

1.2.1 Quantum-dot Material

The majority of the above research was conducted on an InP material system. This is because InP has a low surface recombination value [13]. It is necessary to etch photonic crystal holes through the waveguide layer and this creates a large surface to volume ratio in the light guiding region. For active photonic crystal devices, it is therefore desirable to use a material with a low surface recombination velocity [14]. InP has generally been preferred to GaAs for this reason. Previous work [15, 16] has observed reduced surface recombination in quantum-dot material compared with quantum-wells. In chapter 6 of this report, I quantify this reduction and provide a value of surface recombination velocity and diffusion length in a GaAs based quantum-dot material. The values are similar to InP, thus increasing the potential for photonic crystal lasers in a GaAs based material.

1.2.2 Single transverse Mode Operation

One disadvantage of deeply etching through the waveguide region in a semiconductor laser is that it will support more transverse modes. As explained in chapters 3 and 5 a higher refractive index contrast at the edge of the laser mesa[1] will support more waveguide modes. The only ways to counteract this

[1] A deeply etched laser ridge is referred to as a laser mesa.

are to decrease the frequency (not an option) or decrease the dimensions of the laser mesa. The dimensions required to ensure single mode operation of a laser mesa (sub-micron) introduce new problems such as high optical losses and increased surface recombination.

In chapters 8 and 9 I show that it is possible to develop single transverse mode mesa lasers without the need for sub-micron dimensions, by the use of a mode-selective photonic crystal mirror. The lack of restriction in device dimensions allows the creation of wide, high power single-mode mesa lasers.

1.2.3 Pulse Compression

Another functionality explored is the potential for pulse compression in mode-locked lasers. Photonic crystals mirrors can provide a wavelength specific reflection. The spectral tuning of such a reflection peak can create a dispersion compensating laser mirror via group delay dispersion. In semiconductor mode-locked lasers the laser pulse is positively chirped and material dispersion leads to broad pulses with a leading red edge. A dispersion compensating mirror would correct for this dispersion by reflecting the trailing blue edge at the front of the mirror and the leading red edge at the rear. In this manner, the red edge has a longer round trip time leading to negative group delay dispersion.

A typical mode-locked quantum-dot laser pulse has a duration of a few ps and a bandwidth of a few nm. If we take a 3 ps, 5 nm pulse and assume a pulse bounces 1.5 times on average, we can quickly calculate the design requirements of the mirror. We want to delay the red edge by 3 ps i.e. 2 ps per round trip. The required mirror length is then:

$$l = \frac{c\Delta t}{2n} \tag{1.1}$$

$$= \frac{3 \times 10^8 \times 2 \times 10^{-12}}{2 \times 3.4}$$

$$= 88\ \mu m \tag{1.2}$$

Thus the reflection peak of the photonic crystal mirror needs to tune by 5 nm over the 88 μm length of the mirror. The crystal will be defined with electron-beam lithography which has a minimum grid size of 1 nm. As a consequence, it will be physically impossible to chirp the reflection smoothly and so we

will require a stepped change. If we use some crystal parameter, x, to tune the spectrum, such as hole radius or period, the tuning rate will determine the maximum number of chirp steps in the mirror. Obviously the higher the number of steps, the closer the approximation of a smooth chirp. Assuming a chirp step in x of 1 nm, the number of steps will then be given by:

$$N_{steps} = \frac{5}{d\lambda/dx} \tag{1.3}$$

over a length of 88μm.

In chapter 10 I theoretically show pulse compression via group delay dispersion by performing computational simulations on a photonic crystal mirror. Some initial experimental results are also presented.

1.2.4 High Reflectivity Mirrors

High reflectivity is a desirable property for most laser mirrors. Furthermore, a variable reflectivity that can be defined by mirror design is particularly advantageous. Chapters 9 and 10 consider the effect of photonic crystal mirror design on reflectivity. In chapter 10, the reflectivity of a two dimensional photonic crystal mirror is experimentally shown to vary with hole radius in the crystal.

1.2.5 Thesis Overview

Chapters 2 and 3 give the reader an introduction to semiconductor lasers and photonic crystals. Chapter 4 then details the experimental techniques used to fabricate the devices produced for this report. A brief overview of quantum-dot theory is given at the beginning of chapter 5 before some characterisation of the material used in this report. As mentioned above, chapter 6 then further characterises the material, specifically studying surface recombination and carrier diffusion. A one dimensional photonic crystal mirror is the subject of study of chapter 7 and some lasing results are reported. Chapters 8 and 9 study a two-dimensional photonic crystal mirror and its ability to produce single transverse mode output. The potential of a similar mirror to provide pulse compression is explored in chapter 10 along with some interesting continuous

wave results. Chapter 11 changes track a little and describes some collaborative work on a hybrid silicon–organic, one dimensional photonic crystal laser. Conclusions and future potential are then described.

2. SEMICONDUCTOR LASERS

2.1 Introduction

This chapter gives a brief overview of semiconductor lasers. Continuous wave analysis including rate equations and steady state analysis is presented. This is followed by an overview of mode locked semiconductor lasers. The different types of mode locking are introduced and the major parameters affecting mode locking in semiconductor lasers are described in detail. For a more comprehensive overview of semiconductor lasers, there are many good books available [13, 17].

2.2 Continuous Wave Diode Lasers - A Quick Recap

Many important continuous-wave (cw) results (chapters 6, 7, 9 and 10) are described in this report. The basics of cw semiconductor laser diodes is revised here.

2.2.1 Rate Equations

Carrier Density

In a semiconductor laser, the free carrier density represents the available population inversion. The carrier concentration is dependent on the generation of carriers via electrical pumping and the loss of carriers via recombination and diffusion processes:

$$\frac{dN}{dt} = \Lambda - R \tag{2.1}$$

where N is the carrier concentration, Λ is the pumping rate and R is the recombination rate. The electrical pumping rate and recombination rate can

be written as:

$$\Lambda = \frac{\eta_i I}{qV} \tag{2.2}$$

$$R = \frac{N}{\tau} + R_{st} \tag{2.3}$$

where η_i is the internal quantum efficiency, I is the pump current, q is the electronic charge and V is the volume of the active region. R_{st} is the stimulated emission recombination rate and τ is the carrier lifetime in the absence of photons. Putting the above equations together, we get the carrier density rate equation:

$$\frac{dN}{dt} = \frac{\eta_i I}{qV} - \frac{N}{\tau} - R_{st} \tag{2.4}$$

Photon Density

Photons are generated via spontaneous and stimulated emission in the cavity and lost by absorption, scattering and output coupling through the mirrors. This loss can be grouped together as a photon lifetime, τ_p that represents their exponential decay:

$$\frac{dP}{dt} = \Gamma R_{st} + \Gamma \beta_{sp} R_{sp} - \frac{P}{\tau_p} \tag{2.5}$$

where P is the photon density, Γ is the optical confinement factor that represents the optical mode overlap with the active region and β_{sp} is the spontaneous emission factor equal to the reciprocal of the number of optical modes in the bandwidth of the spontaneous emission. Equations 2.4 and 2.5 are the two coupled rate equations that can be solved for the steady state (cw) and dynamic responses of a laser diode.

2.2.2 Threshold Gain

The simple definition of laser threshold is the point when the round trip gain first equals the round trip loss, that is a round trip gain (or loss) factor of 1:

$$P_0 \times Roundtripgain \times Roundtriploss = P_0$$

The round trip cavity gain and losses are written as exponential terms as they are embedded in the complex part of the optical mode propagation constant.

The mirror reflectivities must also be included as a factorial loss term. Our expression becomes:

$$r_1 r_2 e^{(\Gamma g_{th} - \alpha_i).2L} = 1 \tag{2.6}$$

where r_1 and r_2 are the two mirror reflectivities, g_{th} is the material gain at threshold and α_i is the internal modal loss. A more appropriate form of equation 2.6 is:

$$\Gamma g_{th} = \alpha_i + \frac{1}{L} \ln\left(\frac{1}{R}\right) \tag{2.7}$$

where $R = r_1 r_2$ is the mean mirror reflectivity. The second term on the right hand side is sometimes abbreviated as the mirror loss α_m.

2.2.3 Some Steady State Analysis

In steady state operation the rate equations defined above both equal zero. Another condition of steady state is that the gain must equal the threshold value. If it were higher, the field amplitude would increase indefinitely and if it were lower the field would decrease to zero. The gain is directly dependent on the carrier density implying that the steady-state carrier density must also equal it's threshold value. In summary:

$$g(I > I_{th}) = g_{th}$$
$$N(I > I_{th}) = N_{th}$$

These conditions imply that any additional carrier injection goes directly into stimulated emission. To show this explicitly, we consider the coupled rate equations derived above.

Just below threshold, we can assume $R_{st} \sim 0$ and $dN/dt = 0$ (steady-state condition). Equation 2.4 becomes:

$$\frac{\eta_i I_{th}}{qV} = \frac{N_{th}}{\tau} \tag{2.8}$$

Substituting this threshold condition back into equation 2.4 for currents above threshold we obtain a new carrier rate equation:

$$\frac{dN}{dt} = \eta_i \frac{I - I_{th}}{qV} - R_{st} \qquad (I > I_{th}) \tag{2.9}$$

and in steady-state

$$R_{st} = \eta_i \frac{I - I_{th}}{qV} \tag{2.10}$$

R_{st} is not very meaningful, but we can define it in terms of the photon density, P. For a small length of gain, Δz, the increase in P is simply:

$$\begin{aligned} P + \Delta P &= P e^{g\Delta z} \\ &= P(1 + g\Delta z) \ \ (\Delta z \ small) \end{aligned}$$

Using $\Delta z = v_g \Delta t$ where v_g is the group velocity we can write

$$R_{st} = \left(\frac{dP}{dt}\right)_{gen} = v_g g P \tag{2.11}$$

Substituting this into equation 2.10 we obtain an expression for the steady state photon density above threshold:

$$P = \frac{\eta_i (I - I_{th})}{q v_g g_{th} V} \tag{2.12}$$

From this expression, we can obtain the optical output power as a function of drive current above threshold. To do this, we multiply P by the volume of the cavity, V_{cav}, and by the photon energy $h\nu$ where h is Plank's constant and ν is the operating frequency. This gives us the optical energy inside the cavity. To convert this to an optical output power we multiply by the rate of energy loss through the mirrors, $v_g \alpha_m$. The output power is therefore:

$$P_{out} = v_g \alpha_m h\nu V_{cav} P \tag{2.13}$$

Substituting for P and g_{th} using equations 2.12 and 2.7 and recognising that $V/V_c = \Gamma$ we arrive at an expression for the output power in terms of drive current above threshold:

$$P_{out} = \frac{\eta_i \alpha_m}{\alpha_i + \alpha_m} \frac{h\nu}{q} (I - I_{th}) \tag{2.14}$$

The term

$$\eta_d = \frac{\eta_i \alpha_m}{\alpha_i + \alpha_m} \tag{2.15}$$

is referred to as the differential quantum efficiency and is the number of output photons for every input electron above threshold. η_d can be found experimentally from the slope of a laser P-I curve above threshold (see figure 2.1), although more commonly we refer to the slope efficiency of a laser:

$$\frac{dP_0}{dI} = \frac{h\nu}{q}.\eta_d \qquad (I > I_{th}) \tag{2.16}$$

which is just the slope of the P-I curve above threshold. For the P-I curve shown in figure 2.1 the slope efficiency is approximately 0.6 and the operating wavelength is 1280 nm. Hence we can easily calculate the differential quantum efficiency $\eta_d = 0.62$. The remaining 38 % of carriers recombine in a non-radiative manner such as Auger recombination and surface recombination (the main focus of chapter 6).

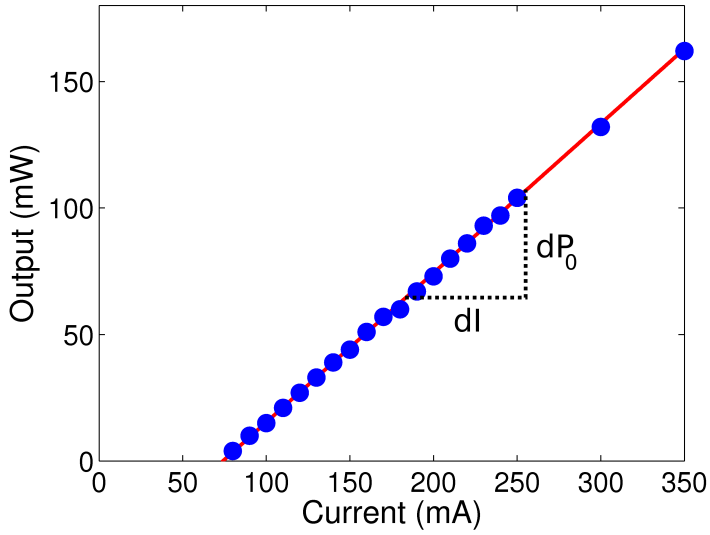

Fig. 2.1: Example of a laser diode P-I curve.

To summarize this section, the laser rate equations have been derived along with the threshold gain condition. Some steady state analysis of these equations has yielded an analytical expression for the slope efficiency obtained from a P-I curve.

2.3 Semiconductor Mode-locked Lasers

One goal in this project is to create a dispersion compensating mirror for a mode-locked semiconductor laser. The theory of passive mode-locking in semiconductor lasers is introduced below..

2.3.1 Basics

Mode-locking is a technique used to produce a train of laser pulses by inducing a fixed phase relationship between the laser cavity's longitudinal modes. This fixed phase relationship leads to periodic constructive interference of the longitudinal modes with a repetition rate, f_{rep} equal to the inverse of the cavity round trip time:

$$f_{rep} = \frac{c}{2nL} \tag{2.17}$$

The laser is said to be phase locked or mode locked. Mode locking has been the most successful technique for producing short laser pulses and high repetition rates in both semiconductor [18] and solid-state laser systems [19].

There are three main methods of mode-locking semiconductor lasers: active [20], passive [21] and hybrid [22]. Active mode locking involves using an RF signal to modulate the gain at the repetition frequency of the cavity. This method produces low jitter pulses, but the modulation electronics becomes complicated at high repetition rates. Passive mode-locking is the method studied in this work and involves using a saturable absorber within the cavity. The saturable absorber acts to encourage pulsed operation over cw. The fabrication and operation is much easier than with active mode-locking and the repetition rate is determined solely by the cavity length. Hybrid mode-locking is, as the name suggests, a combination of the active and passive techniques. An RF signal is used to kick-start pulsing after which the saturable absorber provides further pulse shaping and shortening.

2.3.2 Passive Mode Locking - Desirable Device Characteristics

The basic layout of a passively mode-locked laser is shown in figure 2.2(a). In a semiconductor laser, the saturable absorber is formed by the electrical isolation of a small section of the waveguide as shown in figure 2.2(b). This section is

then left unpumped or reversed biased to create a saturable absorber [23]. The

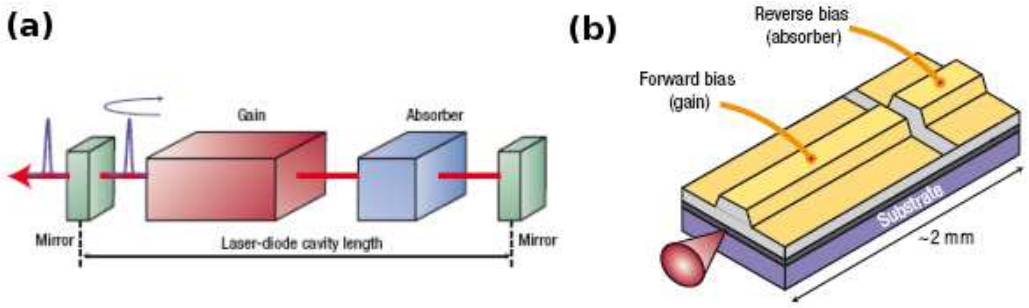

Fig. 2.2: (a) Schematic of basic layout of a passively mode locked laser and (b) typical mode locked semiconductor laser schematic showing gain and absorber sections. (Images taken from [24]).

main parameters that influence passive mode locking in semiconductor lasers are addressed below:

Gain Bandwidth

The duration of a pulse with a given spectral bandwidth is transform limited by the time-bandwidth product[1][25]:

$$\Delta t \Delta \nu = 0.44 \tag{2.18}$$

The time-bandwidth product is a direct consequence of Heisenberg's uncertainty principle and implies that for short pulse durations a broad pulse spectrum is required. A broad gain spectrum is therefore desirable to achieve this. However, it should be noted that a broad gain spectrum does not ensure a broad pulse spectrum. An effect called spectral narrowing [25] occurs during lasing and can produce pulses of a significantly narrower spectrum than the gain bandwidth.

[1] The time-bandwidth product is dependent on pulse shape and the value of 0.44 assumes a gaussian pulse profile.

Carrier Dynamics

The speed of the gain and saturable absorber recovery times are very important parameters in passive mode locked semiconductor lasers.

The absorber recovery time should be shorter than the cavity round trip time (which determines repetition rate) so that the absorber has recovered to a state of maximum attenuation before each successive pulse. A very fast absorber can also attenuate the trailing edge of each pulse leading to a further reduction in pulse duration. In semiconductor mode locked lasers, the absorber recovery time can be reduced by applying a reverse bias to the saturable absorber. Thomson et al. confirmed these principles by showing an exponential decrease in pulse duration with increasing saturable absorber reverse bias [26].

The gain recovery should also be shorter than the cavity round trip time to ensure a state of maximum gain upon arrival of each successive pulse. However, it is desirable for the gain recovery time to be longer than the pulse duration. This will lead to less amplification of the pulse's trailing edge and further pulse shortening [27].

A schematic of the gain and absorption dynamics in a mode locked laser are shown in figure 2.3. The figure shows gain and absorption recovery times shorter than the repetition time with the gain recovery time much longer than the pulse duration. The resulting net gain window and output intensity are also shown.

Saturation

The gain saturation energy, E^g_{sat}, of a material is defined as

$$E^g_{sat} = \frac{h\nu A}{\frac{dg}{dN}} \tag{2.19}$$

where h is Plancks constant, ν is the laser frequency, A is the mode cross-sectional area, g is the modal gain and N is the carrier density. g can be replaced by a in equation 2.19 to give an expression for the absorber saturation energy, E^a_{sat}. For successful passive mode locking, the absorption of the saturable absorber must saturate at a lower energy than the gain of the gain medium [28]. The higher the ratio of E^g_{sat}/E^a_{sat}, the more stable the mode

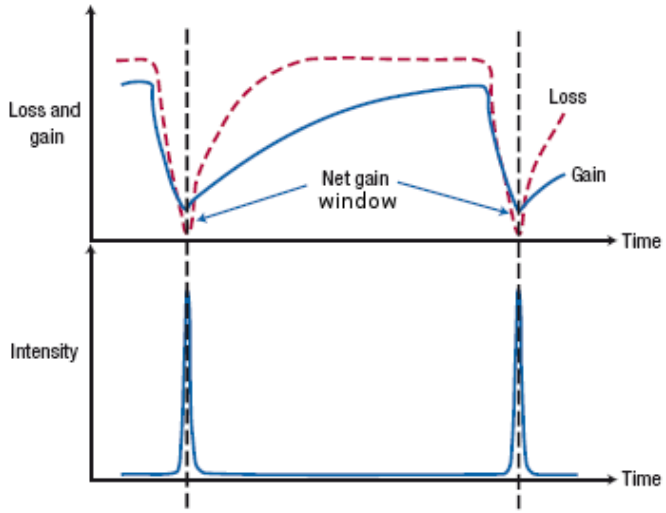

Fig. 2.3: Schematic of gain and loss evolution, and resulting output intensity, in passive mode locked semiconductor laser. (Taken from [24]).

locking is. To satisfy this condition, examination of equation 2.19 implies

$$\frac{da}{dN} > \frac{dg}{dN} \tag{2.20}$$

is necessary for successful mode-locking. Thankfully in semiconductor lasers, differential gain (loss) decreases with increasing carrier density [13]. This is particularly true for quantum-well and quantum-dot material in which the gain versus carrier density relationship takes on a logarithmic form[2] as seen in figure 2.4.

The mode cross-sectional area, A, can also be useful in reducing the saturation energy of saturable absorbers. A is typically the same in both the gain and saturable absorber sections. However, mode-locking has been achieved in flared lasers, where the gain section is a flared waveguide and the saturable absorber is a narrow single-mode waveguide [26]. This has the added advantage of providing more gain (and hence higher output power) while remaining single-mode due to the narrow absorber section. This flared waveguide concept is explored in more detail in chapter 10 of this thesis.

[2] An ideal quantum–dot gain profile would be a series of delta functions like the density of states, however in reality it takes a logarithmic profile (chapter 5).

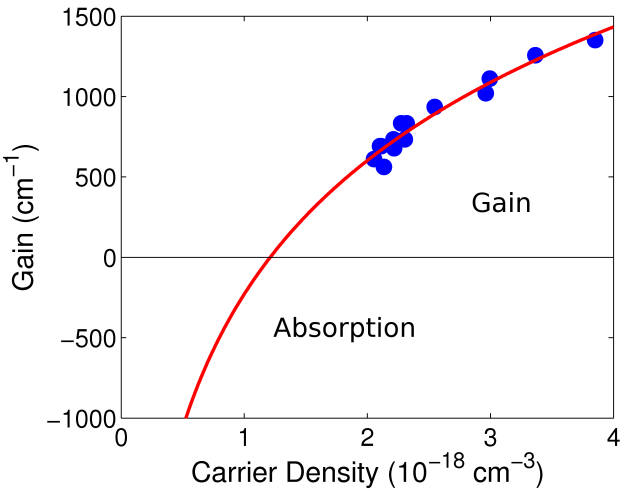

Fig. 2.4: Variation of differential gain with carrier density (Taken from chapter 6).

Self Phase Modulation

Self-phase modulation (SPM) occurs in a medium when a high energy pulse of light induces a refractive index change in the medium. This dynamic index change alters the phase of the pulse leading to spectral broadening.

The refractive index change occurs in solid state lasers and optical fibres due to the nonlinear optical Kerr effect. In solid state lasers, the optical Kerr effect can be used to produce ultra-short pulses via Kerr lens mode-locking [19]. The origin of the refractive index change is different in semiconductors and arises from changes in carrier density due to gain depletion. The effect is described by the linewidth enhancement factor:

$$\alpha = -\frac{4\pi}{\lambda_0}\frac{\frac{dn}{dN}}{\frac{dg}{dN}} \tag{2.21}$$

where λ_0 is the free space wavelength and n is the refractive index of the material. We know from figure 2.4 that dg/dN is positive. Equation 2.21 then implies that dn/dN is negative[3]. The leading edge of an incident pulse will deplete the carrier density (dN/dt negative) and therefore lead to an increase in refractive index ($dn/dt = dn/dN \times dN/dt$ is positive). To see how this leads to spectral broadening of the pulse we consider the simple example of a plane

[3] In general α is a positive constant.

wave:

$$E(x,t) = E_0 e^{i(\omega_0 t - kx)} \tag{2.22}$$

where ω_0 is the free space angular frequency and k is the wave-vector equal to $2\pi n/\lambda_0$. The frequency of the pulse at a given time, t, is given by the time derivative of the phase:

$$\begin{aligned} \omega_0(t) &= \frac{d}{dt}\{\omega_0 t - kx\} \\ &= \omega_0 - \frac{\omega_0}{c}\frac{dn}{dt}x \end{aligned} \tag{2.23}$$

So for a positive value of dn/dt we get a decrease in frequency across the pulse with the central section of the pulse experiencing the biggest shift (dn/dt maximum).

At first sight, SPM seems like a useful effect for producing short pulses. The broader pulse spectrum allows the production of shorter pulse durations as described by equation 2.18. However, there is a catch: dispersion. Semiconductors exhibit strong positive material dispersion and so the blue pulse components will travel slower than the red components leading to temporal broadening of the pulse. However if we can provide suitable dispersion compensation we can utilise the extra bandwidth provided by SPM to produce short pulses. 200 fs pulses have been produced using dispersion compensation to compress the output pulses outside the laser cavity [29, 30]. One goal of this project is to provide similar dispersion compensation "on chip" by the use of photonic crystal mirrors that possess negative group delay dispersion (GDD).

2.4 Summary

This chapter has given a brief overview of semiconductor laser theory related to my research. The rate equations and some steady-state cw analysis was derived. Mode-locking in semiconductors was introduced and the main parameters effecting it were described. These include, gain bandwidth, recovery times, saturation energies and self-phase modulation (SPM).

3. PHOTONIC CRYSTALS

3.1 Introduction

This chapter is intended to provide the reader with a brief introduction to photonic crystals and their application as laser mirrors. A more thorough description is available in a variety of good texts [31, 32]. The chapter is laid out as a progression from the simplest of systems – a uniform dielectric medium – through to two-dimensional photonic crystals. The chapter begins with Maxwell's equations and an analytical analysis of wave propagation in an isotropic material and then a slab waveguide. After this photonic crystals are introduced with a more conceptual approach.

3.2 Some Fundamentals

We start with Maxwell's equations:

$$\nabla.D(r,t) = \rho(r,t) \tag{3.1}$$

$$\nabla.B(r,t) = 0 \tag{3.2}$$

$$\nabla \times H(r,t) = \frac{dD(r,t)}{dt} + J(r,t) \tag{3.3}$$

$$\nabla \times E(r,t) = -\frac{dB(r,t)}{dt} \tag{3.4}$$

where E and H are the electric and magnetic field vectors, D and B are the electric and magnetic displacement vectors, J is the electric current density and ρ is the charge density. Here we can assume ρ and J are both zero and relate E and D via $D = \epsilon(r)E$[1] and B to H via $B = \mu_0 H$[2] and arrive at a

[1] Here we assume the materials are low loss (ϵ real) and operating in the linear regime.
[2] We further assume the materials involved are non magnetic.

simpler form of the equations:

$$\nabla.\epsilon(r)E(r) = 0 \tag{3.5}$$

$$\nabla.H(r) = 0 \tag{3.6}$$

$$\nabla \times H(r,t) = \epsilon\frac{dE(r,t)}{dt} \tag{3.7}$$

$$\nabla \times E(r,t) = -\mu\frac{dH(r,t)}{dt}. \tag{3.8}$$

3.3 Wave Propagation in Isotropic Media

For an isotropic medium we can assume that ϵ is a scalar constant and for propagation in the z direction we can assume $d/dx = d/dy = 0$ in equations 3.7 and 3.8. Expanding the two equations into their cartesian components, we can then easily show that

$$\frac{d^2E_x}{dz^2} = \mu\epsilon\frac{d^2E_x}{dt^2} \tag{3.9}$$

which is recognisable as the wave equation. A standard solution to the wave equation is a plane wave:

$$E_x = E_0e^{i(\omega t-kz)} \tag{3.10}$$

where ω is the angular frequency and k is the wave-vector. The velocity of the plane wave is simply given by:

$$v = \frac{\omega}{k} = \frac{1}{\sqrt{\mu\epsilon}}. \tag{3.11}$$

In a vacuum, where $\mu = \mu_0, \epsilon = \epsilon_0$, this velocity is c. In a dielectric medium, $v = c/n$, where $n = \sqrt{\epsilon/\epsilon_0}$ is the index of refraction. Equation 3.11 gently introduces us to the ω–k dispersion diagram. The dispersion diagram is a useful way of plotting a systems response to electromagnetic radiation. Figure 3.1 shows the dispersion diagram for an isotropic medium. The response of the medium is simply a linear relationship between ω and k with gradient c/n.

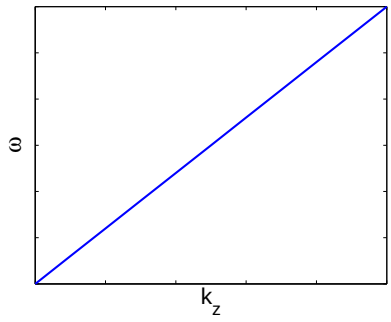

Fig. 3.1: Dispersion diagram for an isotropic medium. The gradient of the line is given by c/n.

3.4 A Slab Waveguide

We now consider wave propagation in a symmetric slab waveguide as depicted in figure 3.2(a). For simplicity, the slab is assumed infinite in the y-direction with a refractive index, n_2 larger than the background index, n_1. Firstly, a

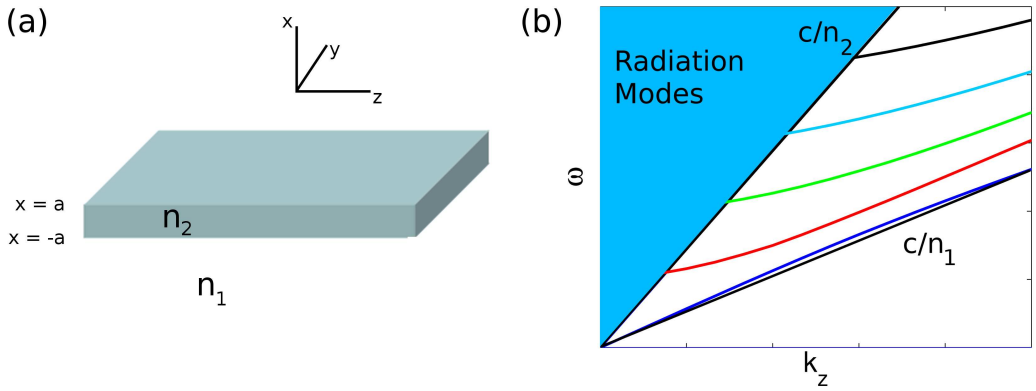

Fig. 3.2: (a) Schematic of a slab waveguide and (b) corresponding dispersion diagram. The guided modes are discrete in nature.

more general form of equation 3.9 is:

$$\nabla^2 E(r) + \frac{n^2\omega^2}{c^2} E(r) = 0 \tag{3.12}$$

where we have assumed an E-field time dependence of the form $e^{-i\omega t}$ and used the relationship in equation 3.11. For propagation in the z-direction we can

assume a solution of the form of equation 3.10. Equation 3.12 then reduces to:

$$\frac{d^2E(x,y)}{dx^2} + (\frac{n_i^2\omega^2}{c^2} - k_z^2)E(x,y) = 0 \qquad n_i = \{\begin{matrix} n_1, & x > |a| \\ n_2, & x < |a| \end{matrix}. \quad (3.13)$$

Examination of the equation implies that there are three main regimes to consider. The first is when $k_z > n_2\omega/c$; this implies that $1/Ed^2E/dx^2 > 0$ everywhere and $E(x)$ is exponential both within and outside the slab. This is clearly not a real solution and corresponds to the region below the ck_z/n_2 line in the dispersion diagram (figure 3.2(b)). The second regime is when $k_z < n_1\omega/c$; this implies that $1/Ed^2E/dx^2 < 0$ everywhere and $E(x)$ is oscillatory everywhere. In this case there is a continuum of states both within and outside the slab. This corresponds to the region above the ck_z/n_1 line in the dispersion diagram.

The final regime is when $n_1\omega/c < k_z < n_2\omega/c$; this implies that $E(x)$ is oscillatory within the slab and an exponential decay outside. This regime is the guided mode regime and corresponds to the region between the two "light lines" on the dispersion diagram. The three regimes are depicted in figure 3.3.

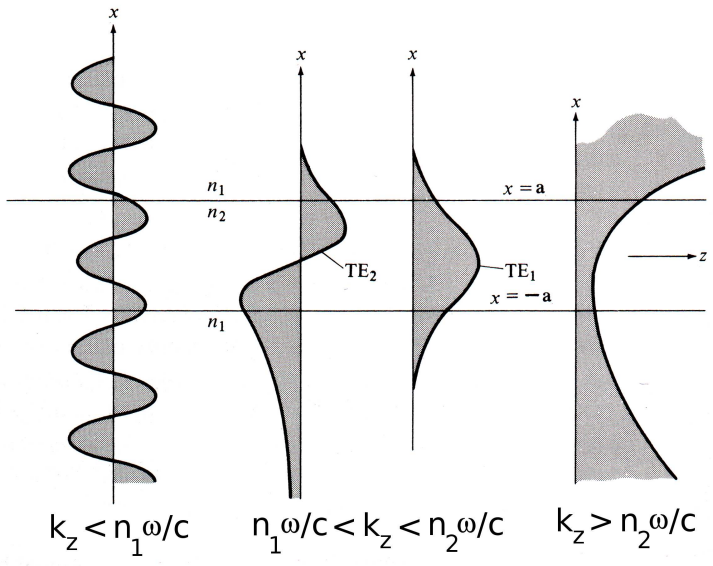

Fig. 3.3: Schematic of the electric field vector profile for the three slab waveguide mode regimes. Figure adapted from [33]

Solution of equations 3.7, 3.8 and 3.12, with the condition that E_y and H_z is continuous at $x = |a|$, reveals that the guided modes are discrete in nature [33] as depicted in figure 3.2(b), with the lowest order mode referred to as the zeroth order or fundamental mode. The solution is described in full in appendix A, but we begin it here to introduce the concept of transverse electric (TE) and transverse magnetic (TM) modes. Expanding equations 3.7 and 3.8 into cartesian form:

$$\frac{dE_y}{dz} = i\omega\mu H_x \tag{3.14}$$

$$\frac{dE_x}{dz} - \frac{dE_z}{dx} = -i\omega\mu H_y \tag{3.15}$$

$$\frac{dE_y}{dx} = -i\omega\mu H_z \tag{3.16}$$

$$\frac{dH_y}{dz} = -i\omega\epsilon E_x \tag{3.17}$$

$$\frac{dH_x}{dz} - \frac{dH_z}{dx} = i\omega\epsilon E_y \tag{3.18}$$

$$\frac{dH_y}{dx} = i\omega\epsilon E_z, \tag{3.19}$$

where we have assumed a time dependence of the form $e^{i\omega t}$ and $d/dy = 0$, we can see that the field vector equations form two distinct groups: (E_y, H_x, H_z and H_y, E_x, E_z). The first group is known as transverse electric (TE) modes (E field perpendicular to propagation direction) and the second transverse magnetic (TM). The remainder of the slab guided modes solution is laid out in appendix A. The solution shows that the number of guided modes that exist within a slab waveguide increases with increasing a, ω and $n_2 - n_1$. This idea can be extended to any waveguide: a discrete set of modes exists for each finite dimension. We refer to single-mode waveguides when we constrict a, ω or $n_2 - n_1$ such that only one mode is supported. The idea is applicable to laser waveguide modes and photonic crystal defect waveguides (see below).

3.5 A One-Dimensional Photonic Crystal

3.5.1 Some Periodic Concepts

A photonic crystal can be defined as a material with a periodic variation in dielectric constant, $\epsilon(r) = \epsilon(r + a)$, where a is defined as the lattice constant. There are a few concepts we can introduce to simplify the study of photonic crystals, which should be familiar to readers with a background knowledge of solid state physics [34]. The first concept is that of a unit cell. This is the most basic lattice unit, which when repeated in space will make up the full periodic lattice. By applying periodic boundary conditions at the edges of this unit cell, we can solve for the modes of the infinite crystal by studying only this unit cell. In a similar manner, we need only study a particular part of the dispersion diagram, known as the first Brillouin zone. This is another direct consequence of the periodic dielectric constant and arises from Bloch's theorem [31]. Bloch's theorem states that the field solution in a periodic lattice is simply that of a plane wave multiplied by a periodic function:

$$E(x) \propto e^{ik_x}.u_{k_x}(x) \tag{3.20}$$

for a periodicity in x. The periodic function enforces the condition $k_x = k_x + 2\pi m/a$ for any integer m. Thus all the information on a dispersion diagram is contained within $-\pi/a < k_x \leq \pi/a$ and this is defined as the first Brillouin zone. A final concept to introduce is that of normalised units for the dispersion diagram. We plot the frequency and wave-vector normalised to the lattice constant a. This makes the units dimensionless and means the dispersion diagrams can be applied to any length scale.

3.5.2 Numerical Analysis of Photonic Crystals

The analysis of the slab waveguide was sufficiently difficult to warrant appearance as an appendix. The analysis of photonic crystals is considerably more complex and typically requires a computational approach. There are two main computational approaches for modeling photonic crystals: frequency domain and time domain. The most common time domain approach, finite difference time domain (FDTD), involves solving Maxwell's curl equations (equations 3.7

and 3.8), in a given system, iteratively in small time steps. A given layout is split into a grid (grid size typically $\sim \lambda/10$) and given an initial field excitation at time, $t = 0$. The E-field is then calculated at every grid point, via equation 3.8, from the H-field and similarly the H-field is calculated from the E-field via equation 3.7. This is continued until desired or until a steady-state condition is reached. FDTD is best used for modeling the evolution of the fields in time, such as transmission of light through a waveguide or the decay of a cavity mode. It can also be used to calculate dispersion diagrams by taking a Fourier transform of a systems response to some initial broadband excitation, but the method is not guaranteed to resolve every mode discreetly.

The frequency domain approach does a direct calculation of the eigenvector problem formed by substitution of equation 3.20 into the wave equation (equation 3.12). The technique can only solve the modes for one k-vector at a time. It is much better suited to dispersion diagram calculations than the FDTD approach, as they are a time-independent (steady state) problem. It will also resolve two closely spaced modes as two independent solutions. To obtain the dispersion diagram for a photonic crystal with the frequency domain approach, we need only define the unit cell and then apply periodic boundary conditions at the cell boundaries. The resulting dispersion diagram will then be that of an infinite lattice. The dispersion diagrams for the photonic crystals in the remainder of this chapter were taken from reference [31] and were calculated with a frequency domain approach: the plane wave expansion method.

3.5.3 A Multi-layer Film

The simplest type of photonic crystal is a multi-layer film as depicted in figure 3.4. A multi-layer film consists of alternating layers of material with different refractive indices (or dielectric constants). Such multilayer stacks are also known as Bragg mirrors when the optical pathlength of the lattice constant, a, corresponds to half the wavelength, $\lambda/2n_{eff}$.

We consider propagation in the z-direction and the resulting dispersion diagrams for three structures: $n_1 = n_2$, $n_2 > n_1$ and $n_2 >> n_1$. The dispersion diagrams are plotted in figure 3.5 with normalised units and show the first Brillouin zone introduced above. For the $n_1 = n_2$ structure, the dispersion diagram is just the "light line", ck_z/n_1, and the periodicity we have introduced

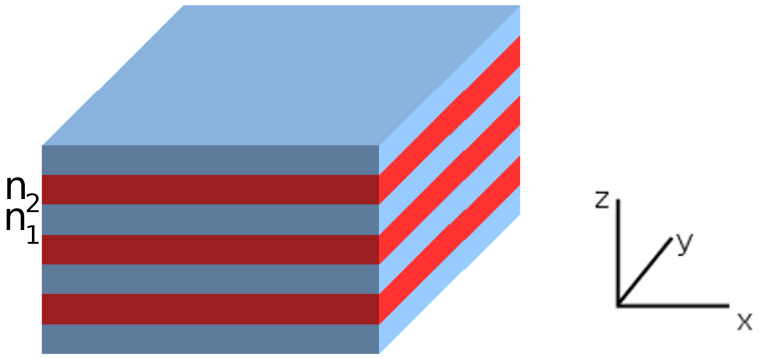

Fig. 3.4: Schematic of a multi-layer film.

causes the folding of the line at the Brillouin zone boundaries via Bloch's theorem. The dispersion diagram of the second structure is identical to that of the first, apart from the region close to the Brillouin zone boundary. There is a discontinuity at the boundary and a resulting frequency region in which no k-vector is supported - a photonic band gap (PBG). The third structure highlights the dependence of the PBG size on refractive index contrast. We label "bands" for the modes either side of the gap and the dispersion diagram for photonic crystals is typically called a band structure[3]. To understand the origin of the band-gap we consider the nature of the optical mode at the Brillouin zone boundary, $k_z = \pi/a$. The modes are standing waves with a wavelength of twice the lattice constant, a. There are two possible orientations for this standing wave: anti-nodes centred in the high refractive index material or anti-nodes centred in the low refractive index material. In general, low frequency modes tend to concentrate their energy in high index material and high frequency modes concentrate theirs in low index material [31]. Therefore, the two standing waves have different frequencies, with the difference increasing with increasing index contrast, and a photonic band gap is formed.

The band gap of a one dimensional photonic crystals can act as a perfect

[3] Dispersion diagrams for photonic crystals will typically be referred to as band structures for the remainder of this report.

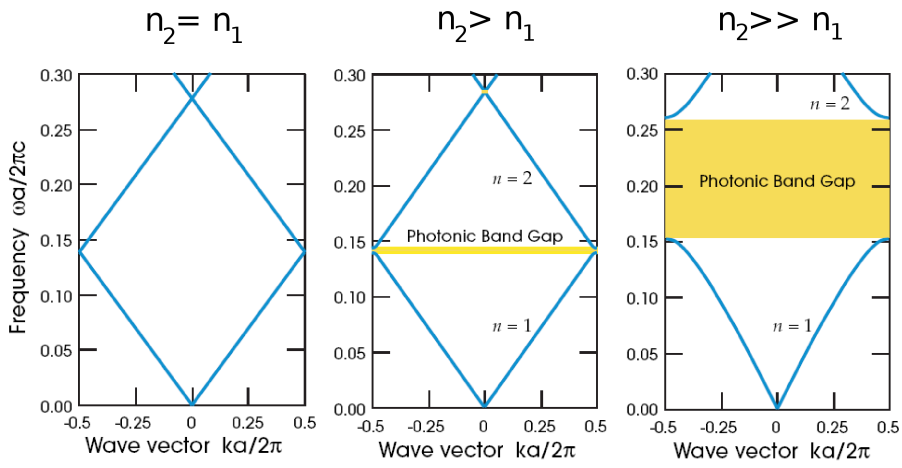

Fig. 3.5: Dispersion diagrams (or band structures) for three multi-layer films with differing refractive index contrasts (taken from [31]). The diagrams are plotted with normalised units and show the first Brillouin zone.

mirror and an example is studied as a potential laser mirror in chapter 7. However, the reflection is limited to normal incidence and we now look at two dimensional photonic crystals that have a more "complete" photonic band-gap.

3.6 Two-dimensional Photonic Crystals

Now we extend the periodicity to an entire plane by considering two dimensional photonic crystals. Two common examples of two-dimensional photonic crystals are shown in figure 3.6 and scanning electron microscope (SEM) images of such fabricated structures are shown in figure 3.7. A major difference between one dimensional and two dimensional photonic crystals is that we can obtain a band-gap for an entire plane of propagation direction. As with the slab waveguide we can also class the propagation modes into TE and TM type. The air holes in dielectric is the only two dimensional photonic crystal used in this report and its band-structure is shown in figure 3.8(b). As the structure is periodic in the entire plane we must consider propagation for any k-vector in the plane (not just k_z like the one dimensional case). The high symmetry of the structure means we need only study the highlighted region shown in figure 3.8(a) and not an entire unit cell. The Γ, K and M points are labelled

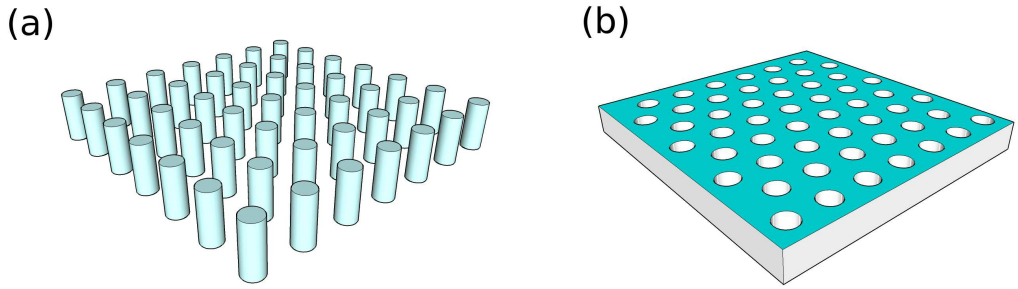

Fig. 3.6: Schematic of two examples of two dimensional photonic crystals: (a) a square lattice of dielectric rods in air and (b) a triangular lattice of air holes in dielectric.

in the figure and the corresponding k-vectors along the edge of this reduced Brillouin zone are used as the x-axis labels in the band structure. A complete band-gap is seen for both TE and TM polarisations, however the TE gap is much larger. The quantum-dot material used throughout this work mainly emits into TE polarisation, so it is the large TE band gap that will be used[4].

3.7 Photonic Crystal Defects

The true meaning of a band-gap is that the wave-vector in such a region is complex and that the field decays exponentially. An incident wave with a frequency lying within the band gap will therefore penetrate some distance into the crystal before being reflected. If we now consider bringing two crystals close together, we arrive at a similar situation to the guided modes of a slab waveguide: an exponentially decaying wave-vector in the two crystals, and an oscillatory wave between. Another way of obtaining this arrangement is to create defects in the crystal by removing single holes (or rods) to create a point defect or entire rows of holes (or rods) to create defect waveguides. These defects can then support a mode that lies within the band-gap. Schematics of these two most basic arrangements, in a dielectric rods in air photonic crystal, are shown in figure 3.9. We refer to a defect waveguide with one missing row of holes as a "W1". Photonic crystal defects have received much attention from

[4] In fact, both band-gaps only co-exist for a small range of hole radii. The TE gap extends over a larger range of hole radii and is therefore much more versatile than the TM gap.

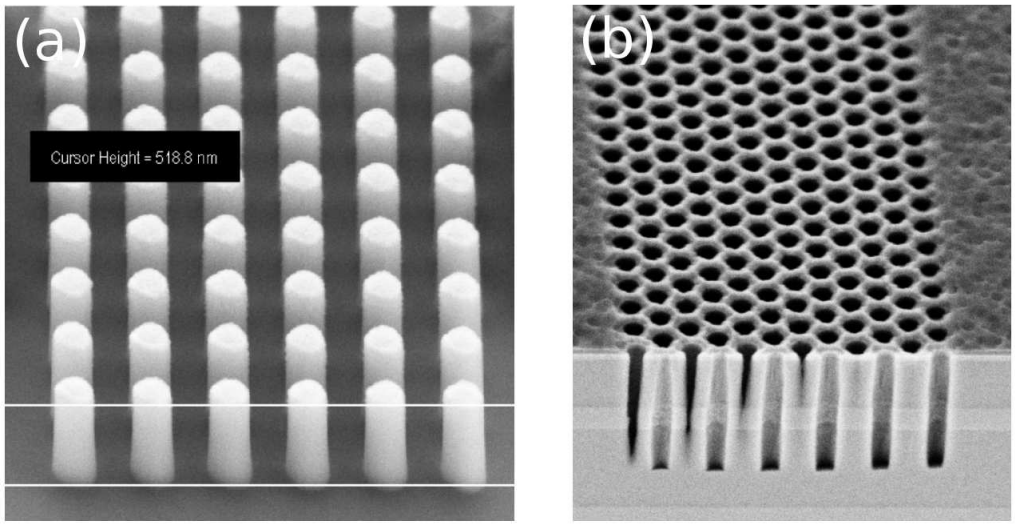

Fig. 3.7: SEM images of fabricated structures of figure 3.6.

the research community. Point defects have been used to create high Q cavities with Q values of the order 10^5 [35]. Cavities with even higher Q values (10^6) have been reported using a heterostructure of W1 waveguides with different lattice constants [36]. W1 defect waveguides have also been used for research into slow light [37].

The use of a W3 line defect waveguide as a laser mirror is the subject of chapters 8, 9 and 10 in this report.

3.8 Summary

This chapter has given the reader a basic introduction to photonic crystals and the main concepts surrounding them. An analytical approach to isotropic media and a slab waveguide was given using Maxwell's equations. Computational modelling techniques used to study photonic crystals were introduced. One and two dimensional photonic crystals were then discussed qualitively and the idea of defects was introduced. The next chapter will introduce the fabrication techniques that are required to build photonic crystals with band gaps at the near infra-red wavelengths of semiconductor lasers.

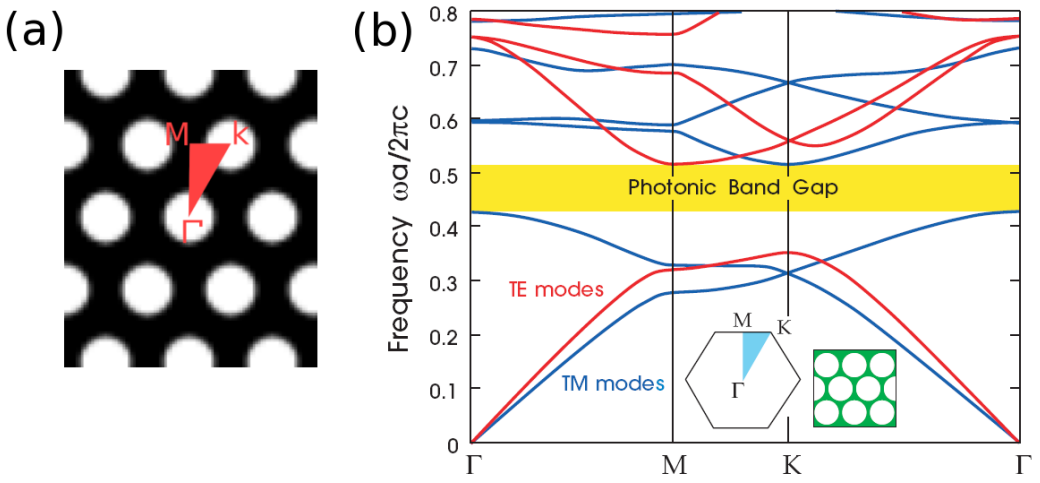

Fig. 3.8: Band structure of a triangular lattice of air holes in dielectric, taken from [31].

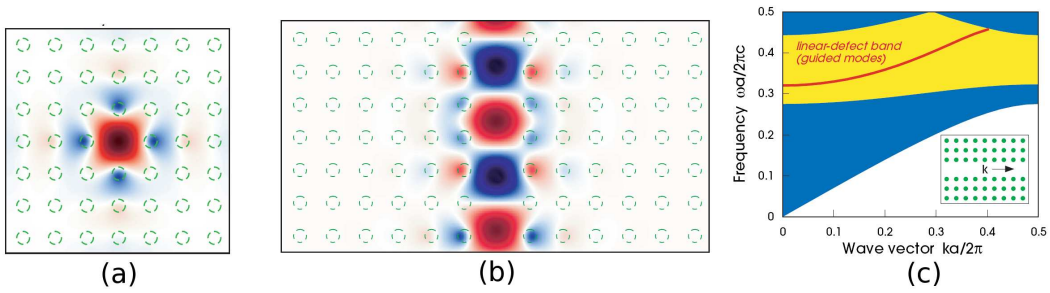

Fig. 3.9: Schematic of (a) a point defect and (b) a line defect waveguide and (c) band structure of the defect waveguide. Taken from [31].

4. DEVICE FABRICATION

4.1 Overview

This chapter gives a brief outline of the main fabrication processes used throughout my work. The chapter follows the fabrication steps for the active quantum-dot devices discussed in chapters 5–10. The fabrication process for the silicon devices in chapter 11 differs from the quantum-dot devices but the basic principles for the individual steps are the same. The chapter begins with an introduction to electron beam lithography, which is used to define device patterns. It then continues onto plasma etching which is used to transfer the design into semiconductor material. The remaining few steps relate to the deposition of electrical contacts.

4.2 Electron-Beam Lithography

4.2.1 Introduction

Electron beam (e-beam) lithography is the process of defining patterns on an electron sensitive surface using a beam of electrons. The electron beam is steered and focused by a set of magnets en route to the sample surface. The magnets are controlled by computer allowing the definition of any desired pattern (figure 4.1). A major advantage of e-beam lithography over photolithography (section 4.5) is that the resolution is much better (down to a few nm) which allows the definition of features down to a few 10s of nm in size.

Design patterns are broken into segments (or write fields) for exposure. The content of each write field is written on an exposure grid. The minimum spacing of this grid is dependent on the resolution of the digital to analogue converter (DAC) and the write field size. The minimum write field size of the machine available is 50 μm and it has a 16 bit resolution, i.e. 64,000 $\times$

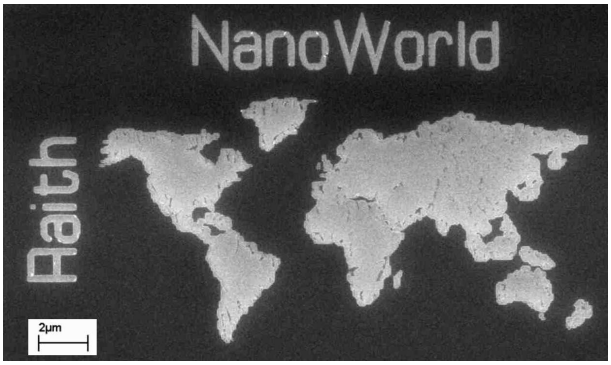

Fig. 4.1: SEM image of e-beam lithography exposed pattern of a world map. This image highlights the ability of e-beam lithography to produce any desired pattern. Image by Raith GMBH.

64,000 pixels. The minimum grid spacing is therefore 800 pm. This defines the minimum step size for addressing individual elements around a design pattern and is the minimum grid size that was referred to in the dispersion compensating mirror calculation in section 1.2.3.

Another important design limit is the area step size. A design polygon will be divided up into tiny squares defined by the area step size. Each square is exposed individually. The area step size is limited by parameters such as writing speed and electron current and is typically much larger than the minimum grid spacing. This limits the positioning of polygon elements even further. Single pixel lines, single pixel dots and circles are not limited by the area step size and can be placed on the design grid. These positioning limits can further limit the resolution of the machine.

An electron sensitive polymer is used as the e-beam resist and the physical structure of this resist changes when exposed to electrons. After exposure the resist can be developed in solvent to leave the defined pattern. Resists are defined as positive or negative. In a positive resist, the exposed regions wash away during development. In a negative resist, the opposite occurs and the exposed regions remain while the unexposed regions are washed away. The most common resist used here is Zeon Chemicals ZEP 520A resist (ZEP). ZEP is a high resolution positive resist allowing the definition of very small (tens of nanometres) features such as photonic crystal holes. Other e-beam resists used are SU:8 (low resolution, negative) and polymethyl methacrylate

(PMMA) (high resolution, positive). Each resist requires a certain exposure dose (measured in μA cm^{-2}) to completely expose an area of resist.

Proximity error, a major problem experienced with e-beam lithography, is addressed below. This is followed by the description of an advanced e-beam technique used in this thesis.

4.2.2 Proximity Error Correction

A major issue that can be experienced with electron-beam lithography is the proximity effect. As explained below, the proximity effect leads to incorrect feature sizes in a given pattern. This is very undesirable in photonic crystals and other periodic structures as it changes the spectral response of the structure. A solution to the proximity effect is therefore required to fabricate devices with the designed feature sizes and consequently well-defined spectral features.

Electrons that are incident on the resist are most likely to pass straight through with no interaction and back-scatter from the substrate. It is these back-scattered, lower energy, secondary electrons that are primarily responsible for resist exposure[1]. The scattering is a random process and results in slight exposure of the surrounding resist. It is this exposure of surrounding resist that leads to the proximity effect.

An easy way to explain the proximity effect is to consider a simple exposure pattern consisting of an array of circles (figure 4.2(a)). Each circle is given the same exposure dose. If the circles in the pattern are spaced closely enough (a few μm), then each circle will cause slight additional exposure of adjacent circles, due to the scattering mentioned above. The circles in the centre of the pattern have more neighbours and will therefore receive a higher exposure dose than those at the edge. Figure 4.2(b) is an SEM image of such an exposed pattern. The resist used was a negative resist (exposed resist remains after development). It is clear from the figure that the centre of the array has been overexposed, while the circles at the edge are reduced in size. This over- and under-exposure due to neighbouring elements is known as the proximity effect.

It is possible to model this proximity effect using Monte-Carlo simulations.

[1] A small amount of secondary electrons are also generated by forward- and back-scattering within the resist.

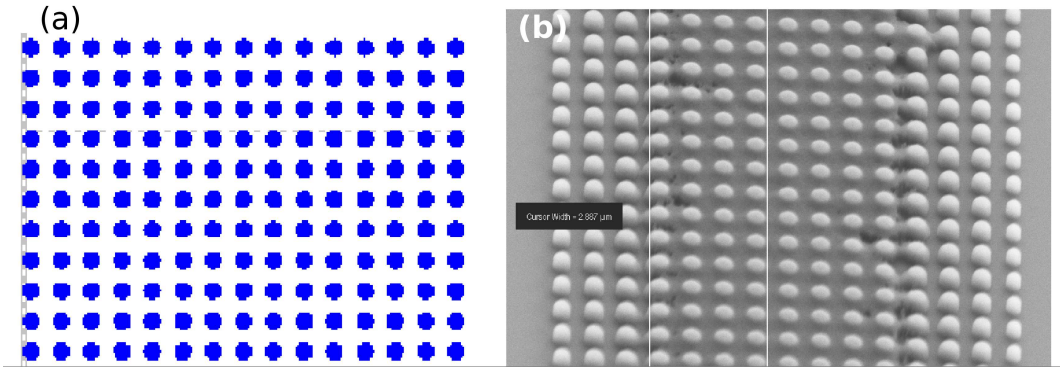

Fig. 4.2: Basic Illustration of the proximity effect. An uncorrected design pattern (a) and SEM image of the resulting exposure pattern (b) are shown. The centre of the pattern in (b) is overexposed and the circles at the edges are reduced in size.

The latest modelling techniques use an advanced proximity function [38] to describe the dose as a function of position, r, from an exposed point:

$$f(r) = \frac{1}{\pi\,(1+\eta+\nu)}\left[\frac{1}{\alpha^2}e^{\frac{-r^2}{\alpha^2}} + \frac{\eta}{\beta^2}e^{\frac{-r^2}{\beta^2}} + \frac{\nu}{2\gamma^2}e^{\frac{-r}{\gamma}}\right] \tag{4.1}$$

where α is the forward scattering range, β is the backward scattering range, η is backward scattering efficiency, ν is the efficiency of the exponential function and γ is the decay of the exponential function. Equation 4.1 can be summed or integrated for any pattern to calculate the dose contribution from each element. The doses can then be adjusted accordingly to produce a proximity corrected pattern. A commercial software package, NanoPECS, was used for such calculations throughout this work. The software requires α, β, η, γ and ν as input parameters. They have to be determined by experiment as they depend upon the sample material, resist and e-beam lithography regime that is used.

All of the parameters besides α describe back-scattering, the dominant contribution to the proximity effect. A method exists to determine these back-scattering parameters, based on the work by Stevens [39]. The technique involves writing an array of doughnut shapes (figure 4.3(a)). The array has an increasing inner radius along the x-direction and an increasing exposure dose along its y-direction. If the doughnut is exposed with a high enough dose, then the proximity effect will cause the doughnut to become a full cir-

cle. As we increase the inner radius of the doughnut, this effect will require a higher exposure dose. Figure 4.3(b) shows an SEM image of an exposed array of doughnuts. It can be seen in the figure that the first doughnut to just become a circle moves to increasing x-direction (inner radius), for increasing y-direction (exposure dose). The position of this first non-doughnut is plotted in figure 4.4.

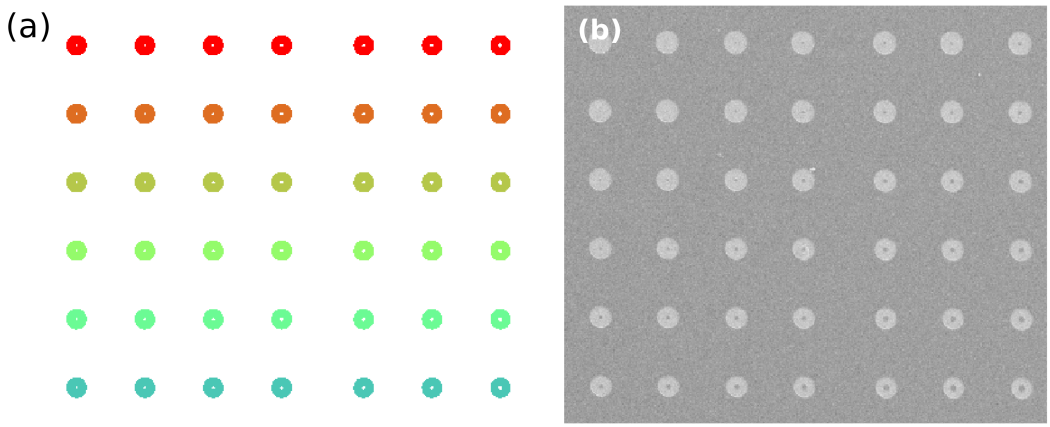

Fig. 4.3: (a) Design pattern of doughnut array used to determine proximity correction parameters. A 'redder' colour represents a higher dose. (b) SEM image of such an array exposed with electron beam lithography.

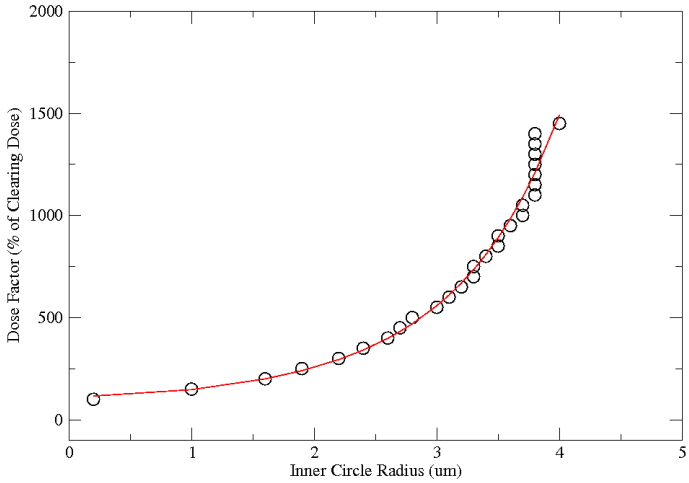

Fig. 4.4: Plot of dose against inner radius for the first doughnut to become a fully exposed circle for each value of inner radius. The raw data is fitted using equation 4.2.

This plot can be modelled by

$$D = D_c\,(1+\nu+\eta)\left[\eta e^{\frac{-R_1^2}{\beta^2}} + \nu\left(1+\frac{R_1}{\gamma}\right)e^{\frac{-R_1}{\gamma}}\right]^{-1} \tag{4.2}$$

where D is the exposure dose, D_c is the clearing dose and R_1 is the inner hole radius. β, η, γ and ν are obtained as fitting parameters. Equation 4.2 can be derived from equation 4.1 by considering the dose at the doughnut centre and integrating over the exposed region with the assumptions $\alpha \ll R_1$ and $\beta, \gamma \ll R_2$.

The other proximity correction parameter required is the forward scattering range, α. Forward scattering only occurs within the resist and therefore contributes much less to the proximity effect than back-scattering form the substrate. α can be determined following a method developed by Dubonos et. al. [40]. The technique involves exposing the pattern shown in figure 4.5(a). The pattern consists of a series of vertical lines of increasing width in the x-direction and decreasing dose in the y-direction. The pattern is corrected for the proximity effect using the correction software. The back-scattering parameters determined above are used with a range of different values for α. Assuming the top of each line is under-exposed there will be a definite boundary above which the line is not exposed. If the value chosen for α is correct this boundary will be at the same height for each line. If the chosen value of α is larger than the actual value then the narrower lines will be longer than the thicker lines. This is because the thicker lines will have been corrected for receiving more forward scattered electrons than actually existed. A microscope image of the exposed pattern for a range of values of α is shown in figure 4.5(b). The technique is better in theory than in practise and a perfectly horizontal boundary does not exist. However the best approximation to a horizontal line in the figure is for a value of $\alpha \sim 70\ nm$.

Once the parameters have been obtained, they can be used with the software to correct any design pattern. Figure 4.6(a) shows a corrected array of circles. It can be seen from the figure that the outer circles receive a higher dose to account for the proximity effect. Figure 4.6(b) shows an SEM image of such an exposed pattern, with uniform circle size.

The method described allows the proximity error correction of all the de-

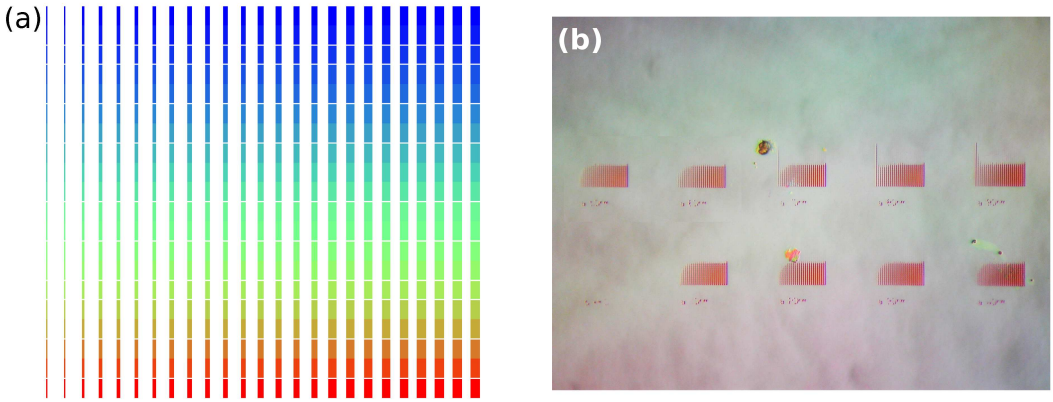

Fig. 4.5: (a) Design pattern for calculation of forward scattering range, α. (b) Microscope image of such an exposed pattern for a range of values of α (10 nm for bottom left to 90 nm for top right pattern).

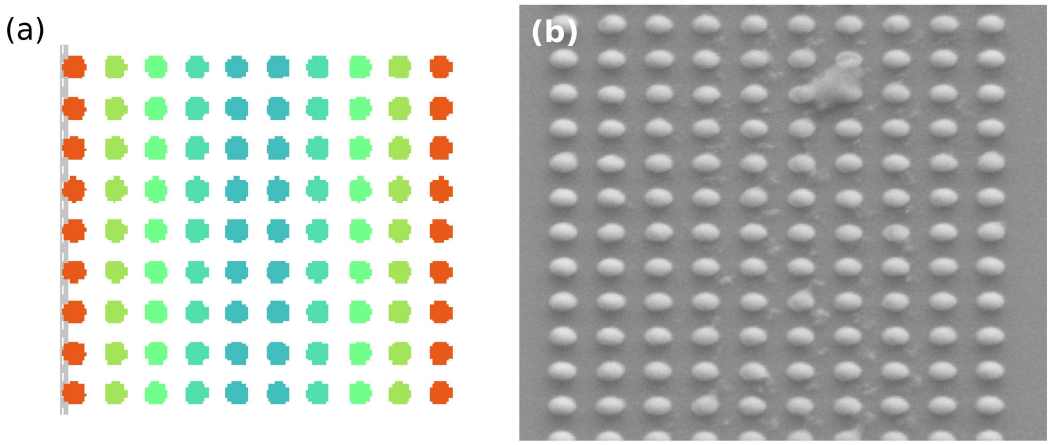

Fig. 4.6: Basic Illustration of the proximity effect. A corrected design pattern (a) and SEM image of the resulting exposure pattern (b) are shown. In this corrected design, the circles are a uniform size across the pattern.

sign patterns used throughout this thesis. This, in turn, should lead to the fabrication of devices with well defined spectral features.

4.2.3 Over-lay Exposure

A sample may require more than one electron-beam exposure step during fabrication. The method of aligning a second exposure to a previous one is known as an over-lay exposure. The most important requirement for this process is

the exposure of alignment marks in the primary exposure. These alignment marks should have sharp features and be highly visible (large) as they are viewed through a layer of resist in the secondary exposure. They should also be far (a few μms) away from the pattern to avoid exposure of the main pattern during re-alignment. Three alignment marks are used to define the working area for the second exposure. These three marks should be widely spaced to maximise accuracy. The design pattern of the alignment marks used during this work is shown in figure 4.7. The mark was easily visible through thick ($\sim$ 1 μm) layers of SU8 and alignment accuracies of a few 10s of nm were achieved.

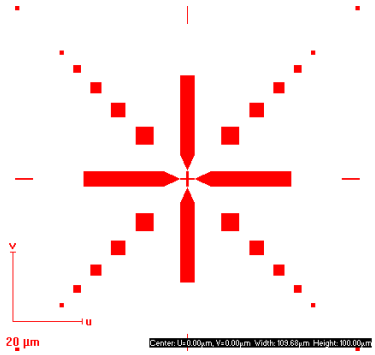

Fig. 4.7: Design pattern of alignment mark used for over-lay exposure

4.3 Plasma Etching

Lithography defines a desired pattern in a polymer resist. The transfer of this pattern to semiconductor material is achieved by etching. Patterns with small features (sub-micrometre) require plasma etching to obtain uniform pattern transfer with vertical sidewalls.

Plasma etching involves the exposure of the masked sample to a plasma. The plasma breaks up a feed gas into different species. There is typically a physical etching component (that removes material by bombardment) and a chemical etching component (that removes material by chemical reaction). High anisotropy (i.e. vertical sidewalls) can be obtained by balancing these two components. Two different plasma etching techniques, used throughout this work, are introduced below.

4.3.1 Reactive Ion Etching

ZEP e-beam resist is not hard enough to act as a mask for pattern transfer deep into the semiconductor material. Therefore an additional hard-mask is used to provide extra etch resistance and permit the required deep semiconductor etching. The spin coated hard-mask is called hydrogen silsesquioxane (HSQ) and is hard-baked onto the semiconductor material before the EBL exposure [41]. Reactive ion etching (RIE) is used for pattern transfer from the ZEP e-beam resist to the HSQ hard-mask.

In RIE, a bias voltage, established between the sample stage and the plasma, accelerates ions towards the sample. HSQ is very similar to silicon dioxide in composition and contains mostly silicon and oxygen atoms. The reactive gas used is CHF_3. The exact reaction process is quite complex but the main reactions are the formation of HF, which will etch SiO_2 (and HSQ) and the formation of carbon polymers that form a protective coating on the sidewalls as etching proceeds. This helps to keep the etch anisotropic.

The HSQ etching had to be optimised as part of this research. A recipe already existed for HSQ etching but the sidewall profiles were not vertical (figure 4.8(a)). Vertical sidewalls are highly desired for this work as patterns are to be transferred deep ($\sim 2\mu$m) into the semiconductor material. The hard mask gradually breaks down during semiconductor etching. If the hard-mask has angled sidewalls, this breakdown results in sidewall surface roughness in the semiconductor.

The plasma flickered and was unstable in the original recipe. To prevent this, the position of injection of the feed gas was moved away from the sample stage. The chamber pressure and RF plasma power was then adjusted so that the bias voltage matched that of the original recipe. The pressure was then adjusted to find the optimum etch recipe. Table 4.1 shows the exact recipes. A SEM image of HSQ etching for the new recipe is shown in figure 4.8(b). The side-wall profile is much improved from the old recipe. The plasma is also more stable in the new recipe resulting in more consistent etching.

Recipe	Ring Position	CHF_3 Flow	Power	DC Bias	Pressure
	(cm)	(sccm)	(W)	(V)	(mBarr)
Old	25	200	43	-465	5×10^{-2}
New	0	200	41	-468	4×10^{-2}

Tab. 4.1: Old and new optimised RIE recipes.

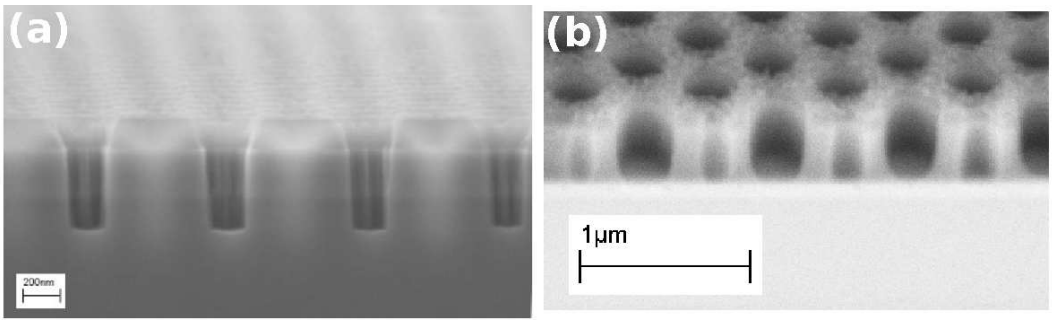

Fig. 4.8: SEM image of HSQ hard mask etched with (a) old and (b) new RIE recipe. The photonic crystal holes in (a) have also been etched into the semiconductor, but the HSQ is still visible. The sidewalls in the HSQ are clearly more vertical in the new recipe.

4.3.2 Chemically Assisted Ion Beam Etching

Chemically assisted ion beam etching (CAIBE) is used for pattern transfer into III-V semiconductor materials[2]. In the CAIBE machine available, Argon is injected into an ion gun where a plasma is generated. The resulting Argon ions are accelerated in a high energy ion beam towards the sample by a beam voltage. This ion beam is the physical component of the etching. Chlorine is fed into the chamber and acts as the chemical component.

The advantage of CAIBE over RIE is that the plasma generation and the etching conditions can be varied independently. The physical component is adjusted by variation of the ion beam parameters (voltage, current) and the chemical component is adjusted by variation of the Chlorine flow and sample temperature. This allows for greater control of the etching and etch depths of up to 2.5 μm can be achieved in GaAs based material.

Optimisation of CAIBE recipes for specific structures (photonic crystals,

[2] Pattern transfer into silicon is achieved using RIE and is discussed in chapter 11.

lasers etc) are discussed in the relevant chapters.

4.4 Contact Insulation

Active devices require a layer of contact insulation before the deposition of electrical contacts. This layer sits between the ridges or mesas allowing large contact pads to be defined over a single device and still ensuring only the ridge/mesa top is electrically pumped (figure 4.9). A secondary purpose of this insulation is to protect the mesa/ridge sidewalls during further processing steps. The HSQ hard-mask is removed by hydrofluoric acid and the insulation layer protects the sidewalls during this potentially damaging process. In particular, in the GaAs quantum dot material, the insulation prevents oxidation of the Aluminum containing regions.

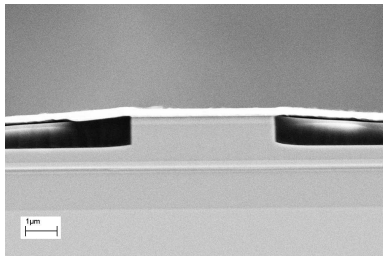

Fig. 4.9: SEM image of laser cross-section. The insulation is the dark layer either side of the laser ridge. The top contact can be seen as the very bright layer on top of the ridge and insulation.

The material used for contact insulation is SU:8. SU:8 has the advantage of being an electrical insulator and both a photo-resist and electron beam resist. The insulation regions can therefore be defined by an overlay exposure in precise locations on the sample. This overlay exposure is not always necessary. If a mesa waveguide is narrow enough, the SU:8 will not settle on the mesa top. This faster method of definition is known as self-aligned contact insulation. Once defined, the SU:8 is hard baked at high temperature (180^{o}C).

4.5 Photolithography

4.5.1 Introduction

Almost all of the devices in this work were defined using e-beam lithography. This is because these devices included small feature beyond the resolution of photolithography. However, photolithography is a much faster, simpler technique than e-beam lithography. Photolithography was used in this thesis for some larger devices and for a procedure called lift-off (next section) that defines electrical contact windows.

Photolithography works similarly to e-beam lithography in that a sensitive resist is used and areas of a sample are exposed according to a desired pattern. In photolithography, the resist is light sensitive and the exposure is from UV light and not electrons. A metal template mask is required to block the UV light from areas to be left unexposed. As with e-beam lithography positive and negative resists are available. After exposure, the sample is developed to wash away the unwanted areas of resist.

4.5.2 Lift-Off

Lift-off is a simple technique used to produce patterned layers of material. It is an alternative to etching and is therefore useful in process steps where etching is difficult or not feasible. The primary use of lift-off in this work is the patterning of electrical contacts. Etching of metals is difficult and potentially damaging to the surface, so the gentle lift-off process is used instead.

In a lift-off process (figure 4.10), an assisting layer is spun onto the sample followed by a layer of positive photo-resist. The assisting layer must be soluble in the developing agent for the photoresist. The desired pattern is then exposed onto the resist using photolithography. The sample is developed for approximately 25 % longer than normal. The exposed part of the resist will wash away as usual and the assisting layer in this region will also dissolve. The longer development time leads to an undercut of the photoresist (figure 4.10(b)). The desired material (e.g. electrical contact metals) is then evaporated onto the sample (discussed in detail in next section). The sample is then exposed to a solvent that will dissolve the photo-resist. The photo-resist

washes away, taking the unwanted areas of material with it. The assisting layer can be removed in the photo-resist developer if necessary.

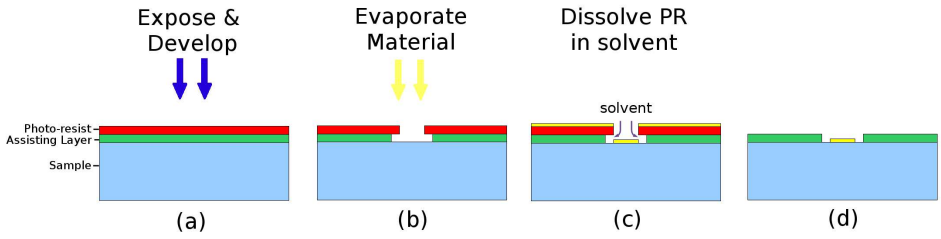

Fig. 4.10: Schematic of main steps in lift-off procedure.

Electron beam lithography can also be used for lift-off with PMMA resist. This is because the scattering of electrons discussed in section 4.2.2 leads to an angled sidewall in the PMMA that is similar to the undercut in figure 4.10(b). Thick layers of PMMA will provide the best results as there will be greater electron scattering, although too thick a layer will compromise pattern resolution. This e-beam lift-off procedure is used successfully in chapter 11.

4.6 Electrical Contact Evaporation

Evaporation is the standard method for depositing electrical contacts onto III-V materials. In an evaporator, the material to be deposited (the charge) is held in a container called the crucible under high vacuum ($\sim 10^{-6}$ mBarr). This crucible is heated resulting in evaporation of the charge. Due to the low pressure, atoms from the charge vapour travel in a straight line until they strike a surface and condense. Over time, a thin film accumulates.

An electron beam evaporator was used throughout this work for electrical contact evaporation. This type of evaporator has an electron gun as a heat source. The advantage of an electron gun is that only the charge is heated. This prevents evaporation (and subsequent contamination) from the crucible. The evaporator can hold four crucibles and so multi-layer films can be deposited. The layer sequence for top (p-type) and bottom (n-type) contacts is shown in table 4.2

Top Contacts (p)		Bottom Contacts (n)	
Material	**Thickness (nm)**	**Material**	**Thickness (nm)**
Nickel	20	Gold	14
Gold	200	Germanium	14
		Gold	14
		Nickel	11
		Gold	200

Tab. 4.2: Composition of electrical contacts.

4.7 summary

In summary, the main fabrication techniques used throughout my project have been described. Aspects of some of the steps, specific to this thesis, have been researched in detail. These include the proximity effect in e-beam lithography and the optimisation of RIE etching of a HSQ hard-mask. Any additional fabrication technique specific to an individual device is discussed later in the relevant chapter.

5. QUANTUM-DOT MATERIAL - THEORY AND CHARACTERISATION

5.1 Introduction

This chapter introduces the basics of quantum-dot material and presents results on the characterisation of the material used throughout this thesis. Characterisation of the material is necessary if any modeling of devices is to be attempted. In particular the spectral absorption loss describes how light interacts with any passive sections of a device. The method of Thomson et al. [42] described in section 5.3.1 is an easy way to obtain the spectral loss. The spectral gain can then be easily extracted.

5.2 Quantum-dot Lasers – The Natural Evolution of III-V Semiconductor Lasers?

The evolution of bulk GaAs material to quantum-dot material has been a 40 year journey determined by the available production technology as much as the underlying physical theory. The first bulk p-n semiconductor laser diodes were demonstrated in the early 1960s [1, 2, 3]. These early devices suffered from high loss (both electrical and optical), high threshold current and an inability to operate at room temperature. In 1963 Alferov [43] and Kroemer [44] simultaneously proposed the heterostructure concept. This involved sandwiching a layer of one type of semiconductor inside another wider bandgap semiconductor. The structure promised major improvements in carrier injection, carrier confinement, optical confinement and temperature stability. Room temperature, continuous-wave (cw) lasing was achieved in 1970 [45] shortly after the discovery of the AlGaAs/GaAs heterostructure [46, 47]. It was soon realised that if the sandwiched semiconductor layer could be made

very thin (on the order of the deBroglie wavelength) then the heterostructure would form a quantum well. This led to further improvements in laser performance due to the quantisation of energy levels and the density of states (figure 5.1(a)). The performance improvement was only realised experimentally [48] after improvements in fabrication techniques were made, such as the development of molecular beam epitaxy (MBE) [49]. A quantum well confines carriers in one dimension (perpendicular to the heterostructure); it was realised that by confining the carriers in two (quantum wire) or three (quantum dot) dimensions, further quantisation of the density of states would occur (figure 5.1(a)), leading to further improvements in laser performance [50]. In particular, quantum dots would have discrete energy levels like electrons in an atom[1]. Technology again dictated progress and ten years later a quantum-dot laser was produced [51]. Figure 5.1(b) shows the evolution of semiconductor laser threshold current density with the advances in III-V semiconductor technology and highlights the important impacts heterostructures, quantum-wells and quantum-dots have made.

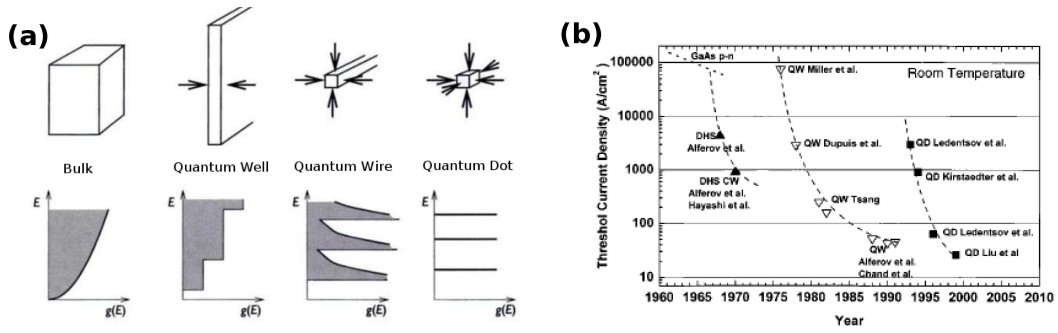

Fig. 5.1: (a) Quantisation of the density of states as the number of confining dimensions is increased in a heterostructure (from [52]) and (b) evolution of semiconductor laser threshold current with the development of the double heterostructure (DHS), quantum-well and quantum-dot lasers (from [53]).

5.2.1 Quantum-dot Fabrication

The most common and successful fabrication technique for III-V quantum-dot material is the Stranski-Krastanow growth technique. The technique requires

[1] quantum-dots are often referred to as artificial atoms.

lattice constant mis-match between the layer being deposited (what will become the quantum dots) and the substrate. Initially the deposited material forms normal layers, but after a thickness of only a few monolayers, lattice strain causes 3D islands to form and these form the quantum-dots. A thin continuous layer remains below the dots and this is known as the wetting layer. InGaAs/InAs quantum-dots grown on a GaAs substrate can operate over the 1–1.3 μm spectral range and InGaAs/InAs quantum-dots on an InP substrate can cover the 1.4–1.9 μm range.

5.2.2 Quantum-dot Lasers - Ideal World vs Real World

The main driving factors for the development of quantum-dot lasers were low threshold, high temperature stability and single frequency operation all arising from the delta function density of states. Very low thresholds were achieved [54] after two major fabrication breakthroughs. The first of these was to stack multiple quantum-dot layers on top of one another to increase the available modal gain [55]. The other breakthrough was to place each quantum-dot layer inside a quantum-well to prevent exciton escape from the quantum-dots due to thermal excitation [56]. Temperature stability of the threshold current at room temperature was also observed after this second breakthrough. One area where quantum-dot lasers have not lived up to their theoretical promise, however, is single frequency operation. This is because the fabrication process described above results in an inhomogeneous distribution of dot sizes and a resulting inhomogeneously broadened emission spectrum as depicted in figure 5.2.

The inhomogeneous broadening of the emission/gain spectrum of the quantum-dots is undesirable in relation to single frequency operation and threshold current density, since it reduces the available gain at the lasing wavelength. However, a broad gain spectrum is of benefit to short pulse operation as described in section 2.3.2. Other properties of quantum-dot lasers that satisfy the mode-locking criteria outlined in section 2.3.2 include:

- **Fast recovery time** ($<$ 1 ps) under both gain [57] and absorption [58] conditions. A reverse bias applied to the saturable absorber can significantly decrease its recovery time further [59].

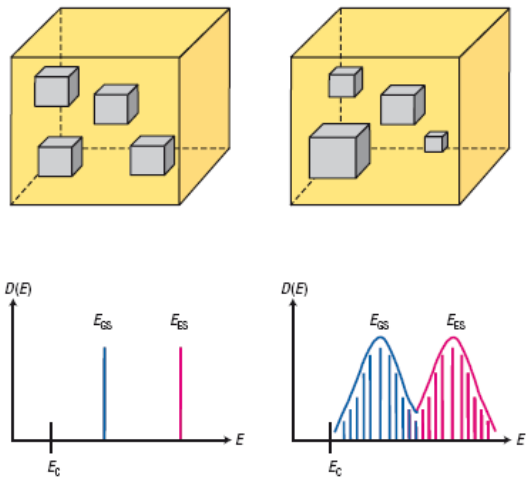

Fig. 5.2: Schematic showing the ideal and real-world distribution of quantum-dot sizes and resulting electron density of states profile (taken from [24]).

- **Low absorber saturation energy** arising from delta function density of states. In an ideal quantum dot, one carrier is needed to reach transparency and a second to achieve inversion. This makes mode-locking easier to achieve with the self-starting passive technique. However, the gain saturation energy is also lower and so the stability of the mode-locking is not enhanced relative to other materials. The stability can be improved by incorporating differing cross sectional areas of the gain and absorber with a flared structure as mentioned in section 2.3.2 and explored in chapter 10.

- **Low linewidth enhancement factor** [60] leading to reduced self-phase modulation and resulting dispersion and temporal broadening. However, this property is uncertain as other reports claim a drastic increase in α above threshold [61]. Gioannini and Montrosset give a convincing argument to explain the different results [62]. They suggest that even with an α value of zero for the lasing state, carriers in other states (such as the first excited state or non-lasing parts of the ground state) can contribute to strong chirp, particularly above threshold, giving a non-zero effective linewidth enhancement factor, α_{eff}.

Other advantages for passive mode-locking include:

- **Reduced carrier diffusion**, which is the subject of chapter 6 of this thesis, allows the fabrication of small structure laser devices that have been etched through the active layer. This is the key parameter that allows the exploration of the deeply etched laser mirrors studied in this thesis. Etching through the active region also reduces the saturation energy of the absorber due to strong confinement of the optical field.
- **Low threshold currents.** As mentioned above quantum-dot lasers exhibit very low threshold currents. Mode-locking can occur very close to threshold in quantum-dot lasers so low pump power mode-locked operation can be achieved.
- **Low temperature sensitivity.** Also mentioned above was the low temperature sensitivity of quantum-dot lasers. This has been shown in mode-locked operation too [63].

The remainder of this chapter characterises the gain and loss of the quantum-dot material used throughout this thesis. The following chapter then characterises the surface recombination and carrier diffusion in the material.

5.3 Quantum-dot Material Characterisation

The quantum-dot material used throughout this thesis consists of 10 layers of InAs quantum dots inside $Ga_{0.85}In_{0.15}As$ quantum wells. This material was grown by NL Nanosemiconductor GmbH using molecular beam epitaxy. The size and composition of the dots was chosen such that the peak of the emission was at 1280 nm. The exact layer composition of the material is shown in table 5.1.

5.3.1 Material Loss and Gain

Method

The spectral loss and gain of the quantum dot material was obtained following the multi-section method of Thomson et al. [42]. The method allows one to

Thickness (μm)	Repeats	Description	Composition and Doping
0.1		Cap	GaAs p = 5x10^{20}
0.015		Top Cladding	$Ga_{0.4}Al_{0.6}As$ p = 3 x10^{18}
0.4			$Ga_{0.4}Al_{0.6}As$ p = 1 x10^{18}
0.5			$Ga_{0.4}Al_{0.6}As$ p = 5 x10^{17}
0.033	10	Waveguide	GaAs
0.005	10	Quantum-well	$Ga_{0.85}In_{0.15}As$
0.0008	10	Quantum-dots	InAs
0.033		Waveguide	GaAs
0.5		Lower Cladding	$Ga_{0.65}Al_{0.35}As$ n = 5 x10^{17}
1			$Ga_{0.65}Al_{0.35}As$ n = 1 x10^{18}
0.02			GaAs n = 3 x10^{18}
		Substrate	GaAs n+

Tab. 5.1: Material composition of quantum-dot material

obtain the gain and loss spectra via measurements from a single multi-section device. One major advantage of this is that any coupling loss in the measurement set-up remains constant for all measurements. The device consists of a broad-area ridge with five or six identical sections, each with their own separate contact for electrical excitation. Feedback is prevented by a long absorbing region and an angled facet, thus avoiding lasing. In this experiment an un-cleaved facet was used instead of an angled facet. A schematic of the device is shown in figure 5.3(a).

50 μm wide stripes were defined using photo-lithography and the pattern transferred into the quantum-dot material using chemically assisted ion beam etching (CAIBE) with Chlorine chemistry. The ridges were etched to a depth of 2 μm, through the active region. Full-length contacts were laid down on the ridges using an electron beam evaporation step and a lift-off step. A third photo-lithography step was used to define 4 μm wide slots perpendicular to the contacts at equal intervals (250 μm) along the contacts, to create multi-section devices. The slots were then ion-milled (CAIBE etching at a low temperature with no chemical component) to electrically isolate each of the sections. The devices were then cleaved at the appropriate end and mounted p-side up on an earthed copper block (figure 5.3(b)). The device output was coupled through a lens into an optical spectrum analyser (OSA). An example of the emission

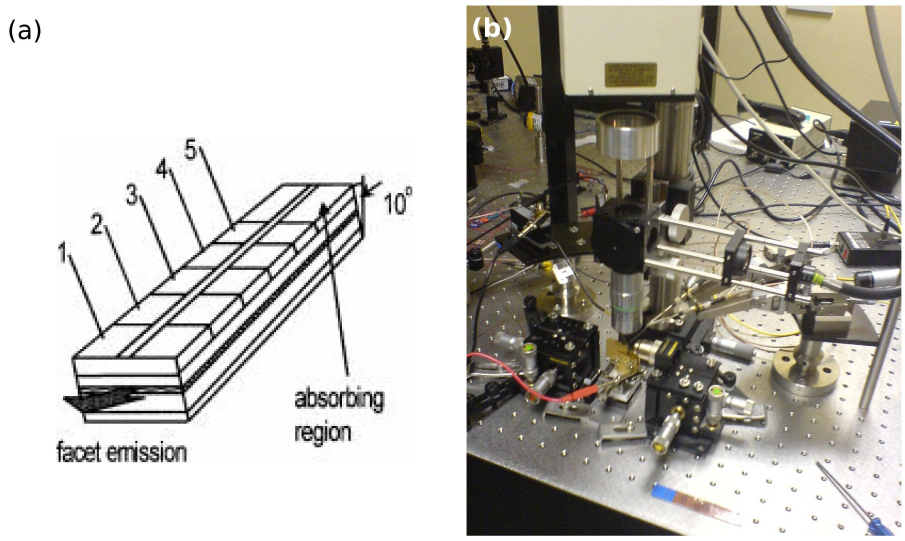

Fig. 5.3: (a) Schematic of multi-section device for measurement of gain and loss spectra (taken from [42]) and (b) Measurement set-up for multi-section device measurements

spectrum from a multi-section device taken by the OSA is shown in figure 5.4. The emission spectra shown are for each section pumped individually. Note how the peak of this emission shifts to longer wavelength as the excited section moves farther from the output facet. This is due to higher absorption of shorter wavelengths in the unpumped absorbing sections. The material gain peak is at a wavelength of 1280 nm in reality (see below). The emission spectrum is fairly broad (∼150 nm) allowing the gain and loss spectra to be measured over the same broad range.

Loss Spectrum

The loss spectrum can be obtained from a multi-section device by pumping each section independently and measuring the output emission spectrum of each (as in figure 5.4). Firstly the emission spectrum is taken with section 1 being pumped only. It is then measured, for the same current density, for section 2 only, section 3 only and so on. As each section is the same length, they act as similar sources of amplified spontaneous emission (ASE) at different distances from the output facet. The passive distance is increased as each section is successively pumped. The output intensity, I_t, can be related

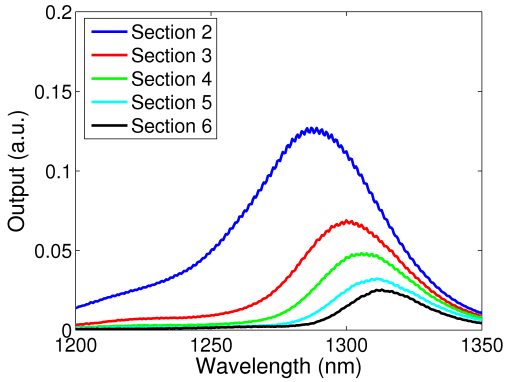

Fig. 5.4: An example of the emission spectra, from a multi-section device, obtained by the optical spectrum analyser. The spectra shown are for each section pumped individually at 25mA

to the initial ASE intensity, I_0, via

$$I_t = I_0 \left(e^{-\alpha_i L}\right) \tag{5.1}$$

where L is the passive length transmitted through and α_i is the internal modal loss of the material. It is easily seen from equation 5.1 that a plot of $\ln(I_t)$ versus L should be a straight line plot with gradient $-\alpha_i$. Figure 5.5 shows two such plots for wavelengths of 1280 nm (peak emission wavelength) and 1325 nm. The scatter in the straight line is small, indicating low experimental error. Some error may have arisen from slightly differing section lengths. By analysing all the data from the OSA measurements in the same manner, a plot of internal loss, α_i, versus wavelength can be obtained (figure 5.6). The absorption edge at $\sim$ 1280 nm can clearly be seen in figure 5.6. The plot is less smooth to the left of the absorption edge. This is because signal strength is lower in this region (due to increased absorption) and this leads to an increase in uncertainty. The loss in the non-absorbing region is ~ 6 cm^{-1}. This value is in good agreement with other measurements on the material [64]. Any loss in this spectral region arises from optical scattering and free-carrier absorption only.

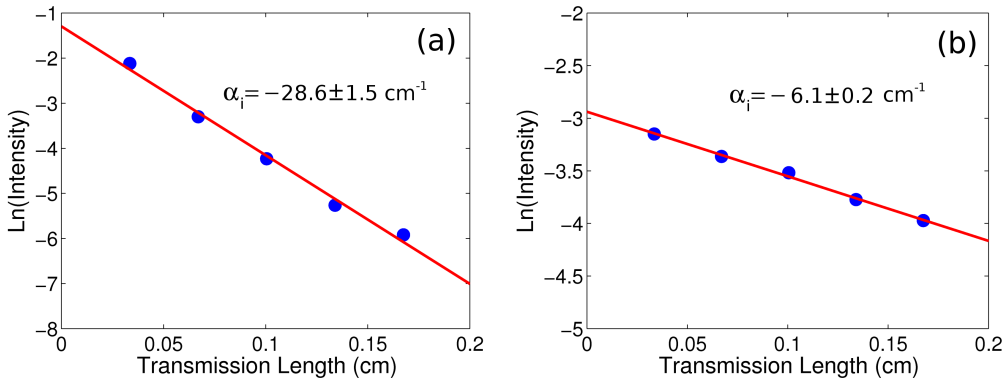

Fig. 5.5: Logarithmic plot of Intensity versus passive transmission length for multi-section devices at (a) 1280 nm and (b) 1325 nm

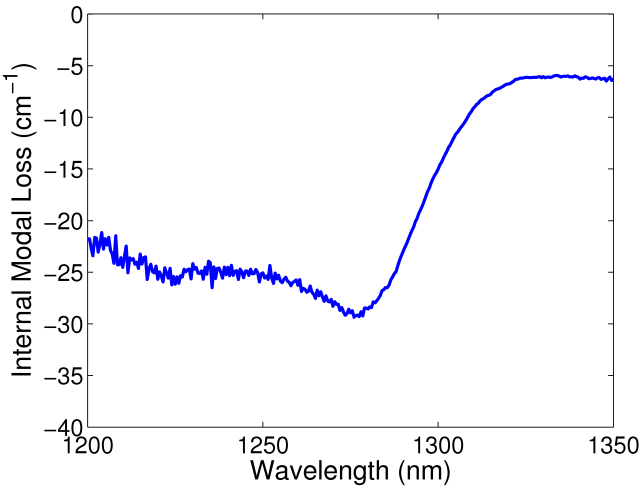

Fig. 5.6: Loss spectrum of quantum dot material obtained via multi-section method

5.3.2 Gain Spectrum

The gain spectrum can be obtained from the multi-section devices with similar ease as the loss spectrum. The active length of the device can be varied by pumping different sections together simultaneously. The output intensity, I, can be found as a function of net modal gain, G, by integration over the device length, L, of the expression for the amplification of light from a point source

a distance l from the facet [65].

$$\begin{aligned} I &= \int_0^L I_{sp} e^{Gl} dl \\ &= \frac{I_{sp}}{G}\left(e^{GL} - 1\right) \end{aligned} \tag{5.2}$$

where I_{sp} is the intensity of the spontaneous emission. The net modal gain, G, can be related to the material gain, g via

$$G = \Gamma g - \alpha_i \tag{5.3}$$

where Γ is the confinement factor. For two device lengths, L_1 and L_2, where $L_2 = 2L_1$, equation 5.2 becomes

$$\begin{aligned} \frac{I_{L2}}{I_{L_1}} &= \frac{e^{2GL_1} - 1}{e^{GL_1} - 1} = \frac{\left(e^{GL_1} - 1\right)\left(e^{GL_1} + 1\right)}{e^{GL_1} - 1} \\ \Rightarrow \quad G &= \frac{1}{L}\left[\ln\left(\frac{I_{L_2}}{I_{L_1}} - 1\right)\right] \end{aligned} \tag{5.4}$$

where I_{L_1} and I_{L_2} are the intensities from devices of length L_1 and L_2 respectively. The multi-section devices were measured with two sections (1,2) pumped simultaneously and four sections (1,2,3,4) pumped simultaneously. The measurements were made for a range of pump currents. The measured spectral intensities were inserted into equation 5.4 to obtain the plot in figure 5.7.

One can see from the plot that as we move to higher drive currents the ground state gain increases steadily. However, as we approach the highest drive currents the ground state starts to saturate and the excess carriers begin to populate the first excited state. This can be seen as the formation of an additional peak at shorter wavelength (∼1200 nm). The pump current density was limited here because of the power supply limit and the large device dimensions (50 μm wide). Using narrower devices would allow examination of higher pump currents, where one would expect the gain in the excited state to increase and grow beyond the ground state level. This is because there is a greater density of states in the excited state.

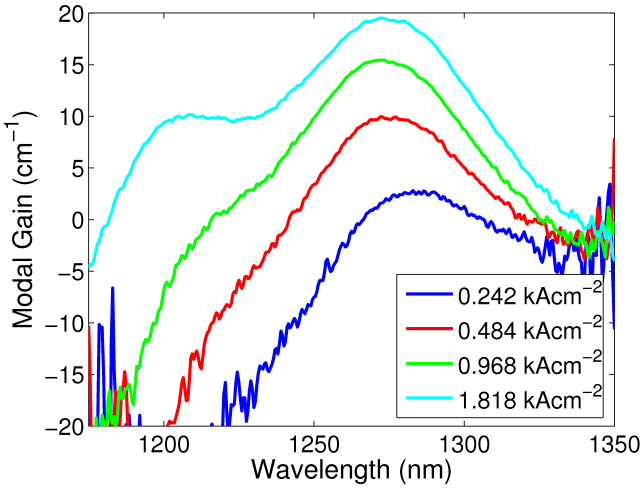

Fig. 5.7: Gain spectrum of quantum dot material obtained via multi-section method

5.4 Summary

In summary, this chapter intorduced the concept of quantum-dots and their potential as good laser material. The material used throughout this thesis was introduced and characterised. The multi-section method [42] was used to obtain both the gain and loss spectra of the quantum-dot material. The passive optical loss is a particularly useful parameter to know and is used in subsequent chapters for device modelling.

6. REDUCED SURFACE RECOMBINATION IN QUANTUM DOT LASERS

This chapter describes a method for obtaining values for the surface recombination velocity and diffusion length in quantum-dot mesa lasers. Surface recombination is a non-radiative recombination process that is particularly detrimental to laser performance when the exposed surface to volume ratio is large. It is therefore very important in photonic crystal lasers [14] and narrow mesa lasers. In this chapter, surface recombination velocity is found experimentally to be much lower in GaAs based quantum-dot material than it is in GaAs based quantum well material and similar to InP. The main results in this chapter were published in reference [64].

6.1 Introduction

Surface recombination is a form of non-radiative recombination in semiconductors. Like all non-radiative forms of recombination, it hampers laser performance and increases threshold current density. Surface recombination occurs at exposed surfaces of the active region, such as those exposed in deeply etched mesa lasers. At the surface, the semiconductor crystal lattice abruptly terminates causing surface defect states to form in high density. These states provide an alternate non-radiative recombination route for excitons across the band-gap (figure 6.1). The phenomenon is not characterised by a lifetime, τ, like other recombination processes, but by a rate, $\nu_s = L_c/\tau$, where L_c is the capture length. The rate, ν_s, is known as the surface recombination velocity. Typical values for ν_s are 5 x 10^5 cms^{-1} in GaAs bulk and quantum-well material and 10^4 cms^{-1} in InP material [13].

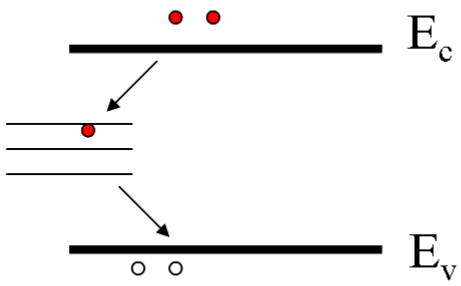

Fig. 6.1: Basic schematic illustrating surface recombination. Defect states at the material surfaces create non-radiative pathways across the gap for excitons

Recent work [15, 16] has observed that surface sidewall recombination in quantum-dot lasers is much reduced compared to that in quantum wells. The studies have not fully characterised this reduction, but attributed it to the strong three-dimensional confinement of carriers to the dots. When carriers are trapped in a dot, they do not interact with a defect. Only while they are in the wetting layer may diffusion to a non-radiative recombination centre take place. Carriers that are in the wetting layer are continually getting trapped by and escaping from the dots (due to thermal effects) and this effectively reduces their diffusion length. In this chapter this phenomenon is examined in detail and the parameters that dominate its behaviour quantified.

Surface recombination is more extreme in devices where the exposed surface area to active volume ratio is large, i.e. when device dimensions are small. In this study[64] mesa lasers of varying width were examined and the increase in lasing threshold (due to the increased surface recombination) observed. The study was conducted on the quantum-dot material discussed in chapter 5 and on an AlGaAs/GaAs quantum-well material to check the accuracy of the technique. This was a double quantum-well design, emitting at 980 nm, grown at the University of Sheffield. The exact layer structure of the material is shown in table 6.1.

6.2 Mesa Fabrication

The mesa lasers were defined using e-beam lithography to create as smooth a sidewall profile as possible. 2–10 μm and 5–50 μm wide stripes were defined in SU8 e-beam resist for the quantum-dot and quantum well samples respectively.

Thickness (μm)	Description	Composition and Doping
0.1	Cap	GaAs p+ (Zn)
0.1	Top Cladding	GaAs graded to $Ga_{0.59}Al_{0.41}As$ p+ (zn)
1.2		$Ga_{0.4}Al_{0.6}As$, p = 1.9 x 10^{18} (zn)
0.1		graded to $Ga_{0.8}Al_{0.2}As$
0.1		graded to $Ga_{0.74}Al_{0.26}As$
0.005	Barrier	GaAs
0.0065	Quantum-well	$Ga_{0.8}In_{0.2}As$
0.005	Barrier	GaAs
0.0065	Quantum-well	$Ga_{0.8}In_{0.2}As$
0.005	Barrier	GaAs
0.1		$Ga_{0.74}Al_{0.26}As$
0.1		graded from $Ga_{0.8}Al_{0.2}As$ to $Ga_{0.59}Al_{0.41}As$ (Si doped)
1.5	Bottom Cladding	$Ga_{0.59}Al_{0.41}As$ n = 1.4 x 10^{18} (Si)
0.1		graded to GaAs (Si)
0.5	Barrier	GaAs n = 1 x 10^{18} (Si)
	Substrate	GaAs n+

Tab. 6.1: Material composition of quantum-well material

The patterns were then transferred into a hydrogen silsesquioxane (HSQ) hard mask using reactive ion etching. The 2.2 μm high mesas were etched using a high beam voltage/low beam current (1450 V/16 mA) regime of chemically assisted ion beam etching [66]. The remaining HSQ was then removed with Hydrofluoric acid before SU8 insulation pads were created using an over-lay e-beam exposure and electrical contact pads were deposited. Figure 6.2 shows a cross-section of a fabricated laser mesa.

Broad area lasers (50 μm wide), of varying length, were also fabricated in the same manner, with the exception of the insulation pads. For such wide mesas it is possible to define large electrical contacts on the mesa using photolithography. Large contacts are easy to probe directly. These broad area devices were used to quantify the gain parameters [67] of the material, as discussed in section 6.4.2.

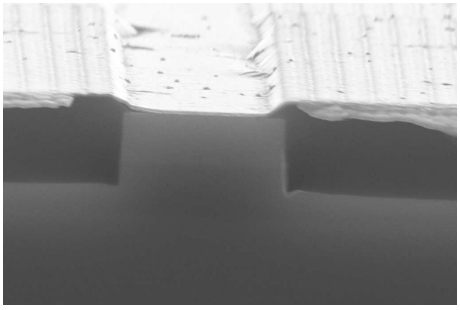

Fig. 6.2: SEM image of the cross-section of a laser mesa. The dark region is the insulation between the mesas. The light region at the top is the top electrical contact pad.

6.3 Measurement

The samples were cleaved into chips of suitable length (approximately 2 mm for the quantum-dot and 0.6 mm for the quantum-well devices) and mounted p-side up on earthed Copper blocks. The devices were driven with an electrical pulse generator and this was operated at a 2 % duty cycle to avoid unwanted thermal effects. The laser output was coupled into a Melles-griot power metre.

Power-current curves were obtained for each laser (figure 6.3). A straight line was fitted to each curve for the data above threshold and the threshold current was determined from the x-intercept of the line. A curve of threshold current density against mesa width was plotted for both materials (figure 6.4). For a 5 μm wide, 2 mm long, quantum-dot device, the threshold current was measured as 140 Acm^{-2}, comparing favourably with that of a similar length broad area device ($122\mathrm{Acm}^{-2}$).

The passive optical loss of each waveguide was measured by taking a transmission spectrum using a tunable laser source in the wavelength range of 1300–1310 nm. The internal loss, α_i, was determined from the Fourier transform of the resulting Fabry-Perot oscillations [68]. A loss value of 5 cm^{-1} for the quantum dot devices was obtained that, within experimental error, was identical for all waveguides indicating that the dependence of threshold current density on ridge width is dominated by sidewall recombination effects rather than by optical losses. Theses α_i measurements were performed by another member of my research group, Liam O'Faolain. The value he obtained is in close agreement with the value of 6 cm^{-1} that I measured in chapter 5.

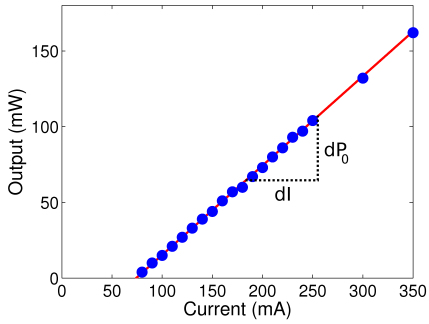

Fig. 6.3: An example of a power-current laser curve. This curve is for a 25 μm wide quantum-well laser.

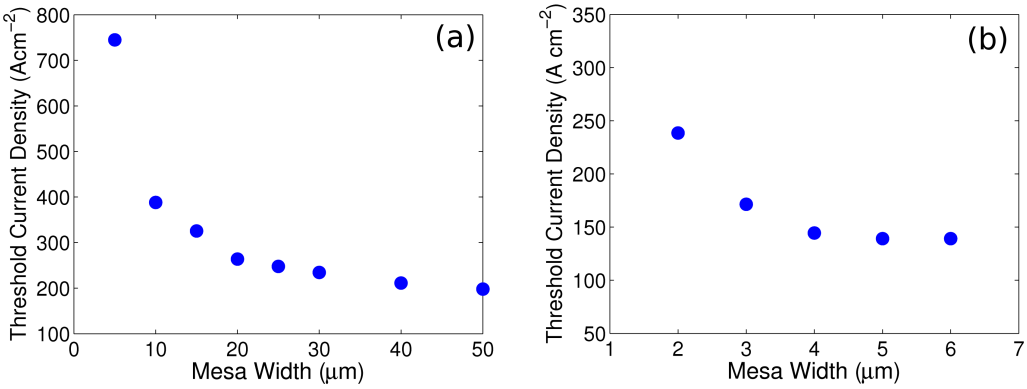

Fig. 6.4: Variation of threshold current density versus mesa width for (a) quantum-well material and (b) quantum-dot material

6.4 Theoretical Model

A theoretical model was used to fit the experimental results and establish values of surface recombination velocity, ν_s and diffusion length, L_d, following the approach of Coldren *et al* [13].

6.4.1 Transverse Carrier Density

The model was constructed by consideration of the transverse carrier density $N(x)$. Starting from the simple lateral diffusion equation

$$D\frac{d^2N(x)}{dx^2} = -\frac{\eta_i J(x)}{qd} + \frac{N(x)}{\tau} \tag{6.1}$$

where D is the diffusion coefficient, η_i is the internal quantum efficiency (taken to be 0.7 for the quantum-wells and quantum-dots), $J(x)$ is the applied current density assumed to be invariant in the x direction ($J(x) = J_0$), q is the electronic charge, d is the depth of the active region, and τ is the carrier lifetime (taken to be 2 ns in the wells [69] and 2.8 ns in the dots [70]). Equation (6.1) can be solved analytically at threshold ($J(x) = J_{th}$). Firstly we rewrite equation (6.1) in the form of an ordinary 2nd order differential equation

$$D\tau\frac{d^2N}{dx^2} - N(x) = -\frac{\eta_i J_{th}\tau}{qd} \tag{6.2}$$

The solution to such an equation takes the general form:

$$N(x) = Ae^{\frac{x}{\sqrt{D\tau}}} + Be^{-\frac{x}{\sqrt{D\tau}}} + \frac{\eta_i J_{th}\tau}{qd} \tag{6.3}$$

We have two boundary conditions for the situation: (1) the profile of the carrier density should be symmetrical about the center of the mesa (x=0) and (2) the diffusion current should be equal to the surface recombination current at the mesa sidewalls (x=±W/2)

$$\begin{aligned} \frac{dN(x)}{dx} &= 0 \quad \texttt{at } x = 0 \\ -\nu_s N &= D\tfrac{dN}{dx} \quad \texttt{at } x = \pm\frac{w}{2} \end{aligned}$$

The first boundary condition forces $A = B$ and so we can rewrite equation (6.3) as

$$N_{th}(x) = A\cosh\left(\frac{x}{L_d}\right) + N_p \tag{6.4}$$

with

$$N_p = \frac{\eta_i J_{th}\tau}{qd} \tag{6.5}$$

L_d is the diffusion length, equal to $\sqrt{D\tau}$ and is used as a fitting parameter in the model. N_p is the injected carrier density, that is the carriers supplied to the active region via electrical pumping. Therefore, looking at equation (6.4) for the transverse carrier density, the first term must be a loss term as $N(x)$ cannot exceed the carriers supplied, N_p. The constant A is therefore expected to be negative. We obtain A from substitution of $N(x)$ and dN/dx, from

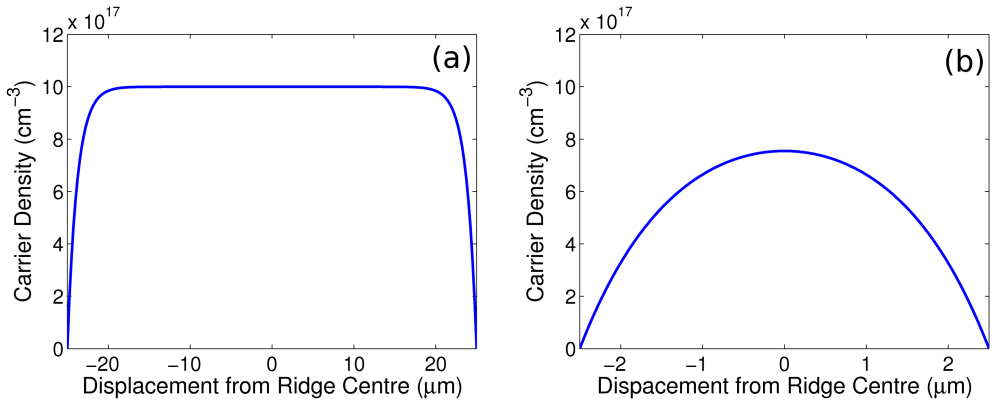

Fig. 6.5: Variation of carrier density across laser mesas of width (a) 50 μm and (b) 5 μm.

equation (6.4), into the second boundary condition. After some rearranging we find

$$A = -\nu_s N_p \left[\frac{D}{L_d} \sinh\left(\frac{W}{2L_d}\right) + \nu_s \cosh\left(\frac{W}{2L_d}\right) \right]^{-1} \tag{6.6}$$

A is negative as expected and the magnitude of the term $A\cosh(\frac{x}{L_d})$ will increase as $|x|$ increases, as we approach the sidewalls.

6.4.2 Threshold Gain

In this section, the 50 μm-wide, varied length, laser data is used to model the variation of threshold material gain, g, with threshold carrier density, N_{th}. For a 50 μm-wide device, we can assume $N_{th} \approx N_p$. To illustrate this figure 6.5 shows the carrier density profile for a 50 μm and 5 μm device according to equation 6.4. A value of 10^{18} cm^{-3} was chosen for N_p and 5 x 10^4 cms^{-1} for ν_s. Typical values for L_d and τ were chosen. One can clearly see that $N_{th} \approx N_p$ across most of the 50 μm device. This is clearly not the case for the 5 μm device where N_{th} is less than N_p even at the ridge centre. We can therefore obtain values of N_{th} for the 50 μm wide devices from their threshold current densities, J_{th}, using equation (6.5).

The threshold gain, g, was calculated by setting it equal to the optical losses

$$g = \frac{(\alpha_i + \alpha_m)}{\Gamma_x \Gamma_z} \tag{6.7}$$

with

$$\alpha_m = \ln(1/R)/L \tag{6.8}$$

,

$$\Gamma_x = \gamma \left[2 \left(\frac{n_{eff2}}{n_{eff1}} \right)^4 + \gamma \right]^{-1} \tag{6.9}$$

and

$$\gamma = 4\pi^2 W^2 \lambda^{-2} (n_{eff2}^2 - n_{eff1}^2) \tag{6.10}$$

where α_i is taken to be 11 cm^{-1} for the wells and 5 cm^{-1} for the dots, α_m is the mirror loss, R is the facet reflectivity taken to be 0.33 and L is the device length. Γ_z is the vertical confinement[1] calculated to be 0.05 for the wells and 0.016 for the dots using a commercial eigenmode solver (FIMMWAVE). Γ_x is the lateral confinement, n_{eff} is the effective refractive index for the given material, calculated (with FIMMWAVE) to be 3.23 for the wells and 3.43 for the dots. λ is the free space wavelength. Inspection of equations (6.7–6.10) shows that for the 50 μm wide lasers, g is only a function of device length, L. Now we can obtain both g and N_{th} for the 50 μm wide, their relationship can be plotted. Figure 6.6 shows the variation of g with N_{th} for the quantum-well and quantum-dot devices. As the lasers are operating below saturation, these plots can be modeled by the logarithmic expression

$$g\left(N_{th}\right) = g_0 \ln\left(\frac{N_{th}}{N_{tr}}\right) \tag{6.11}$$

where g_0 is the gain parameter from the fit (found to be 720 and 1199 cm^{-1} in the wells and dots respectively) and N_{tr} is the carrier density at transparency (found to be 6.85 x 10^{17} and 1.21 x 10^{18} cm^{-3} in the wells and dots respectively).

Equation (6.11) gives g as a function of N_{th} or with some rearrangement N_{th} as a function of g. If we now consider a set of lasers of a fixed length but varying width, inspection of equations (6.7–6.10) shows that g is a function of mesa width, W, only. Therefore, from equation (6.11) we have an expression for N_{th} as a function of W.

[1] Γ_z is the modal overlap for all the quantum-well (or quantum–dot) layers combined.

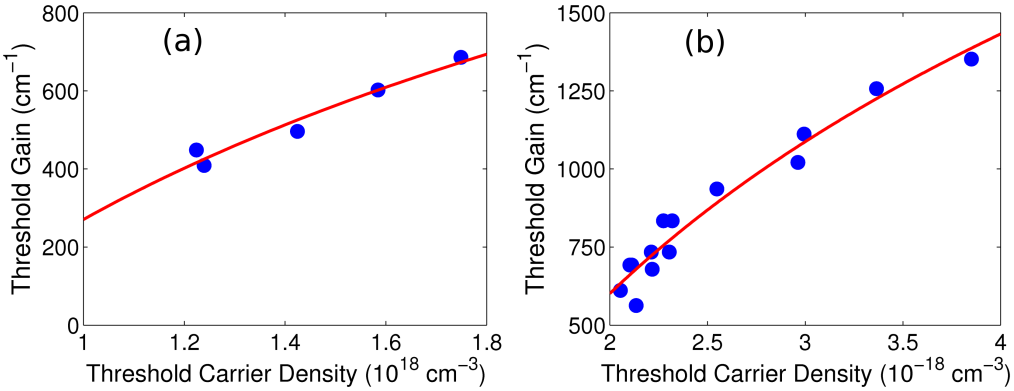

Fig. 6.6: Variation of threshold gain with threshold carrier density for 50 μm wide (a) quantum-well and (b) quantum-dot lasers

6.4.3 Carrier Profile and Optical Mode Profile

As was mentioned in section 6.4.1 and illustrated in figure 6.5, for narrow ridges, the assumption $N_{th} \approx N_p$ is no longer valid. To account for this, we can define an effective carrier density, N_{eff} as an approximation to N_{th}. To obtain N_{eff}, we integrate $N(x)$ in equation (6.4) across the width of the mesa.

Along with this distinct carrier profile, we must also account for the optical mode profile, which will be stronger in the centre of the mesa. This mode profile can be approximated as a cosine function as this is the form of the fundamental wave-guide mode inside a mesa. This function must be included in the integration of equation (6.4) as a weighting function, $P(x)$. $P(x)$ should therefore be a normalised cosine function

$$\begin{aligned} \int_{-\frac{W}{2}}^{\frac{W}{2}} P(x)dx &= \int_{-\frac{W}{2}}^{\frac{W}{2}} P_0 \cos(kx)dx = 1 \\ \Rightarrow \quad P(x) &= \frac{\pi}{2W} \cos\left(\frac{\pi x}{W}\right) \end{aligned} \tag{6.12}$$

This can be combined with equation (6.4) to give the following expression for N_{eff}

$$N_{eff} = \frac{\pi}{2W} \int_{-\frac{W}{2}}^{\frac{W}{2}} \cos\left(\frac{\pi x}{W}\right) \left[A \cosh\left(\frac{x}{L_d}\right) + N_p\right] dx \tag{6.13}$$

This integral can be solved by parts to give the solution

$$N_{eff} = \frac{A\pi^2 L_d^2 \cosh\left(\frac{W}{2L_d}\right)}{\pi^2 L_d^2 + W^2} + N_p. \tag{6.14}$$

As mentioned at the end of section 6.4.2 we have an expression for N_{th} as a function of W. We can now substitute N_{eff} for N_{th} and solve for N_p as a function of W. Using equation 6.5 we can then easily obtain J_{th} as a function of W. Now we have the desired theoretical relationship: the variation of threshold current density, J_{th}, with mesa width, W. This is the same relationship plotted from experimental results in figure 6.4 and the theoretical and experimental results can now be compared.

6.5 Results

The quantum-well devices were fabricated to act as a control in the study and check the validity of the theoretical model and experimental procedure. These results are examined first.

The theoretical curves of $J_{th}(W)$ for the quantum-well devices are plotted in Fig. 6.7 for four different values of surface recombination, ν_s. The experimental results from figure 6.4(b) are overlaid for comparison. Inspection of the plot suggests $\nu_s \sim 5 \times 10^5$ cms^{-1}. This is in good agreement with the accepted values [13] quoted in section 6.1. A value of 5 μm for L_d provided the best fit for the curve. Using L_d as a fitting parameter is discussed in more detail in the next section.

The agreement of the quantum-well material results with accepted values gives confidence in the model and procedure. The quantum-dot results can now be examined and values of ν_s and L_d obtained. The theoretical curves $J_{th}(W)$ for the quantum-dot are plotted in Fig. 6.8 for four different values of ν_s. Notice that one value of ν_s is zero and the curve is flat for mesa widths greater than roughly 1 μm. This is on the order of the wavelength (1.28 μm) and Γ_x probably drops substantially at this point, increasing the optical loss and raising the threshold current. Inspection of the plot suggests $\nu_s \sim 5$ x 10^4 cms^{-1} in the quantum-dot devices. This is an order of magnitude less than the quantum-well result and agrees with the argument in section 6.1. A value

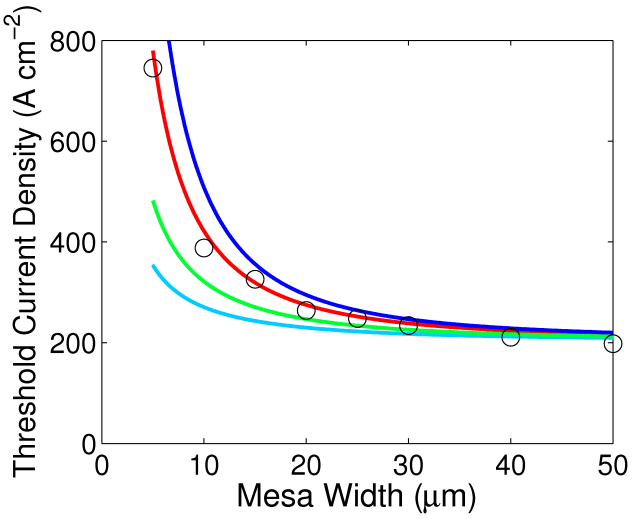

Fig. 6.7: The theoretical dependence of the threshold current density on mesa width for quantum-well lasers. The experimental data is overlaid. The blue, red, green and cyan curves represent values of ν_s of 5 x 10^6, 5 x 10^5, 2 x 10^5 and 1 x 10^5 cms^{-1} respectively.

of 1.0 μm for L_d in the dots provided the best fit. This value shows good agreement with that measured by Popescu *et al* [71]. They used a photo-luminescence technique to determine the diffusion length of a similar material and obtained a value of 1.65 μm for ground state emission.

6.6 Model tolerance

To test the robustness of this measurement approach, some of the key constants used in the modelling (α_i, η_i, Γ_z, τ), were varied to see the effect on the predicted values of ν_s and L_d. Figure 6.9 shows the effect on the results of varying α_i, η_i and Γz. The plot with the assumed constant values (figure 6.8) is shown at the top for reference. On first glance it appears that varying the parameters has no effect on the plots. However, closer inspection reveals a slight shifting of the theoretical curves for the different values of α_i. This shift is minimal and it can be concluded that the model is very tolerant to inaccurate values of α_i, η_i and Γ_z. The tolerance is due to effective cancellation of the constants in the modelling. This is difficult to show explicitly. It can be understood qualitatively by considering that the constants are used with the

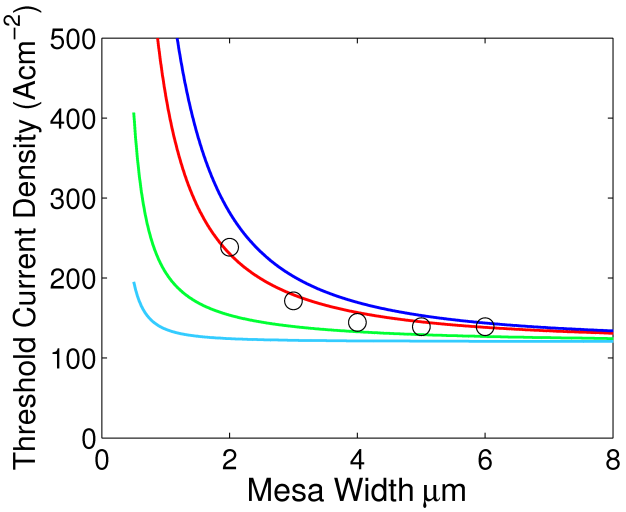

Fig. 6.8: The theoretical dependence of the threshold current density on mesa width for quantum-dot lasers. The experimental data is overlaid. The blue, red, green and cyan curves represent values of ν_s of 1 x 10^5, 5 x 10^4, 1 x 10^4 and 0 cms^{-1} respectively.

50 μm data to model the gain (equation 6.7) and threshold carrier density (equation 6.5 ($N_{th} = N_p$)) and then used again with the varied width data and the obtained gain equation (equation 6.11).

The model is not as tolerant to changes in the value of τ. Figure 6.10 shows the effect of varying τ on the theoretical curves. Figure 6.8 is again shown for reference. In figures 6.10(b) and (c) the value of L_d was left at 1.0 μm. The fit is not good, particularly for the higher value of τ. The value of L_d was optimised for each value of τ and the results are shown in figures 6.10(e) and (f). The optimised values of L_d were found to be 1.2 μm and 0.8 μm for τ equal to 2 ns and 3.5 ns respectively. It is less straightforward to understand why the model is more sensitive to τ. The parameter appears explicitly in the same equations as η_i and so could be expected to cancel. However, τ is also intrinsically related to D and L_d via $L_d = \sqrt{D\tau}$ and so it is unsurprising that varying τ will alter the predicted value of L_d. The variation of L_d is not too large ($\pm$ 20%) as we vary τ ($\pm$20%) and the value of ν_s does not change at all. We can conclude that the approach is robust, so long as τ can be estimated with reasonable accuracy.

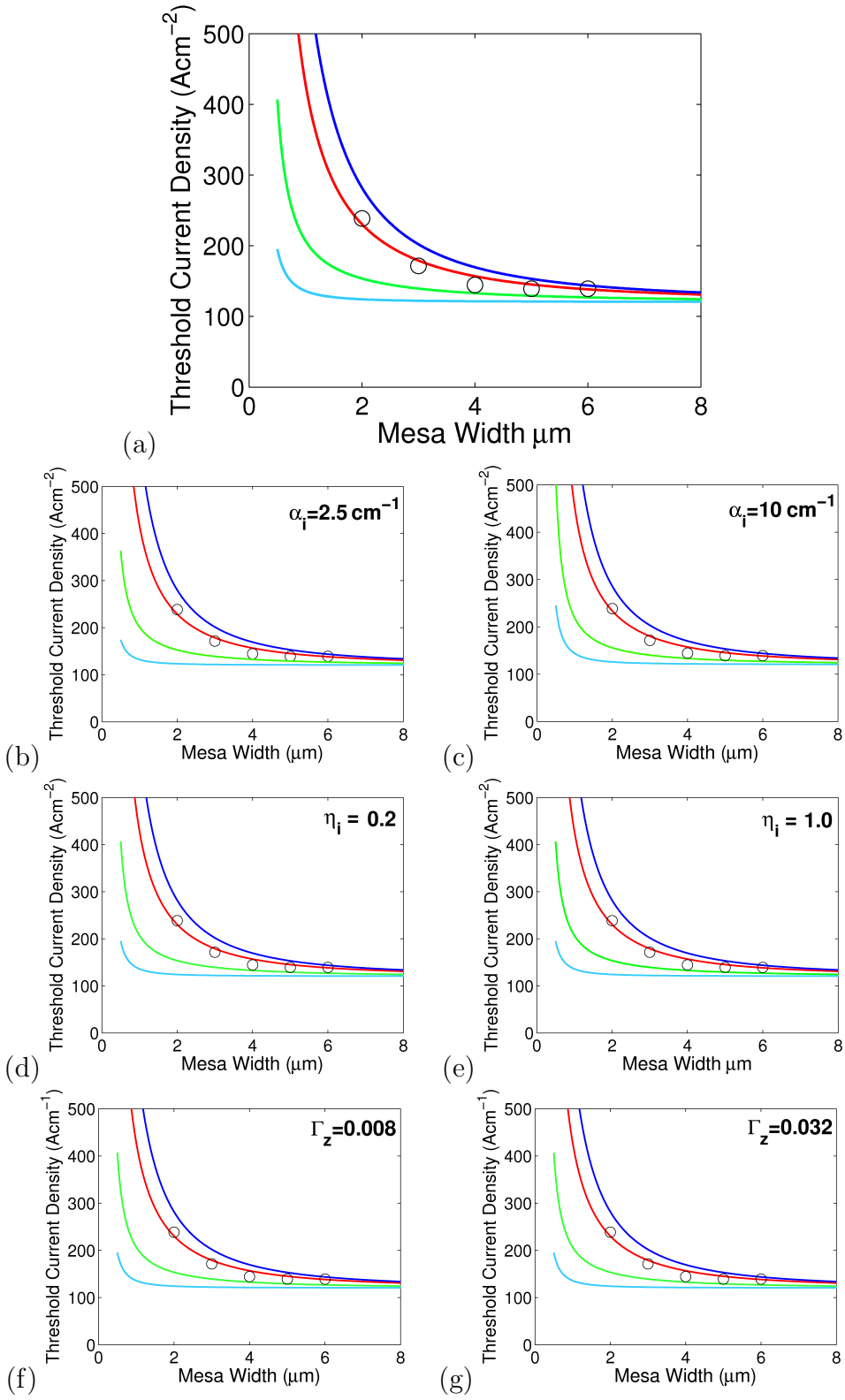

Fig. 6.9: The theoretical dependence of the threshold current density on mesa width for quantum-dot lasers. The experimental data is overlaid. The blue, red, green and cyan curves represent values of ν_s of 1 x 10^5, 5 x 10^4, 1 x 10^4 and 0 cms^{-1} respectively.

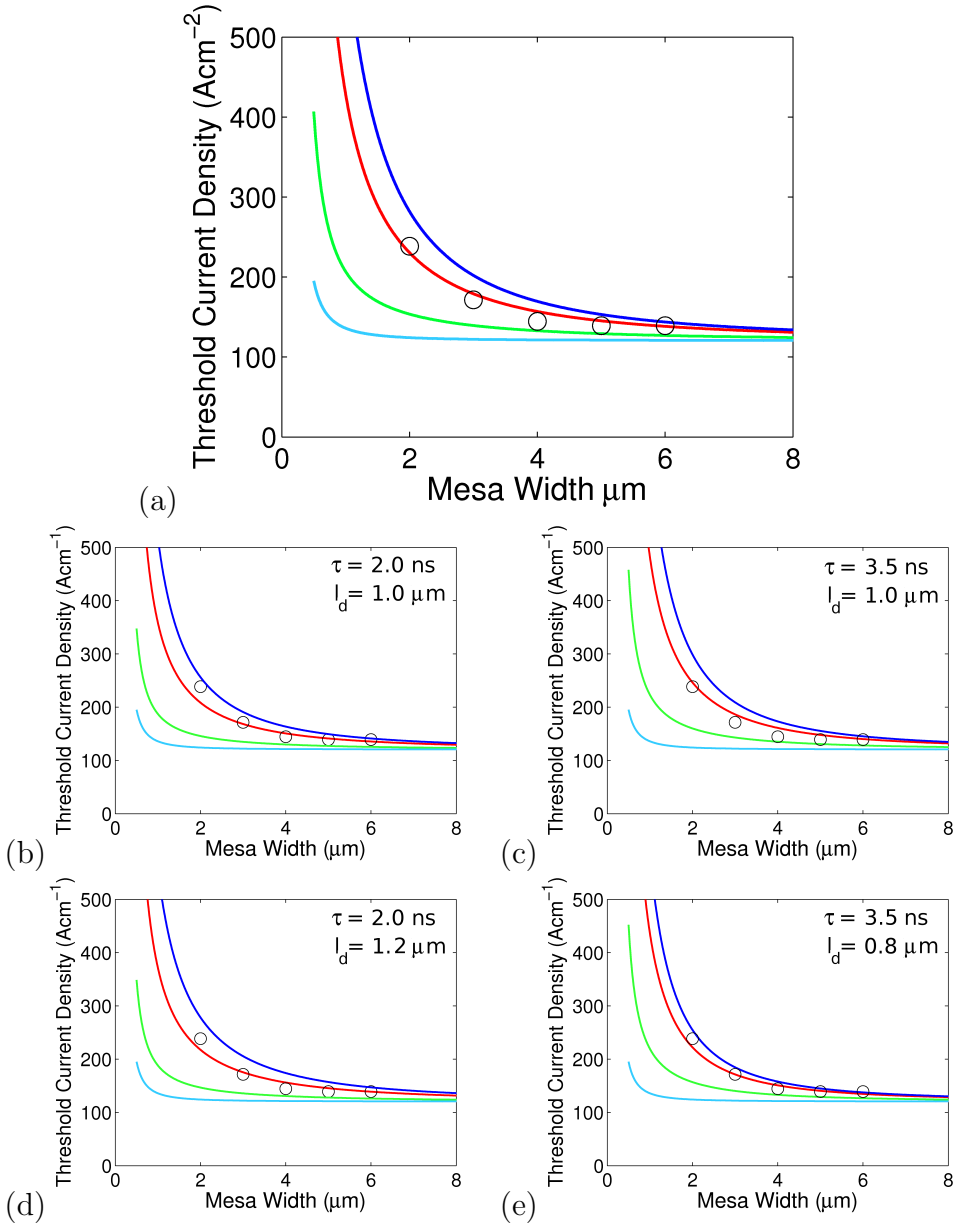

Fig. 6.10: The theoretical dependence of the threshold current density on mesa width for quantum-dot lasers. The experimental data is overlaid. The blue, red, green and cyan curves represent values of ν_s of 1 x 10^5, 5 x 10^4, 1 x 10^4 and 0 cms^{-1} respectively.

6.7 Summary

In summary, a method to determine the surface recombination velocity (ν_s) and diffusion length (L_d) in quantum-dot mesa lasers has been developed. Mesa lasers were fabricated with both quantum-dot and quantum well material. A model was developed to fit theoretical curves to experimental plots of threshold current density versus mesa width. The quantum well devices yielded values of ν_s and L_d of 5×10^5 cms^{-1} and 5 μm respectively. These values agreed well with literature, thus validating the model. The quantum-dot devices yielded values of ν_s and L_d of 5×10^4 cms^{-1} and 1 μm respectively. This was the first report of an experimental determination of ν_s in quantum-dot material [64].

The order of magnitude difference in surface recombination and the reduced diffusion length between quantum wells and quantum dots allows the creation of high-performance, narrow quantum-dot mesa lasers. Importantly, the reduced value of ν_s allows the creation of small device features, having a large surface to volume ratio, with little penalty in device performance. This chapter therefore highlights the suitability of quantum-dot material for photonic crystal lasers, the subject of the next few chapters.

7. FINNED WAVEGUIDES

7.1 Introduction

The first photonic crystal mirror studied was a one-dimensional finned waveguide. The structure, as its name suggests, consists of a waveguide with a comb of teeth etched into the side-walls (figure 7.1). This creates a periodic change in effective refractive index in the direction of propagation of the waveguide. It is in effect a Bragg grating. The structure has previously been proposed as a slow-light time delay structure in silicon [72]. The structure was seen as a potentially simple design that could be used as a dispersion compensating mirror by suitable chirp of the period.

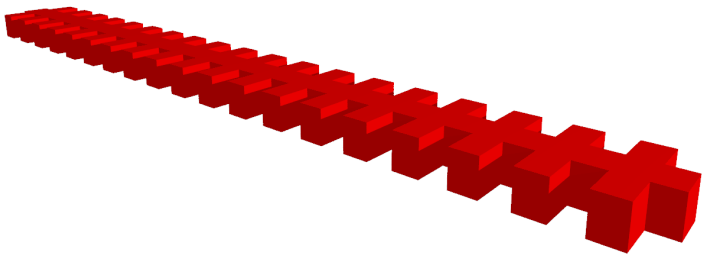

Fig. 7.1: Schematic of a finned Waveguide Structure

In a traditional 1D Bragg grating an entire section is etched away and the grating consists of alternate layers of air and dielectric. Such a grating will act as an excellent mirror at the wavelength that satisfies the Bragg condition:

$$n_{eff}.a = m.\frac{\lambda}{2} \tag{7.1}$$

where m is any positive integer, a is the grating period, λ is the free-space

wavelength and n_{eff} is the effective index of the grating. This Bragg condition is equivalent to a wave-vector at the Brillouin zone boundary, $k = \pi/a$, as described in chapter 3. The mirror will have a very short penetration depth of just a few periods. However, the gratings will have high loss at wavelengths that do not satisfy the Bragg condition and so they are not a good candidate for a dispersion compensating mirror.

The finned waveguide act similarly to a Bragg grating but has the advantage that the centre of the waveguide, where the majority of the optical mode resides, is undisturbed. As a result, the structure has lower loss at non-Bragg wavelengths. The reflectivity at the Bragg wavelength is reduced, due to the reduction of the refractive index contrast, but should be large enough to provide feedback for lasing.

Previous work has been done on similar structures in InP material [73, 74, 75, 76]. This work involved using the grating properties to create distributed feedback (DFB) lasers, optical filters and optical switches. The low surface recombination of the quantum-dot material, shown in the previous chapter, allowed me to extend research of the structure into a GaAs system.

7.2 Design and Fabrication

7.2.1 Design

A quick calculation using equation 7.1 gives a grating period, a, of ~190 nm, for an operating wavelength of 1280 nm (quantum dot gain peak) and an effective index of 3.3. The widths of the two segments were initially set to 0.8 and 1.4 μm corresponding to effective indices of 3.28 and 3.34 respectively. These were calculated using a mode solver with the quantum-dot material structure (table 5.1) and a mesa etch depth of 2.5 μm. The design has a relatively large refractive index contrast and an average effective index of 3.3. The lengths of the two segments were equal i.e. a/2.

7.2.2 Pattern Definition

The structures were defined in ZEP resist using e-beam lithography. Initially the structures were defined as polygons (figure 7.2(a)), but after some early

results, the design was changed to a plain rectangle with a row of 5 single pixel dots to define the fins (figure 7.2(b)). The single pixel dots can be drawn on the pixel grid of the machine and are therefore more useful when trying to work at high resolutions. As mentioned in section 1.2.3, working at the resolution limit of the machine maximises the number of steps in any chirped mirror, thereby producing a better approximation to an ideal smooth chirp.

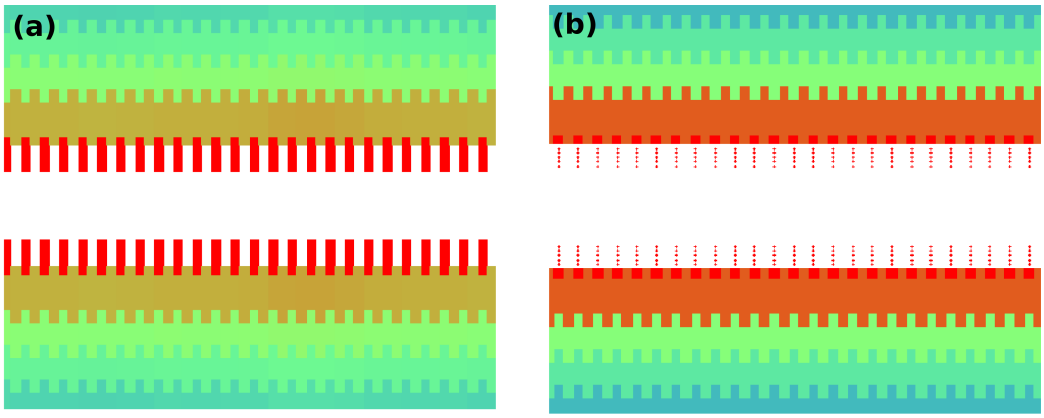

Fig. 7.2: Design patterns for finned waveguides. The design in (a) uses a single polygon shape wereas the design in (b) uses a row of single pixel dots to define the fins. The designs have been proximity corrected.

7.2.3 Hard Mask Etching

After development of the resist, the pattern is transferred to a hydrogen silsesquioxane (HSQ) hard mask using reactive ion etching (RIE) with CHF_3 chemistry. This is the process that was optimised in section 4.3.1. Figure 7.3 shows an SEM image of an etched hard mask from above and from a 45^o angle. A residue can be seen on the sidewalls of the hardmask in figure 7.3(b). This is believed to be a fluoro-carbon polymer formed from the by-products of the etching process. Various techniques were used in an attempt to remove this residue including further RIE etching with Oxygen and Argon chemistry and various solvent and acid mixtures. The residue could not be removed without damaging the profile of the hardmask. After some research it became obvious that this is a common, and as yet largely unsolved, problem in the semiconductor IC industry and has even been the subject of an entire PhD

thesis [77]. The remnants of the ZEP resist, in contrast, can be removed with a five minute, low power, Oxygen RIE etch.

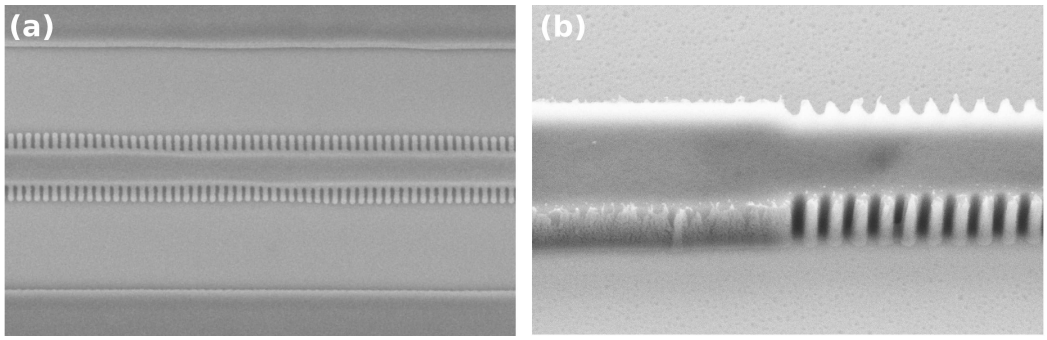

Fig. 7.3: SEM images of HSQ finned waveguide hardmask post-RIE-etching. (a) Top (b) 45^o angle. The images were taken after removal of the Zep e-beam resist.

7.2.4 Semiconductor Etching

The next step in the process is to transfer the pattern to the quantum dot material. This is done using chemically assisted ion beam etching (CAIBE). The large etch depths required ($\sim 2\mu$m) make this a difficult task for such fine features ($\sim$ 100 nm fins). The best etching results achieved are shown in figure 7.4(a). A high beam voltage/high beam current regime (1450V/16mA) was used and the sidewalls are vertical. Figure 7.4(b) shows a roughness on the sidewalls. This is not so apparent in figure 7.4(a) due to the use of a low energy secondary electron SEM detector which tends to to show less surface topology but more material contrast than the high energy secondary electron detector used for figure 7.4(b). I believe that the roughness arises from the gradual breakdown of the hardmask residue discussed above.

7.2.5 Electrical Contacts

Passive finned waveguide devices would be finished after the CAIBE etch step, whereas active devices require electrical contacts. An insulation layer of SU:8 is put down using an e-beam overlay exposure. The devices are then dipped in HF:H_2O 1:10 for 2 minutes to remove any remaining HSQ, before the metal contact layers are deposited as described in chapter 4.

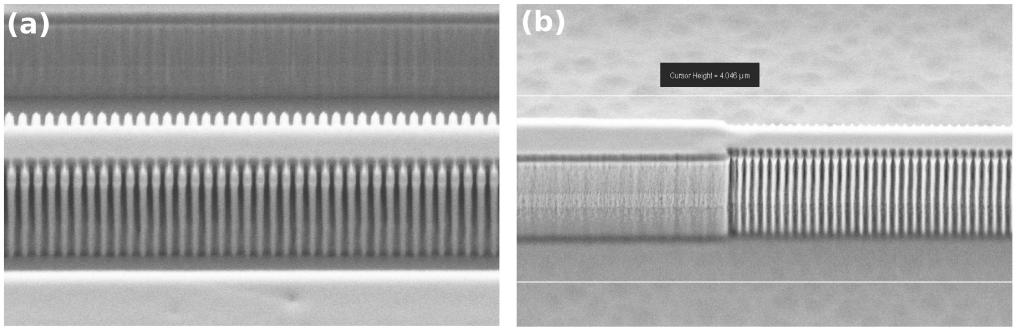

Fig. 7.4: SEM image of finned waveguides post CAIBE etching. (a) shows some of the best etching achieved and (b) higlights a surface roughness issue

7.3 Results

7.3.1 Passive Transmission Measurements

The first finned waveguide devices to be tested were simple passive waveguides. These devices were probed around a wavelength of 1300 nm to look for transmission dips that correspond to the fundamental band-gap of the finned waveguide. The sample consisted of 3 μm wide access waveguides (input and output) that tapered down to the 100 period long finned waveguide. The sample had numerous devices with a range of periods (180 nm to 230 nm). The transmission spectrum for a finned waveguide with a period of 215 nm is shown in figure 7.5. The first obvious feature is the absorption edge at 1300 nm that was previously seen in figure 5.6. The other main features are the strong Fabry-Perot resonances at wavelengths above 1300 nm. These strong resonances are due to reflections at the device facets. The combination of theses resonances and the strong absorption below 1300 nm made identifying any spectral features of the finned waveguides very difficult. An alternative measurement technique was therefore sought.

7.3.2 Internal Source Measurements

Idea

To avoid the undesirable Fabry-Perot resonances, the "on-chip" active quantum-dot material was used as the source for probing the finned waveguides. The

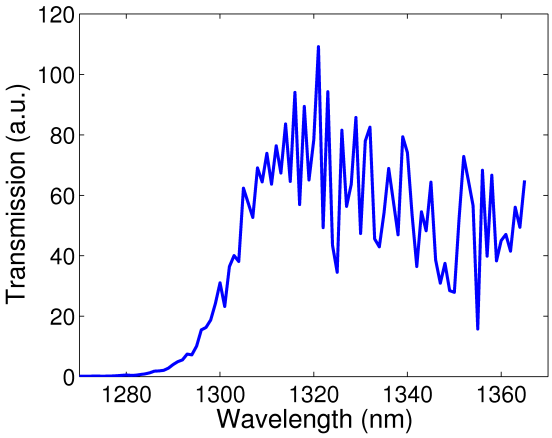

Fig. 7.5: Transmission of 1300 nm tunable laser source through a passive finned waveguide.

material has a broad ($\sim$ 100 nm) amplified spontaneous emission (ASE) spectrum and is therefore an excellent source for characterising the finned waveguides. To use this ASE requires prevention of lasing and this can be achieved by leaving one facet un-cleaved (similar to approach in section 5.3.1). Electrical pumping was used and a large section of the device was fabricated with an electrical contact. This section was a 10 μm wide, 2 mm long waveguide that tapered down to the 800 period long finned waveguide. A schematic of an internal source device is shown in figure 7.6.

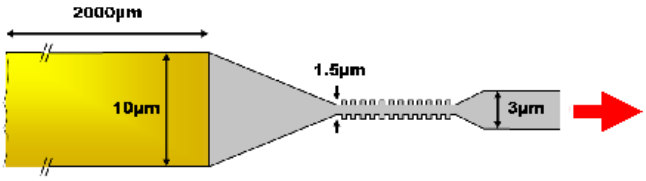

Fig. 7.6: Schematic of an internal source device for measuring transmission spectrum of a finned waveguide

Results

A set of internal source devices, with a range of periods (190 nm to 240 nm), was fabricated. The sample also contained a blank waveguide (no fin), as

a normalisation reference. The transmission spectra were measured using a optical spectrum analyser (OSA). Figure 7.7(a) shows the output obtained from a blank device and from a finned device and 7.7(b) shows the transmission from the finned device normalised against the blank.

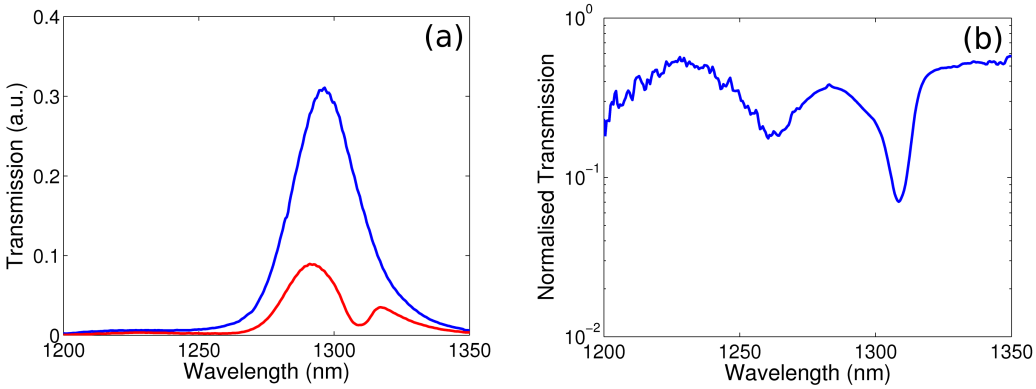

Fig. 7.7: (a) Transmission spectrum of a blank waveguide (blue) and a 240 nm period finned waveguide (red) from an internal source device. (b) Normalised transmission of 240 nm period finned waveguide

All measurements were normalised in this manner and the results are plotted together in figure 7.8. The largest transmission dips are approximately 10 dB in magnitude.

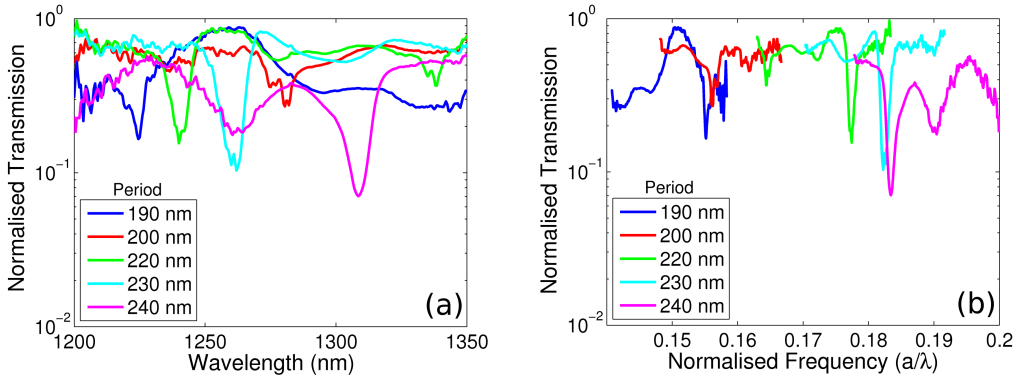

Fig. 7.8: Normalised transmission spectra for finned waveguides from an internal source plotted against (a) wavelength and (b) normalised frequency.

The plot against normalised frequency shows two main transmission dips at $a/\lambda = 0.155$ and $a/\lambda = 0.18$. The physical origin of these dips is discussed

towards the end of the chapter. The spectral tuning of the dips as a function of period can be found by examining two equivalent dips. For example, the dips for 230 nm and 240 nm periods at $a/\lambda \sim 0.18$ correspond to a wavelength difference, $\Delta\lambda$, of ~ 50 nm in figure 7.8. The spectral tuning with period can be estimated as

$$\frac{\Delta\lambda}{\Delta a} \sim \frac{50\ nm}{10\ nm} \sim 5. \tag{7.2}$$

This value can be derived theoretically from the normalised frequency (a/λ). Simple inspection shows that $da/d\lambda$ is simply the inverse of the normalised frequency. Inspection of equation 1.3 shows that this tuning rate would only allow one chirp step for any dispersion compensating mirror. The period of a finned waveguide is therefore not a suitable chirping parameter for a dispersion compensating mirror.

Long Wavelength Passive Measurements

The longer period devices were also characterised with a broadband LED source centred at 1550 nm. The sample was cleaved at the previously uncleaved end for characterisation. The normalised transmission is plotted in figure 7.9 against wavelength and normalised frequency. The dips in normalised transmission are now at ~ 0.16, slightly higher than the value of 0.155 seen in figure 7.8(b), but within the experimental error.

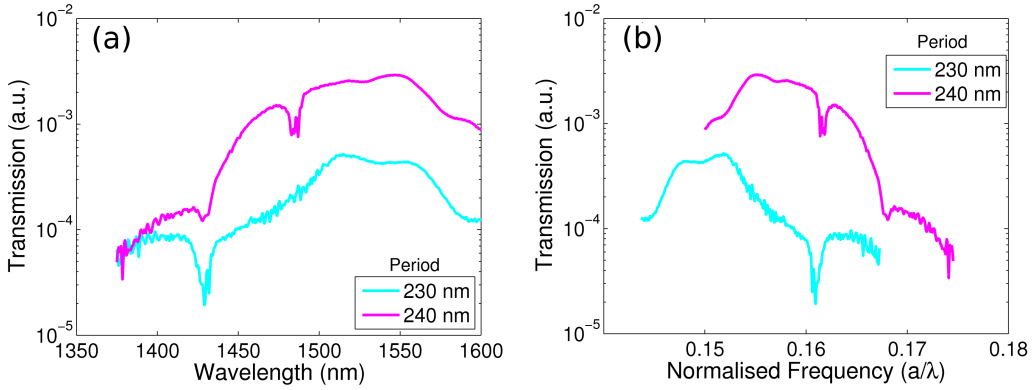

Fig. 7.9: Normalised transmission spectrum, of 230 nm and 240 nm period finned waveguide devices, plotted for (a) longer wavelength and (b) lower normalised frequency.

7.3.3 Continuous-Wave Lasing Tests

A duplicate sample of the internal source devices was fabricated for lasing tests. The opposite end was cleaved in order to use the finned waveguide as a laser mirror. Lasing was only observed under high excitation ($\sim$ 100 mA) and was also observed in the device with no fin. The thresholds observed were approximately 3 times higher than the 10 μm devices characterised in chapter 6. This suggests that the lasing feedback mainly orginates from interface mode mismatch (possibly at the taper) and not from feedback from the fin. One device, with a period of 220 nm, did have a slightly lower threshold of 60 mA suggesting that the fin may have provided some feedback (figure 7.10(a)).

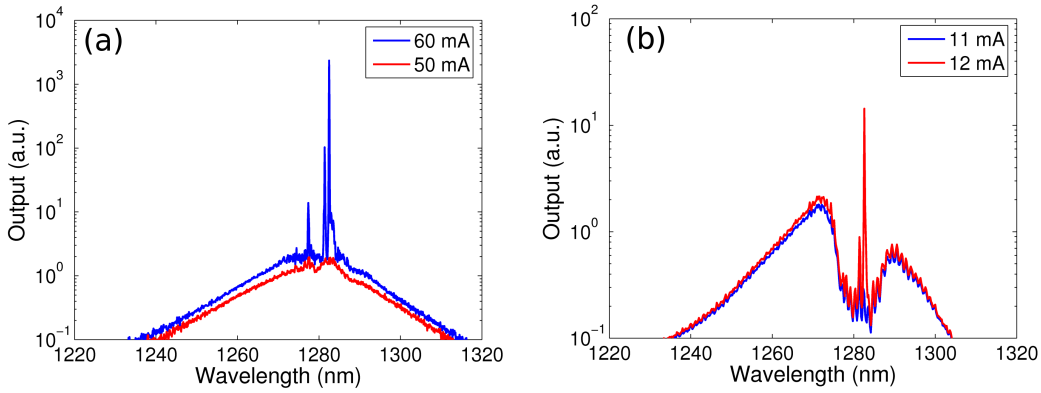

Fig. 7.10: OSA spectra of 220 nm period finned waveguide laser output for (a) fin as stand alone mirror and (b) additional facet beyond fin. Spectra in (b) are for the output transmitted through the fin.

The other end of the sample was cleaved and the output through the fin examined to confirm whether the fin was providing any feedback. Every device lased via feedback from the two cleaved facets and this reduced the threshold current. Figure 7.10(b) shows the OSA output from the 220 nm period device. The figure clearly shows that the lasing is occurring at the centre of the fin transmission dip. This suggests that the fin is providing feedback and that this led to the reduced threshold observed earlier. However, the finned waveguide was 800 periods long and the transmission dip is at the centre of the material gain (1280 nm). These conditions are very favourable for lasing, yet bot ends of the device had to be cleaved to obtain a reasonable threshold value. This suggests that although the fin is introducing some wavelength specific feedback,

the reflection is very low. Figure 7.11 shows a lasing spike for a 210 nm period device on the lower side of the gain spectrum at 1265 nm. This confirms the wavelength selective feedback of the finned waveguides with lasing observed away from the material gain peak.

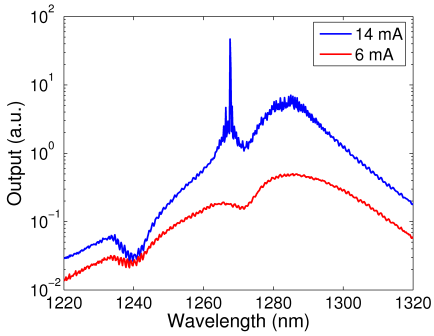

Fig. 7.11: OSA spectra of 210 nm period finned waveguide laser output transmitted through the fin end of device.

In summary, the cw lasing results were not as promising as was hoped. Figures 7.11 and 7.10 indicate that the fin does provide wavelength selective feedback. However, the fin does not act well as a stand-alone mirror and results in high thresholds. The fin seems to be acting more like a DFB element than a stand-alone distributed bragg reflector (DBR). This may be why the previously mentioned InP work [76] only produced a DFB laser and not a DBR.

7.4 Simulations

The disappointing lasing results were unexpected and some simulations were performed to try to explain the results. As discussed above, the finned waveguide acted more like a spectral filter than a complete reflector. To understand this operation better, I conducted simulations of the finned waveguide transmission and reflection properties using the finite difference time domain (FDTD) method. A commercial FDTD software package, Rsoft Fullwave, was used for the calculations. A 40 period finned waveguide with dimensions matching those fabricated above was defined (figure 7.12). The structure length was only 40 periods to maximise simulation speed. The figure also shows the launch position (yellow bar) and detector positions (green bars).

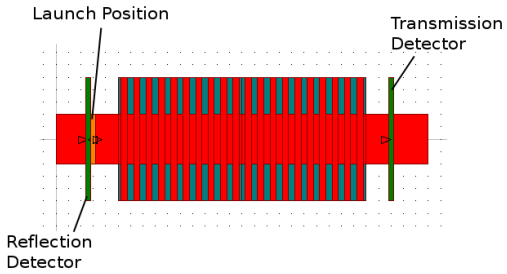

Fig. 7.12: Design layout for FDTD simulations

Figure 7.13 shows the normalised transmission and reflection response from the 40 period finned waveguide. The transmission and reflection is shown for the fundamental mode (blue and red plots). Two large transmission dips are visible at normalised frequencies of 0.16 and 0.19. These are very close to the experimentally observed dips(figures 7.8(b) and 7.9(b)). There is no corresponding reflection into the fundamental mode of the access waveguide. There is a field response in reflection at these wavelength suggesting that the reflection excites higher order modes. The simulations indicate that the finned waveguide is a more complicated structure than the simple Bragg grating approximation assumed prior to fabrication!

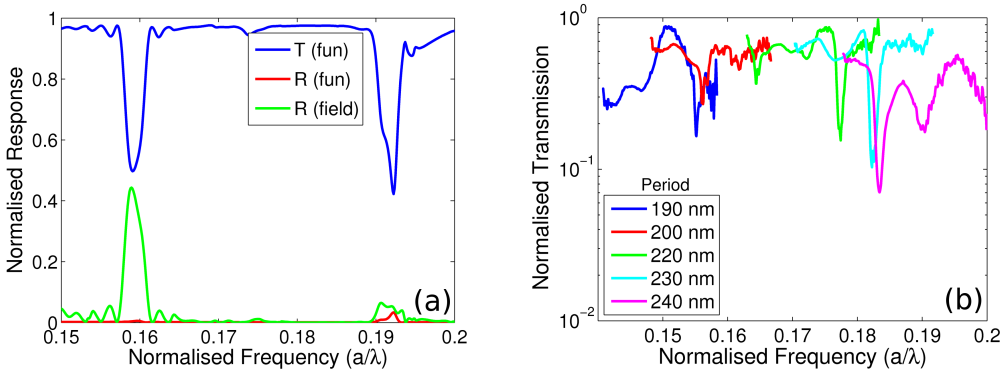

Fig. 7.13: (a) Calculated transmission (blue) and reflection (red) from a finned waveguide into the fundamental mode. The field reflection (green) is also shown. (b) Experimental transmission results (figure 7.8(b)) shown for comparison.

7.5 Summary

In summary the concept of a finned waveguide has been introduced and some properties explored. A good fabrication process has been developed. Transmission measurements showed two sharp dips at normalised frequency values of 0.155 and 0.18. Laser devices were fabricated and cw lasing was observed using the finned waveguide as a mirror but with high thresholds. Further investigation implied that the finned waveguide was acting more like a wavelength filter than a stand alone reflector. FDTD simulations showed that the transmission dips observed did not correspond to large reflection peaks into the fundamental mode.

7.6 Discussion

At this point, a decision was taken to look for an alternative mirror to the finned waveguide. There were a few reasons that led to this decision.

- The fabrication of these "simple 1d devices" was actually very difficult. There are a few parameters needed to define a fin - width, period, grating depth, wide length/narrow length ratio etc. One small shift in any of these parameters can cause a significant change in spectral properties. The e-beam lithography and dry etch steps can lead to such shifts and, as a result, repeatability was an issue.

- The poor performance of the laser devices discussed above.

- The FDTD simulations also suggested any reflections would be multimode. This is undesirable and would also lead to complications when designing any dispersion compensating mirror. To make the thinner section narrow enough (800 nm) to support the fundamental mode would complicate fabrication further and lead to higher loss.

- The tuning rate of the Bragg wavelength with period was too large to design a suitable group delay element for a dispersion compensating mirror within the constraints of e-beam lithography.

All of this is not to say that the finned waveguides are not a useful system. They have already been used in literature and with better fabrication

conditions could have been pursued further here. The high tuning could be addressed by adjusting a different parameter to the period. With hindsight, some thorough simulations could have been performed before experimental work commenced but the system seemed elegantly simple and simulations were deemed unnecessary.

The next chapters explore the use of a photonic crystal defect waveguide as a laser mirror. These 2d structures were originally thought to be more complex than a finned waveguide. However, they only have two parameters to define them – period and radius – making fabrication simpler. The central waveguide defect is also much wider ($\sim$ 1.5 μm) further reducing fabrication difficulty. Despite this wide central defect, the system still operates on the fundamental mode, eliminating any multi-mode complexity. My research group has extensive experience with photonic crystals and there is a large volume of literature to consult. The reduction in fabrication difficulty and the strong knowledge support (along with the disappointing finned waveguide results) were the main driving forces behind the decision to change mirror structure.

8. PHOTONIC CRYSTAL W3 DEFECT WAVEGUIDES - THEORY AND PASSIVE DEVICES

8.1 Introduction

A general introduction to photonic crystals was given in chapter 3. The concept of defect structures was also introduced. The next few chapters look at the potential of using a photonic crystal defect waveguide as a laser mirror for CW and mode-locked operation.

The defect to be studied as a potential laser mirror consists of a photonic crystal with three missing rows of holes, typically referred to as a W3-type waveguide [78]. A standard W3 waveguide is twice the width of a W1 ($2\times\sqrt{3}a$). The typical band structure of a W3 waveguide is shown in figure 8.1 (taken from [79]). The figure illustrates that several transverse modes are supported within the band-gap. Close inspection of the figure reveals that different order modes cross in one of two ways. Firstly, in some cases, modes cross each other without any interference, this is known as a crossing. In other instances, modes interfere with one another causing a discontinuity in their profiles. This type of interference is known as an anti-crossing. The parity of two modes determines what type of crossing they will form. Modes of the same parity will form an anti-crossing [80]. The discontinuity arising from an anti-crossing leads to spectral regions where neither of the modes involved in the anti-crossing are supported. These regions are known as mini-stopbands (MSB) and act like a mini-band-gap for the modes involved. There are three MSBs visible in the band-structure. The MSB involving the fundamental and 4^{th} order mode is shown in more detail in the figure. This MSB will be highly reflective for the fundamental mode and is the feature of the W3 that will be examined as a

potential high reflectance, single mode laser mirror.

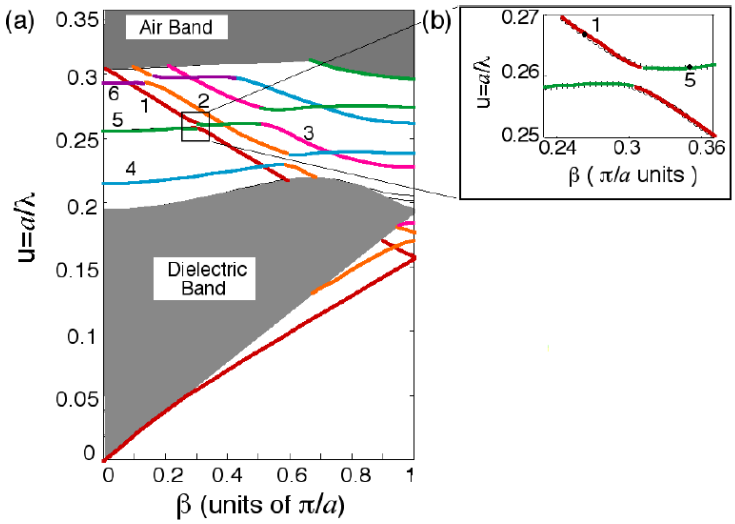

Fig. 8.1: Theoretical band-structure of W3 defect photonic crystal taken from [79].

8.2 Band Structure Modeling

8.2.1 Overview

The band-structure of the W3 waveguide was studied using the open-source plane-wave expansion package "MIT Photonic Bands (MPB)" [81]. MPB is a frequency domain technique specifically designed for photonic crystals and is therefore an excellent package for calculating W3 band-structures.

The software requires a unit-cell or a super-cell for calculation. A unit cell is used to compute bulk photonic crystal band structures. A super-cell is used to calculate defect structures, such as photonic crystal cavities and defect waveguides. A super-cell typically consists of multiple unit cells with a line or point defect. A supercell will be repeated periodically like a unit-cell and therefore the dimension that is not periodic in reality needs to be large. The super-cell of a W3 is shown in figure 8.2. The software works by setting the fields at opposite boundaries of a unit-cell (or super-cell) to be equal:– periodic boundary condition. As a consequence, it calculates the band structure of an infinite lattice.

The calculations in this section are two dimensional. This assumes that the photonic crystal is infinite in the z-direction (parallel to the holes). This is a valid assumption here, as the waveguide structure is single-mode in the vertical direction. Even though there are losses, the mode can be assumed to interact with the crystal lattice as if the structure is vertically invariant, as there is little index variation in the z-direction (table 5.1).

8.2.2 Calculations

A Basic W3

Initially, a standard W3 band-structure was calculated to test that the software had been set-up correctly. The W3 studied had a radius of $0.3a$ (where a is the photonic crystal period) and a dielectric refractive index of 3.2. The supercell of the structure is shown in figure 8.2. The resulting band-structure is shown in figure 8.3(a). This band-structure agrees with figure 8.1 indicating that the software was working correctly. The MSB that involves the fundamental and 4^{th} order mode at a normalised frequency of ~ 0.27 is shown in greater detail.

Fig. 8.2: Schematic of the supercell used to model the band-structure of a W3 waveguide in MPB

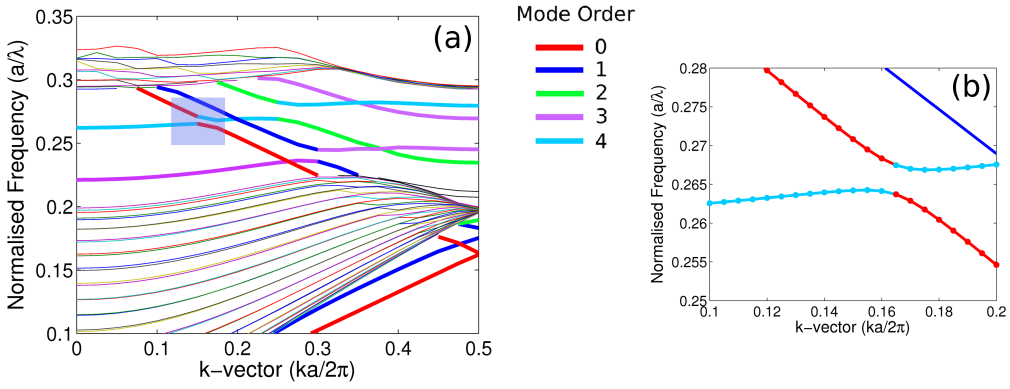

Fig. 8.3: Theoretical band-structure of W3 defect photonic crystal calculated using MPB. The calculation uses the supercell shown in figure 8.2.

The individual modes labelled in the band-structure were determined with the MPB software to confirm agreement with figure 8.1. This was done by studying the field profiles. These profiles can only be calculated for a single k-vector at a time. The field profiles for the modes that lie within the band-gap are shown in figure 8.4 for three different k-vectors. The mode profiles show correspondence with figure 8.1 and the various modes in figure 8.3 were labelled by studying several of these plots.

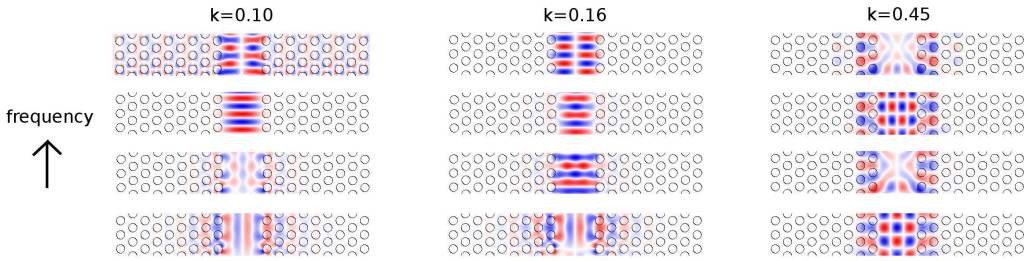

Fig. 8.4: Field profiles of W3 waveguide modes that lie within the band-gap for three different k-vectors. The modes correspond to the labelling in figure 8.3.

The middle two modes at $k = 0.16$ correspond to the edges of the MSB. This is the location where the fundamental and fourth order modes interact and anti-cross. It is clear in the figure that neither of the mode profiles look strictly fundamental or strictly fourth order and that both modes appear more like a combination of the two. The MSB therefore has strong potential as a single fundamental mode laser mirror as the fourth order mode is typically not highly excited in a semiconductor laser.

Variation of Defect Width

As described in chapter 1, one potential application for a photonic crystal laser mirror was pulse compression, via group delay dispersion (GDD), in a mode-locked laser. In order for the mirror to operate as a dispersion compensating element, the spectrum of the reflection peak should vary with some physical parameter. One of the drawbacks of the fin structure, discussed in section 7.3.2, was that the tuning rate of the spectral position of the band-gap with period was too high. In a W3, the variation of MSB position with period is also very strong (λ /a). Another physical parameter that has a smaller effect on the

spectral position of the MSB is required.

The modeling software was used to check the strength of the spectral tuning with defect width in a W3 waveguide[1]. The position of the MSB was calculated for a range of defect widths around a standard W3 (figure 8.5). It can be seen in the figure that the tuning is quite linear. The strength of the tuning $d\lambda/dW$, where W is the defect width is approximately 0.75. Inspection of equation 1.3 reveals that this tuning rate would allow six steps, which is a reasonable approximation to the ideal smooth chirp.

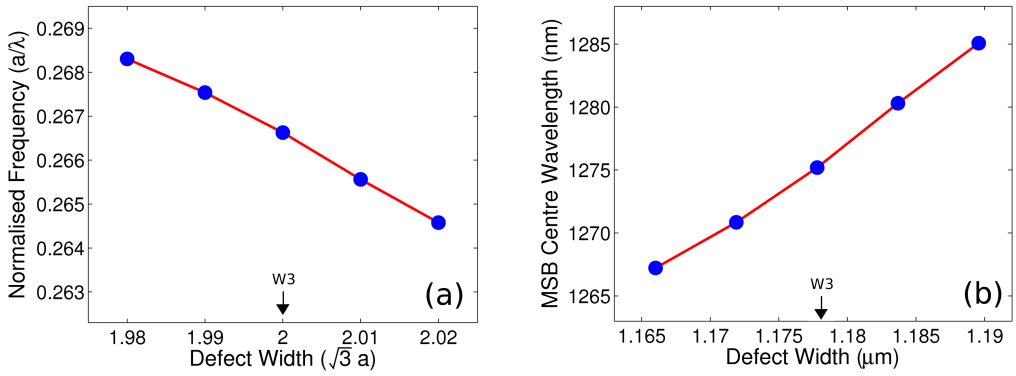

Fig. 8.5: Variation of the MSB centre wavelength with defect width. (a) shows the tuning in normalised units and (b) shows actual wavelength and defect width assuming a period of 340 nm

Variation of Hole Radius

A similar calculation was done to study the tuning of the MSB spectral position with hole radius. The results are shown in figure 8.6. The strength of the tuning in this case, $d\lambda/dr$, is approximately unity. However, when fabricating these devices, it is the diameter, D, that matters for EBL and so the tuning can be assumed to be $d\lambda/dD \sim 0.5$.

This tuning rate, for the hole radius, appears more attractive than $d\lambda/dW$, but in reality it is more difficult to realise. The best way to chirp the hole radius smoothly would be to vary the dose in incremental steps. However calculating this dose step would be problematic as measuring hole radii with nanometer precision is difficult, even with an SEM. In contrast, the defect

[1] The waveguides will not be strictly W3s anymore when the defect width is changed.

width is a better controlled parameter that is laid out on the design grid of the EBL and so this method would be a better candidate for the fabrication of a dispersion compensating mirror.

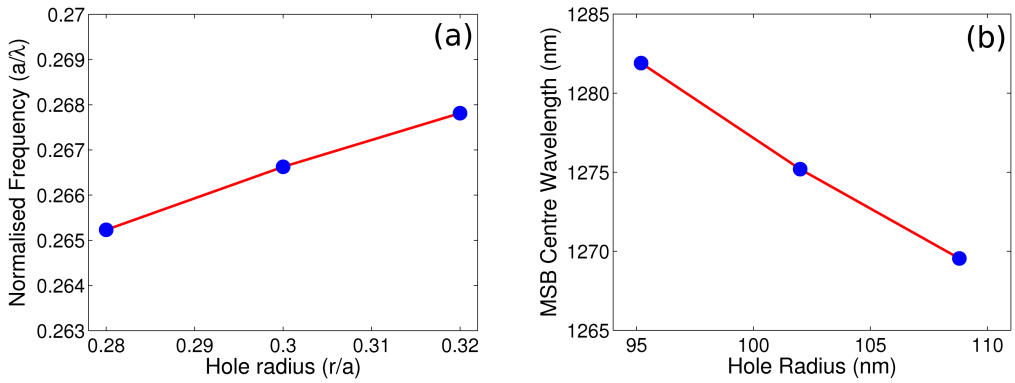

Fig. 8.6: Variation of the MSB centre wavelength with hole radius. (a) shows the tuning in normalised units and (b) shows actual wavelength and radius assuming a period of 340 nm

8.3 Fabrication

The optimised fabrication process for the W3 photonic crystal structures was found to be very similar to that of the finned waveguides, described in section 7.2. Zeon Chemicals ZEP 520A electron beam resist was used and the reactive ion etch (RIE) recipe, for the HSQ hard mask, was the same. A SEM image of a proximity corrected, patterned hard mask, from above and at a 45^o angle, is shown in figure 8.7. The ZEP resist was left on for the chemically assisted ion beam etch (CAIBE) step to provide some extra mask toughness that allows for longer etch times. The optimised CAIBE etch used a lower voltage and current (600V/10mA) than the finned waveguide recipe. High CAIBE voltages were found to erode the HSQ mask before a sufficient photonic crystal hole depth was reached. A SEM image of the best CAIBE etching is shown in figure 8.8. Passive devices are ready for characterisation after the deep etch step. For active devices, described in the next two chapters, SU8 electrical insulation pads were created via an over-lay e-beam lithography exposure and electrical contacts were deposited via electron beam evaporation and a lift-off

step.

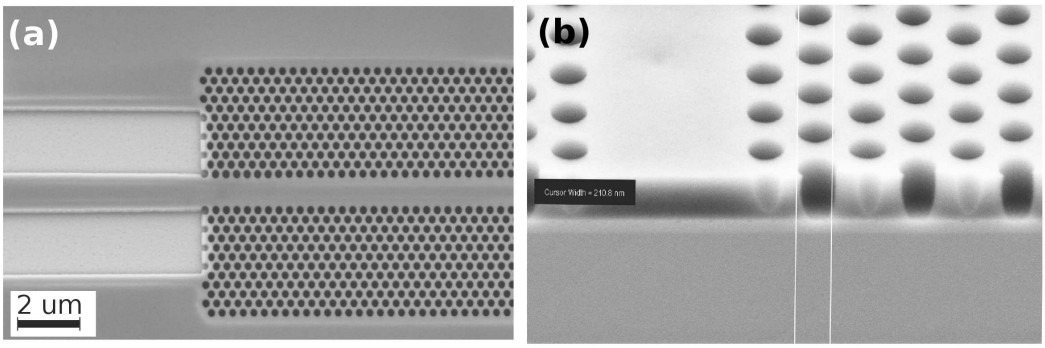

Fig. 8.7: (a) Top down and (b) 45^o angle SEM images of a patterned, proximity corrected W3 HSQ hard mask.

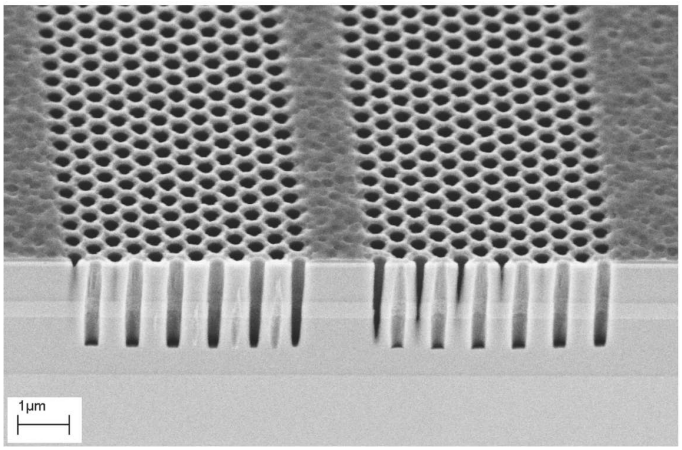

Fig. 8.8: SEM image of deeply etched photonic crystal holes. The rough surface is due to remnants of the HSQ hard mask.

8.4 Passive Characterisation

The spectral transmission of W3 photonic crystal defect structures and their suitability as laser mirrors was studied by fabricating a range of passive devices. This also had the benefit of improving processing techniques through continuous iterations of the fabrication process. The measurements were taken using a simple transmission line set-up and an Optical Spectrum Analyser (OSA).

The sources used were an ASE source centred at 1550 nm and a white light source (700 nm–1700 nm). A tunable laser centred at 1300 nm was used to optimise the signal at 1340 nm and the white-light source was then used to obtain a broad spectrum around this wavelength. The measurements are described in detail below and include transmission, loss and defect width tuning properties.

8.4.1 Standard W3 Transmission

The first set of devices were simple W3-defect waveguides to locate the spectral position of the MSB. The period of these device was designed to find the MSB at a wavelength of 1550 nm. The reasons for initially choosing this long wavelength were due to the availability of brighter sources at this wavelength (an Erbium doped fibre amplified spontaneous emission source (ASE)) and to aid fabrication (bigger holes). A quick calculation using figure 8.3, in which the MSB lies at ~ 0.27, implies a period of $a = 1550 \times 0.27 \sim 420\ nm$. A wide range of periods (340–470 nm) was fabricated to allow for errors and to allow for the possibility of probing the MSB of a shorter period device with the 1300 nm source. Each device was 60 periods long.

The spectral transmission for some of the longer period devices is shown in figure 8.9(a). The MSB is clearly visible and can be seen to tune with period as expected. To highlight this, figure 8.9(b) shows the normalised spectra. All the MSBs lie around a normalised frequency of 0.27, as expected. The signal strength within the MSB was very weak and below the noise level for the sensitivity setting used on the OSA. Figure 8.9(b) also shows a spectrum for a 360 nm period device. The MSB of this device was at 1340 nm which is much closer to the quantum-dot peak gain wavelength of 1280 nm. This spectra was taken at the highest sensitivity[2] setting of the OSA to get a sense of the true depth of the MSB (figure 8.10). The signal level within the MSB was still below the noise level, but figure 8.10 indicates that the attenuation in transmission is at least 20 dB. Assuming most of this is due to reflection, a W3 should make an excellent laser mirror (bare facet reflectivity ~ 3 dB).

[2] Only the 360 nm period device was taken at the highest OSA sensitivity as these spectra take a very long time to scan.

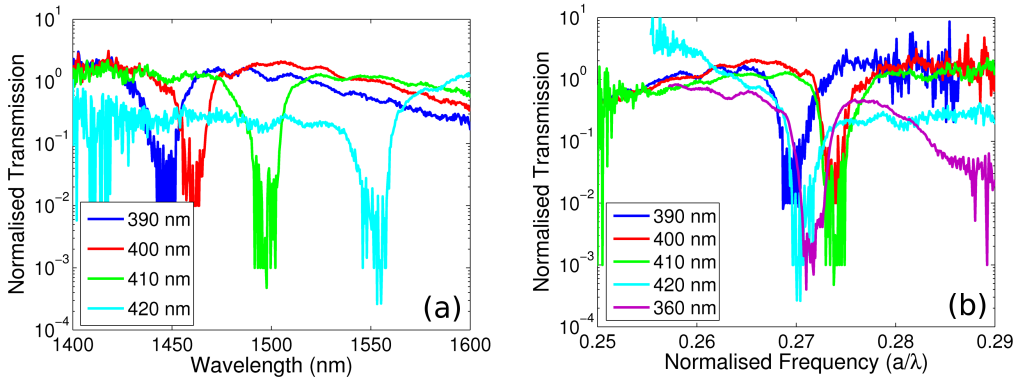

Fig. 8.9: Spectral transmission of 60 period long W3-defect waveguides for a range of periods. The MSB is clearly visible as the large dip in transmission. The spectra are plotted against (a) wavelength and (b) normalised frequency.

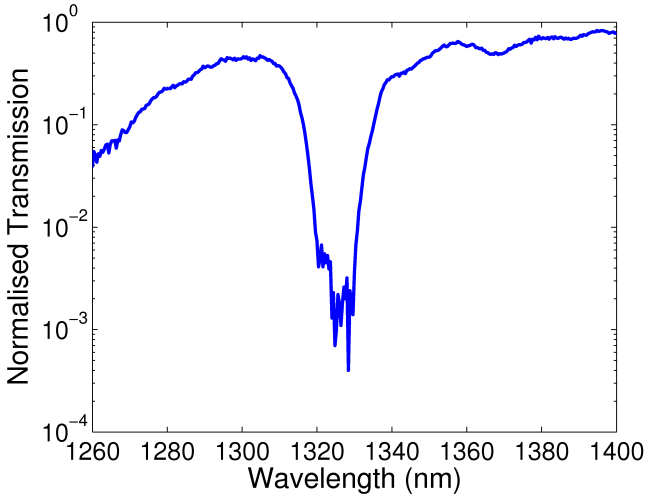

Fig. 8.10: Spectral transmission of 360 nm period W3 device measured using the highest sensitivity setting on the OSA. The MSB attenuation is at least 20dB.

8.4.2 Passive Optical Loss

Any W3 laser mirror will be an un-pumped region and therefore the passive optical loss of the W3 should be low to avoid high thresholds. The passive optical loss of the W3s was measured using the cut-back technique. This technique calculates the loss by comparing the transmission through a range of different device lengths. The loss is measured in dB/unit length, so the

transmission through a device of length L can be written as:

$$I_L = I_0 10^{-\frac{\alpha L}{10}} \tag{8.1}$$

where I_L is the intensity of light transmitted through a length L, I_0 is the initial intensity and α is the passive optical loss. It can be seen from equation 8.1 that a plot of $10\log(I_L)$ versus L will give a straight line of gradient $-\alpha$ measured in dB/unit length.

A set of W3 devices with a period of 355 nm covering a range of different W3 lengths (58 μm to 1 mm) were fabricated and characterised using the white light source and the OSA. The output spectra are shown in figure 8.11(a). An error in the EBL fabrication step led to a slight inconsistency in defect width which results in the inconsistency in the MSB position. However, the data on the long wavelength side can still be used for a loss calculation. This side of the MSB is away from the absorption region of the quantum dot material making it a good region for a loss measurement. The calculated loss spectrum is shown in figure 8.11(b). The passive loss is ~10 dB/mm, which is low enough for use as a laser mirror, particularly as field penetration into the W3 will only be a few periods.

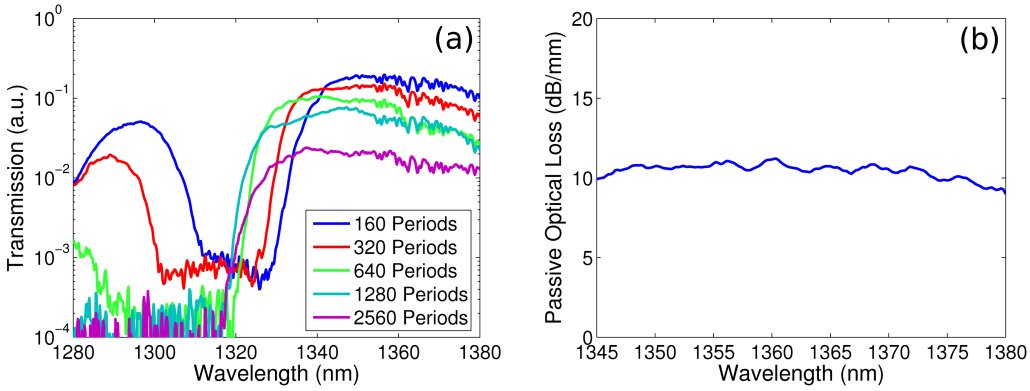

Fig. 8.11: (a) Spectral transmission of 355 nm period W3 structures for a range of device lenghs. (b) Calculated loss spectrum using data in (a).

8.4.3 Defect Width Tuning

In section 8.2.2, simulations calculated the rate of tuning of the MSB position with defect width ($d\lambda/dW$) to be approximately 0.75 (figure 8.5). The calculation was only 2D and so an experimental verification of the result was desirable. A set of photonic crystal defect waveguides with varying defect width and a fixed period of 360 nm was fabricated. The defect width ranged from 0.9 to 1.1 times a standard W3 width. The MSB centre wavelength is shown as a function of defect width in figure 8.12. The gradient of this plot gives the tuning rate, $d\lambda/dW$, and is equal to 0.865. This value is in good agreement with the 0.75 value obtained via simulation in section 8.2.2

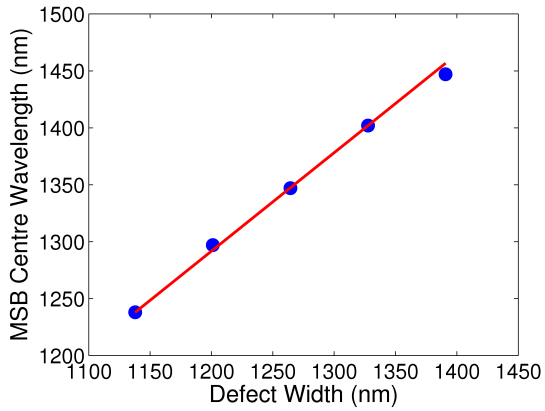

Fig. 8.12: Spectral postion of MSB centre wavelength as a function of defect width for 360 nm period devices. The centre value is a standard W3.

8.5 Summary

In summary, this chapter has studied some basic properties of a W3 defect waveguide and its potential as a laser mirror. Theoretical band structures have been calculated. The MSB resulting from the anti-crossing of the fundamental and fourth order modes should act as a single fundamental mode reflector in a semiconductor laser.

The variation in spectral position of the MSB as a function of defect width ($d\lambda/dW$) and hole radius ($d\lambda/dr$) has been studied theoretically and found to

be 1.0 and 0.5 respectively. These low tuning values indicate that a W3 could potentially be used as a dispersion compensating mirror.

Fabrication of deeply etched photonic crystals was optimised. Experimental passive measurements confirmed the spectral position of the MSB and obtained a passive loss value of ∼10 dB/mm, low enough for a short laser mirror. An experimental measurement of $d\lambda/dW$ yielded a value of 0.7, slightly less than predicted in theory.

In comparison with the finned waveguides studied in the previous chapter, the W3 appears more suitable as a laser mirror. Firstly their ease of fabrication, highlighted by the repeatability in spectral position of the MSB is a definite advantage. Their potential for single mode operation is another improvement. Additionally, the attenuation of the W3 was greater than 20 dB for only a 60 period device which compares very favourably to the 10 dB attenuation observed for a 800 period finned waveguide. Finally, the slow tuning rate of the MSB with hole radius and defect width suggests potential for a dispersion compensating mirror. I believe the above advantages fully justify the decision to change mirror structure at the end of chapter 7.

9. PHOTONIC CRYSTAL W3 DEFECT WAVEGUIDES - CONTINUOUS-WAVE LASER MIRRORS

9.1 Introduction

This chapter builds on the work of the previous chapter and describes the use of W3 defect waveguides as mode selective, continuous-wave (cw) laser mirrors. The high reflection and mode selectivity of the W3 mini-stopband (MSB) is used to produce single mode cw lasing in broad area mesa lasers (typically multi-mode). The main results described in this chapter were published in reference [82].

9.2 Design and Fabrication

The band structure of a W3 waveguide and the existence of a mini-stopband (MSB) was discussed in section 8.1. The MSB is formed by the anti-crossing of the fundamental and fourth order modes and, as a consequence, is a highly reflective spectral region for these two modes. The attenuation in transmission was shown to be at least 20 dB in section 8.4.1 giving an indication of the high reflection. The band structure of a W3 and transmission spectrum for a 360 nm period W3 waveguide are shown again in figure 9.1 for reference.

The W3 MSB can be used as a laser mirror by choosing the period so the spectral position of the MSB coincides with the gain peak of the laser material. The peak gain wavelength for the quantum-dot material was previously shown to be at 1280 nm (section 5.3.2). Figure 9.1 indicates the MSB lies at a normalised frequency of 0.27, calculated theoretically and from experimental result. Therefore a W3 with a period of $a = 1280 \times 0.27 = 345$ nm should have a MSB centred at 1280 nm.

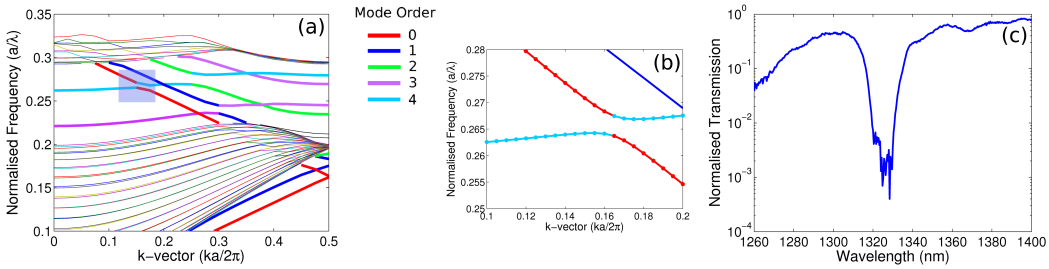

Fig. 9.1: (a) A typical band structure of a W3 with (b) the mini-stopband highlighted. (c) Transmission spectrum of a 360 nm period device.

A layout of the laser design utilising a W3 mirror is shown in figure 9.2. Previous work [64] indicates that 2 mm is a good laser length for the quantum-dot material. The taper is a smooth change in width ($\sim 1^o$) and will therefore vary in length depending upon the width of the main gain section. The W3 mirror is 100 periods in length. A small section of the taper and the W3 mirror are not pumped due to the difficulty of depositing electrical contacts on small features [9]. There is also an extra passive waveguide at the far end of the W3 (not shown in figure) to aid characterisation. The specific fabrication steps were described in detail in section 8.3.

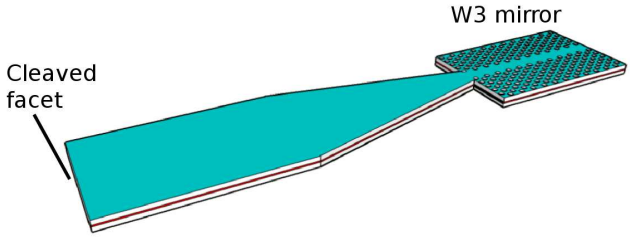

Fig. 9.2: Schematic of W3 mirror laser (not to scale). The gain section is 1.8 mm long and the taper is 200 μm long. The W3 mirror and 50 μm of the taper are not pumped. The other mirror is a cleaved facet.

9.3 Results

The measurement set-up used was very similar to that described in section 5.3.1. A Melles-Griot power meter was also used to obtain power-current (P-I) relationships.

9.3.1 5 μm Wide Gain Section Lasers

Initially a sample of laser devices with a 5 μm wide gain section and a range of periods (335–355 nm) were fabricated. Two devices, the 350 nm and 355 nm period W3 mirrors, produced particularly good laser results as displayed in figure 9.3. Figures (a) and (d) show the P–I curve for each device. Both have thresholds of the same order as similar devices fabricated in chapter 6 and both have reasonable slope efficiencies. They are both good lasers. Figures (b) and (e) show the OSA spectra of the output from the lasers. Lasing peaks are visible at 1260 nm and 1280 nm for the 350 nm and 355 nm devices respectively. Both of these peaks correspond to a normalised frequency of 0.277. Figures (c) and (f) show the top down IR camera image of each device lasing. The images are centered at the W3–gain section interface where a bright spot is visible. No light can be seen in the passive waveguide (at the other side of the W3) in either device.

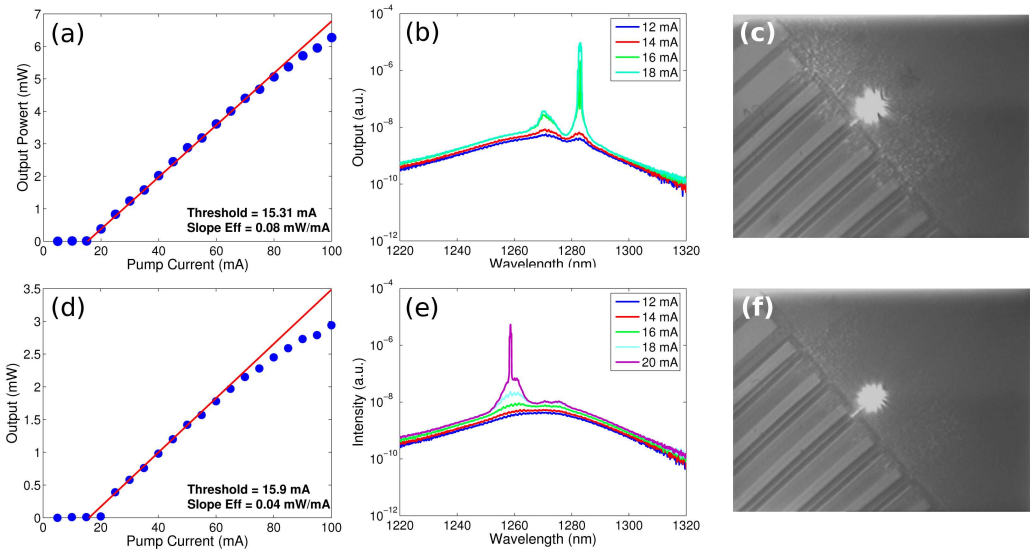

Fig. 9.3: (a) P–I curve of a laser device with a 355 nm period W3 mirror, (b) corresponding OSA spectra and (c) top-down IR camera image of W3–gain section interface above lasing threshold. (d)–(f) show the same for a 350 nm period W3 mirror.

Only one other device reached a lasing condition. This was the 335 nm period device and the results are shown in figure 9.4. The P–I curve shows a threshold 3 times higher than the 350 and 355 nm period devices and a slope

efficiency an order of magnitude lower than the 355 nm device. The OSA shows a lasing peak at 1280 nm (normalised frequency = 0.261). The camera image shows light transmitting through the W3, into the passive waveguide.

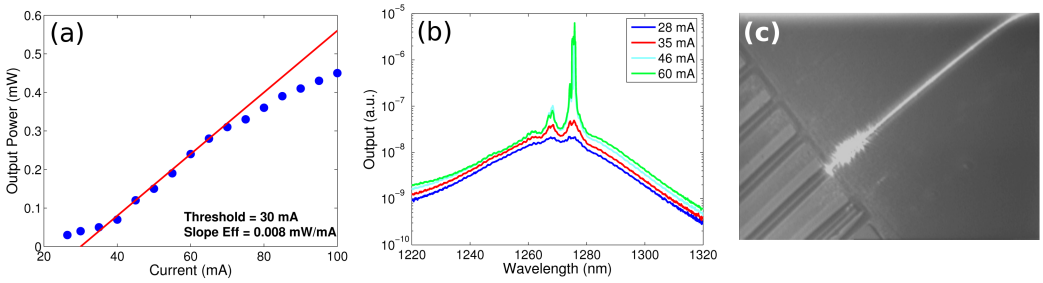

Fig. 9.4: (a) P–I curve of a laser device with a 335 nm period W3 mirror, (b) corresponding OSA spectra and (c) top-down IR camera image of W3–gain section interface above lasing threshold.

The results show that the 350 and 355 nm period devices are much better lasers than the 335 nm device. It is debatable if lasing is actually occurring in the 335 nm period device. All the P–I curves are plotted together in figure 9.5 to highlight this. The camera images would suggest that the 350 and 355 nm period W3 mirrors are operating at the MSB position and providing feedback for the laser. The operation of the 350 and 355 nm period devices at the same normalised frequency provides further evidence for this. Light is transmitting through the 335 nm period W3 mirror, despite the lower power, suggesting that the laser operation is away from the MSB. The feedback for lasing is probably provided by mode mismatch at the W3 interface or some damage to the waveguide.

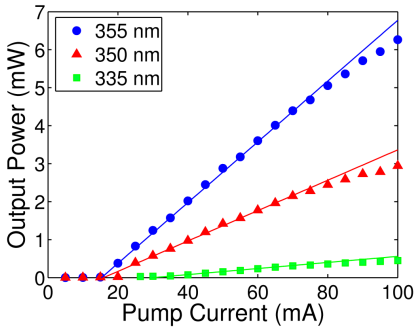

Fig. 9.5: P–I curve from figures 9.3(a),(d) and 9.4(a) plotted on same axis.

The results suggest that the 350 and 355 nm period devices are operating as designed. To confirm that the lasing action was due to the MSB and not some interface reflection, the back-end of the sample was cleaved and the output through the passive waveguides was measured on the OSA. Figure 9.6 shows the output spectra for the 350 and 355 nm devices and the corresponding camera images. The MSB is clearly visible in the spectra and the lasing peak forms in the centre of it. The camera images show that most of the reflection is still occurring at the W3, where there is a bright spot, with a dimmer spot at the output facet. There is little light seen in the passive waveguide.

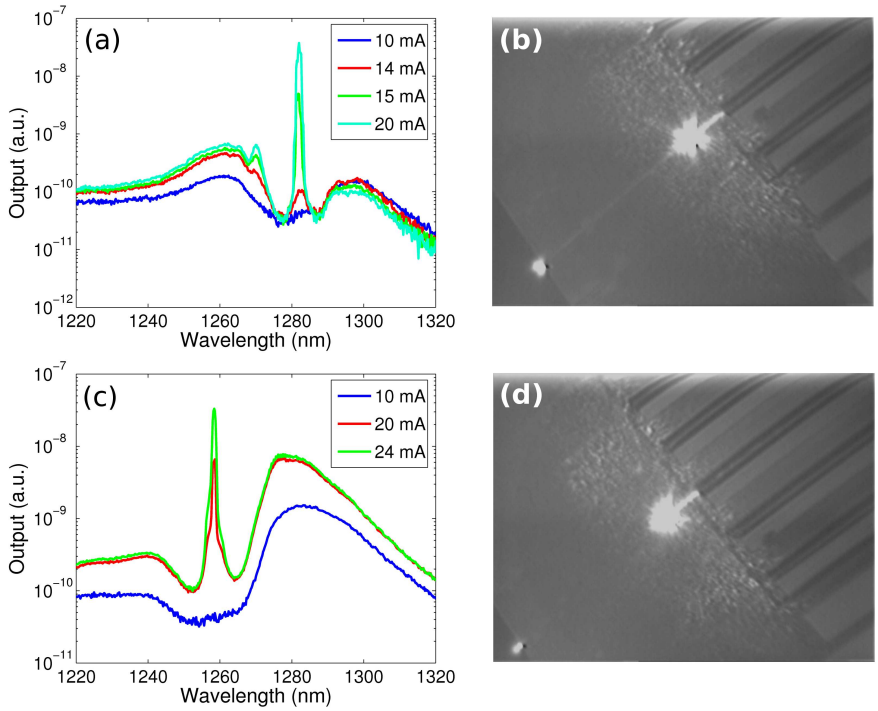

Fig. 9.6: (a) Spectral output of the 355 nm period W3 laser device transmitted through the W3 mirror and (b) associated IR camera image. The output facet can be seen in the bottom left hand corner. (c) and (d) display the same for the 350 nm period device.

Figure 9.7 shows the OSA output and corresponding camera image for the 340 nm period device. The spectra show the onset of lasing at about 40 mA at a wavelength of 1280 nm. The MSB is visible at a wavelength of 1230 nm, far away from the gain peak. The camera image shows that the lasing feedback is arising from the facet reflection, where there is a bright spot, and not the W3.

Large amounts of light can be seen in the passive waveguide.

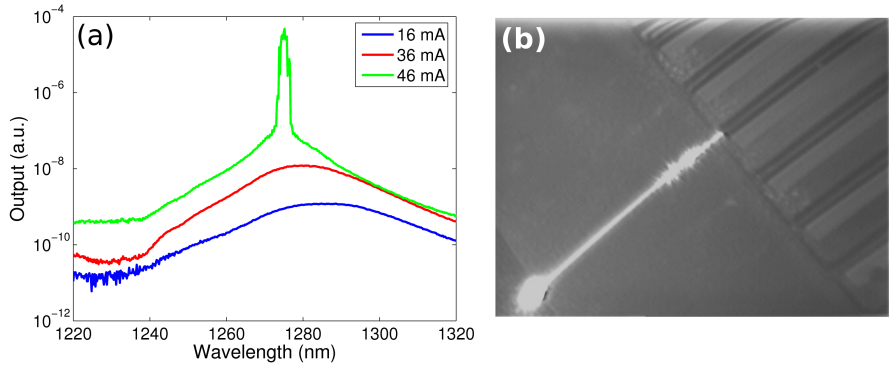

Fig. 9.7: (a) Spectral output of the 335 nm period W3 laser device transmitted through the W3 mirror and (b) associated IR camera image.

In summary, the 5 μm wide devices were conclusive in showing strong lasing feedback provided by the MSB. The two devices (350 and 355 nm period) that lased via feedback from the MSB had threshold currents and slope efficiencies comparable to those for similar devices characterised in chapter 6. In contrast, devices whose MSBs lay away from the quantum-dot gain peak barely lased at all. It was clear at this stage that the W3 waveguide far outperformed the finned waveguide and the decision to change mirror structure had been vindicated.

9.3.2 20 μm Wide Gain Section Lasers

A potential advantage of a W3 mirror is its transverse mode selectivity. The MSB only reflects the fundamental ($m = 0$) and fourth order ($m = 4$) modes. In a typical cleaved facet semiconductor mesa laser the first few modes ($m = 0...3$) are likely to lase depending on the mesa width. In general, the fourth order mode will not lase under normal excitation. The MSB will therefore act like a mode selective mirror and should produce single fundamental transverse mode output.

To investigate this mode selective property, devices with a 20 μm wide gain section were fabricated and characterised. 20 μm would be wide enough to observe multiple lobes in a multi-mode output. The devices were otherwise identical to the 5 μm wide devices with the same W3 period range.

The mode-profiles were measured using a beam profiler. The profile of a device reflecting from a W3 MSB is shown in Fig. 9.8. Also shown are the profiles for two as-cleaved facet devices. One device has a constant width of 20 μm and the other has a taper similar to the one used for the W3. The profiles show that the taper provides some mode filtering compared with the plain 20 μm device, but the extra lobes persist. The W3 mirror device is the only one that has a single lobe throughout the operating range, highlighting the mode selective feedback obtained from the MSB.

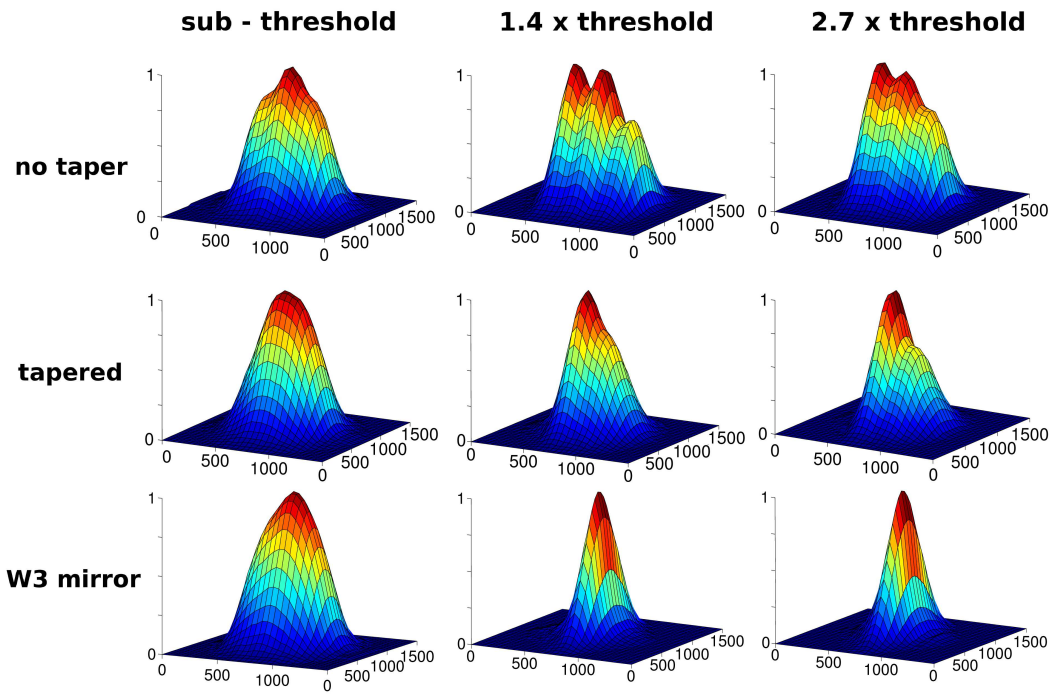

Fig. 9.8: Mode profiles of devices at sub-threshold, 1.4×threshold and 2.7×threshold for un-tapered 20 μm, tapered 20 μm and W3 mirrored 20 μm wide devices. The horizontal axes are displacement across the beam (μm). The threshold current density was very similar for all devices.

The W3 mirror device shown in figure 9.8 had its MSB at the quantum dot gain peak. The device had a threshold current and slope efficiency comparable to similar devices characterised in chapter 6. This is consistent with the 5μm devices measured previously.

Further evidence of the mode-selective nature of the W3 mirror was provided by a device whose W3 MSB lay away from the gain peak at a wavelength of

1305 nm. Figure 9.9 shows the output spectra and beam profiles over a range of pump currents for the device. The device has three distinct operating phases. The first and most obvious of these is the sub-threshold phase. The spectrum shows no lasing peak and the beam profile is a broad lobe like those seen in figure 9.8. The second phase begins at a pump current of approximately 200 mA. A lasing spike is seen at the quantum-dot gain peak wavelength (1280 nm) and the beam profile is multi-mode. Lasing feedback is probably provided by some mode-mismatch at the W3 interface. The final operating stage is observed at pump currents above 250 mA. A lasing spike is now seen at the MSB wavelength of 1305 nm and the 1280 nm peak has disappeared. The peak is almost two orders of magnitude larger than the peak at 1280 nm had been and the beam profile has become a single lobe. In this phase, the high pump current has provided enough gain for lasing at the MSB wavelength. The enhanced feedback at this wavelength induces a jump in lasing wavelength and the mode-selectivity of the W3 mirror leads to lasing in the fundamental mode only. This switch from multi-mode to single-mode lasing with higher pump current is the opposite of what is typically expected in semiconductor lasers.

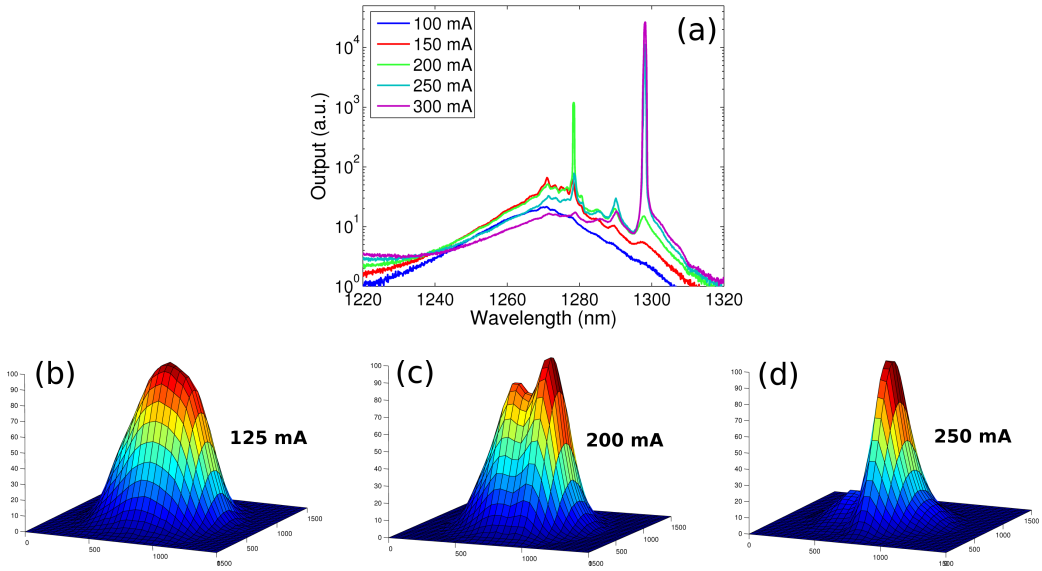

Fig. 9.9: Output spectra and beam profiles for a W3 laser device with a MSB at 1305 nm.

Figure 9.9 highlights the mode selectivity of the W3 mirror. It also shows the ability of the W3 mirror to produce lasing away from the quantum-dot peak gain wavelength, albeit with higher threshold currents. Lasing was also observed on the low side of the gain peak at a wavelength of 1255 nm. This wide operating range was not seen in the 5μm wide devices. This is because narrower devices have a higher threshold current density (chapter 6) and the ground state gain gets saturated before the threshold condition is met.

9.4 Design Improvement

The cw laser results were very promising overall and worthy of publication [64]. The results clearly indicate the mode selectivity of the W3 mirror, but considering the strong transmission dip seen in the passive measurement (figure 9.1(c)), one would also expect higher reflectivity than from a cleaved facet and correspondingly lower thresholds. These were not observed, however.

The reflection from a W3 MSB is more complex than being simply related to transmission ($R \neq 1 - T$) and involves modal conversion between the fundamental and fourth order modes of the W3 [79]. The theory describing this process, coupled mode theory, predicts that any incident fundamental mode, at the MSB wavelength in a W3, will reflect into the fourth order mode. The theory also predicts the reverse process.

Some simple FDTD simulations were used to study the back-reflection from the W3 waveguide into the access waveguide. A W3 length of 20 periods was used to increase simulation speed. Initially, simulations were performed for the structure design used experimentally. Figure 9.10 shows the design file and the corresponding transmission and reflection spectra. The spectra show the reflection into different order even modes of the access waveguide and were calculated for an incident fundamental mode (of the access waveguide).

The MSB is evident in the spectra at a normalised frequency of 0.265. Reflection is evenly distributed into the fundamental and fourth order modes with almost no light entering the second order mode. Coupled mode theory predicts that a reflected fundamental mode is the result of an incident fourth order mode and vice versa. This would suggest that the incident fundamental mode of the access waveguide excites various modes in the W3. At the MSB

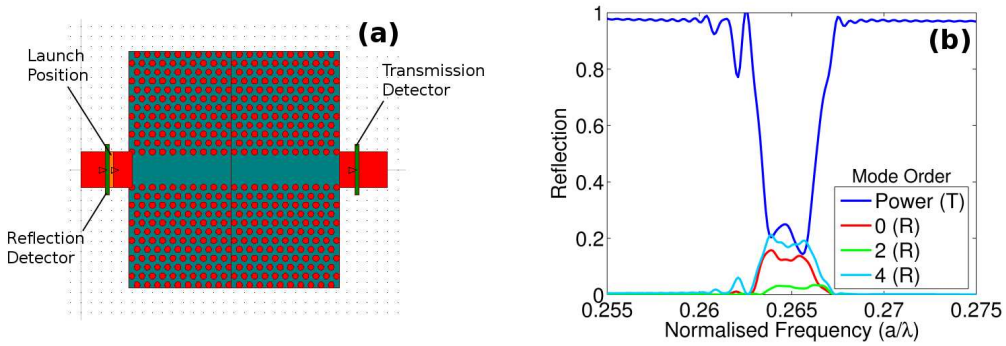

Fig. 9.10: (a) FDTD design file and (b) simulated transmission and reflection spectra for W3 design used experimentally. Reflection is shown for each even mode.

wavelength, all these modes are transmitted through the W3 with the exception of the fundamental and fourth order. These modes are reflected into their counterparts and back into the access waveguide. This is what is observed in the simulated reflection spectra.

The simulation predicts quite poor reflection, ∼15%, into each mode which suggests that most of the reflected light is being lost to scattering. The simulation was rerun at a fixed normalised frequency of 0.265 and the field profile is plotted in figure 9.11(a). Significant scattering can indeed be seen outside the access waveguide.

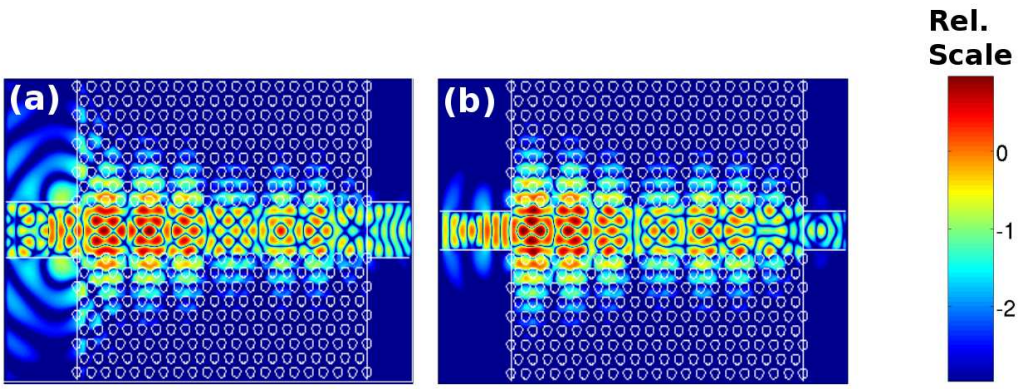

Fig. 9.11: Steady state field profile for (a) original W3 laser mirror design and (b) optimised laser design

The access waveguide–W3 interface is the most likely source of scattering. In order to address this, the width of the access guide was scanned in an attempt to improve the interface coupling. The simulated results are shown in figure 9.12 and show the peak fundamental reflection as a function of access guide width. The x-axis units are normalised to the width of a W3 (width $w = 2\sqrt{3}a$). For a normalised access guide width of w=1 (experimental value (highlighted)), the access guide terminates in the centre of the boundary holes of the W3 waveguide. As the access waveguide is narrowed, the reflection first falls to a minimum at $w \sim 0.9 \times W3$. At this value, the edges of the access waveguide are in line with the edge of the first row of holes of the W3. This suggests that scattering is the main mechanism preventing coupling of reflected light back into the access waveguide. However, by narrowing the access waveguide further, the reflectivity into the fundamental mode of the access waveguide increases again and peaks at a width of $w \sim 0.7 \times W3$. The field profile at this access guide width (figure 9.11(b)) shows efficient coupling and little scattering.

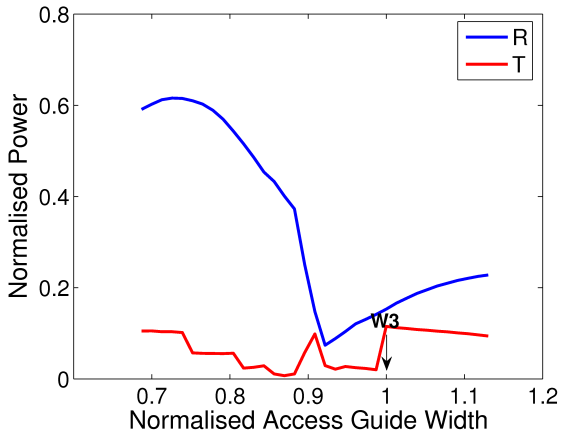

Fig. 9.12: Simulated W3 peak fundamental mode reflection and corresponding transmission as a function of access guide width.

The simulations predict that reflectivity into the fundamental mode can be increased by up to a factor of 4 over the present value by reducing the access waveguide width. This should lead to a significant improvement in laser performance.

A sample of W3 lasers utilising both the old design and the new optimised

design, with the narrower access guide was fabricated and characterised. The resulting P–I curves are shown in figure 9.13. The results utilising the new design indicated no improvement. The reasons for this are unclear, but one possibility is that the narrower access guide exhibits a higher optical loss and this balances out any gain in reflection.

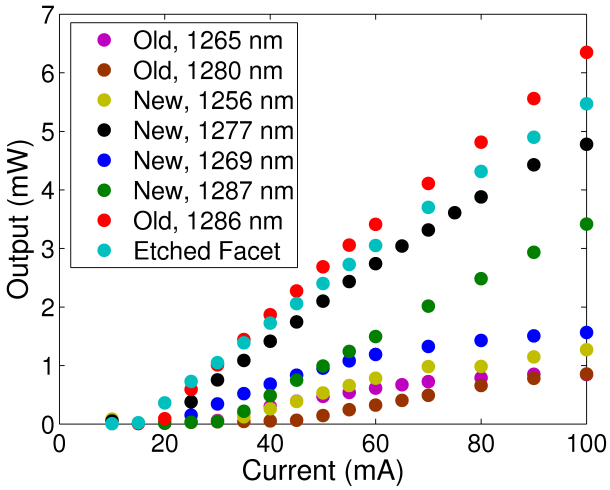

Fig. 9.13: P–I curves for W3 lasers utilising original (old) and optimised (new) W3 mirror design. The legend shows the design type and corresponding operating wavelength for each device. The P–I relationship for a device with an etched facet mirror is shown for reference.

9.5 Summary

In summary, cw W3 mirror lasers have been fabricated and characterised. The W3 MSB provides feedback for only the fundamental mode leading to single transverse mode output, even for wide gain sections. The thresholds are similar to lasers with two cleaved facets. FDTD simulations suggested optimisation of the reflection coupling from the W3 mirror into the gain section would lead to a factor 4 increase in reflectivity. However experimental results showed no improvement when using the optimised design. The results for cw lasing are impressive. The next chapter begins with a study of the potential of the W3 as a dispersion compensating mirror.

10. Γ–M DEFECT WAVEGUIDES AND THE POTENTIAL OF A DISPERSION COMPENSATING MIRROR

10.1 Introduction

The bulk of this chapter concentrates on another photonic crystal defect waveguide for use as a laser mirror. This waveguide is also of W3-type, but propagation is in the Γ-M direction instead of the Γ-K direction as previously. The chapter begins by studying the potential of a Γ-K waveguide for use as a dispersion compensating mirror. The realisation that the reflection peak has too broad a spectrum for a dispersion compensating mirror is the motivation for the study of the new Γ–M defect. Several iterations of simulation and experiment lead to the fabrication of a high reflecting laser mirror and a solid understanding of the interesting physics involved. The chapter finishes by exploring the potential of the Γ–M defect as a dispersion compensating mirror and presents some initial experimental results.

10.2 A Pulse Compressing Chirped W3 Mirror?

Before attempting to fabricate any experimental devices with dispersion compensating mirrors, finite difference time domain (FDTD) simulations were performed to model the W3 Γ-K mirror's response to an optical pulse.

The spectral tuning of the W3 mini-stopband (MSB) with defect width was first analysed with the FDTD software. The result is shown in figure 10.1 along with the experimental results from section 8.4.3 and the MPB simulation from section 8.2.2. The three plots are for a period of 360 nm and all have very similar tuning rates, $d\lambda/dW \sim 0.8$, indicating accuracy in the simulations. Inspection of equation 1.3, with a tuning rate of 0.8, gives a value of 6 for

the number of mirror sections, N_{steps}, the e-beam lithography machine can define at maximum resolution. This should hopefully give a sufficiently good approximation to a smooth chirp.

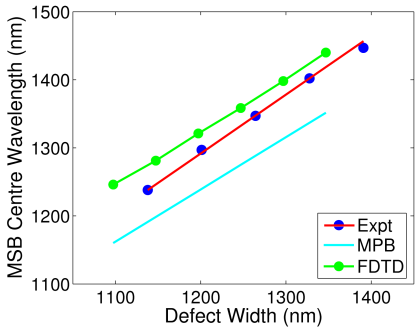

Fig. 10.1: Comparison of theoretical and experimental results for spectral tuning of mini-stopband centre wavelength with defect width. The MPB plot was extrapolated over a broader range than figure 8.5. The tuning rate, $d\lambda/dW$ is consistent.

The next step was to design a chirped mirror with the parameters calculated in section 1.2.3. An FDTD simulation was performed on such a mirror with an incident 3 ps linearly chirped pulse with a 5 nm bandwidth. The centre wavelength of the pulse was chosen to be the centre wavelength of the MSB of the first section of the mirror. This assumption was made due to the fact that the lasers in chapter 9 operated at the centre wavelength of the MSB. The simulation results are shown in figure 10.2(b). There is no compression evident in the reflected pulse. The reason for this can be understood by studying figure 10.2(a) which shows the spectral response of the W3. The reflection of the MSB is relatively flat topped and its spectral width is much broader than that of the pulse. The mirror chirp has no effect on the pulse as the pulse wavelength is at the centre of the MSB. Therefore, a much narrower reflection peak is necessary to create a dispersion compensating mirror.

10.3 Γ–M Orientation

Previous photonic crystal laser work [9, 10] used a defect waveguide in the Γ–M crystal direction to create a DFB type laser. It operated on a MSB formed when the fundamental mode folds at the Brillouin zone boundary (the

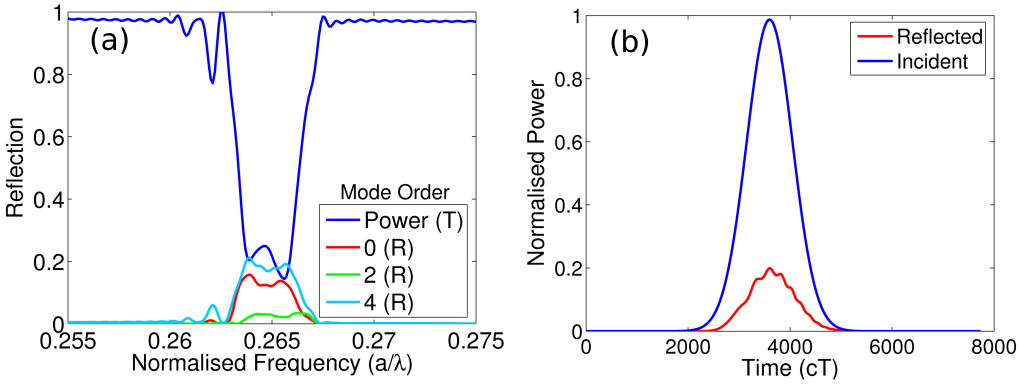

Fig. 10.2: Simulated pulse reflection from a chirped W3 mirror. (a) is a repeat of figure 9.10(b) and shows the spectral reflection of a W3 mirror. (b) shows the mirror response at a normalised frequency of 0.265. No compression is observed.

M Point). This MSB should be significantly narrower than the W3 Γ–K MSB studied in the previous chapters. The next few sections describe the simulation and experimental characterisation of these Γ–M mirrors.

10.3.1 Γ–M Band Structure

The frequency domain MIT photonic bands (MPB) package was used to calculate the band-structure of a W3/4 defect orientated in the Γ–M direction[1]. Figure 10.3 shows the calculated band structure along with the W3 band-structure repeated from figure 8.3 for comparison. The wider Γ–M defect allows the presence of higher order modes and results in a more complex band structure. The folding of the fundamental mode at the Brillouin zone boundary can be seen at a normalised frequency of ~ 0.27 and results in a mini-stopband. Figure 10.4 shows an expanded view of this MSB.

[1] I refer to a W3/4 defect as it is formed by the alternate removal of three and four holes.

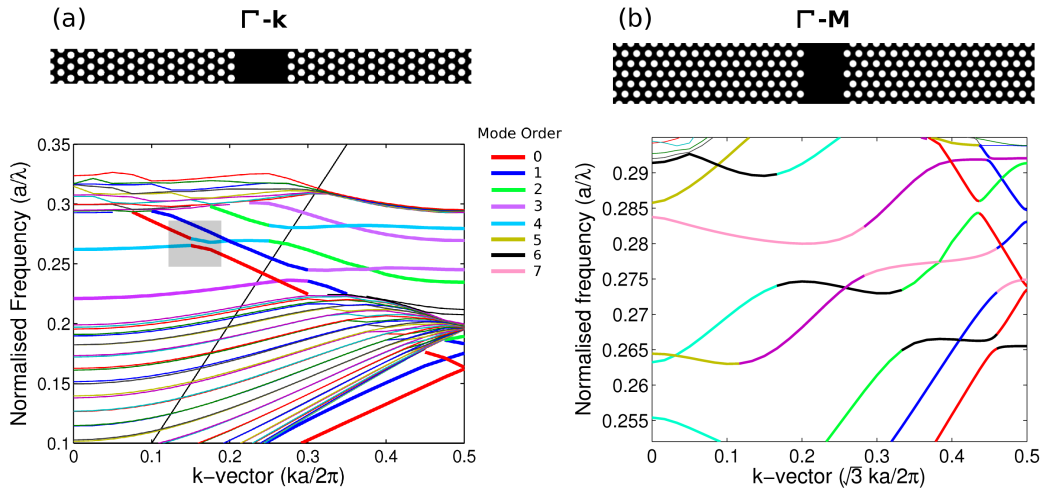

Fig. 10.3: Band structures of different oriented photonic crystal defects. (a) is a repeat of figure 8.3(a) and shows the supercell and band structure of a Γ–k orientated W3 defect. (b) shows the supercell and band structure for a Γ–M orientated W3/4 defect.

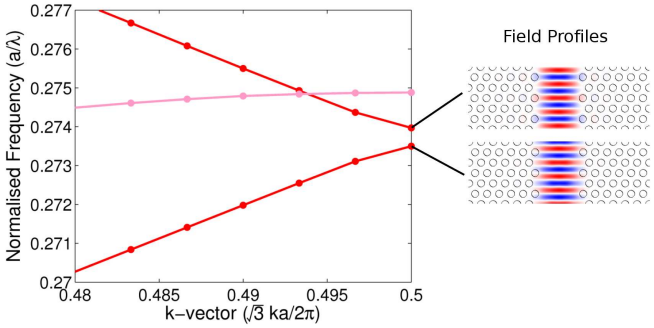

Fig. 10.4: Expanded view of interception of fundamental mode with Brillouin zone boundary in figure 10.3(b). The field profiles either side of the mini-gap are also shown.

10.3.2 FDTD Simulations

FDTD simulations were performed on the Γ–M defect waveguide to study its reflection properties. Figure 10.5 shows the fundamental mode spectral transmission and reflection within the band-gap. Initially it was assumed that the narrow peak at a normalised frequency of ∼0.265 was due to the fundamental mode fold at the Brillouin zone boundary[2]. An expanded view of this peak is

[2] This was actually an incorrect assumption as shall be explained in the next few sections.

shown in figure 10.6 along with the W3 MSB spectral reflection for comparison. The Γ–M reflection peak is significantly narrower than that of the W3 and therefore a better candidate for use as a dispersion compensating mirror.

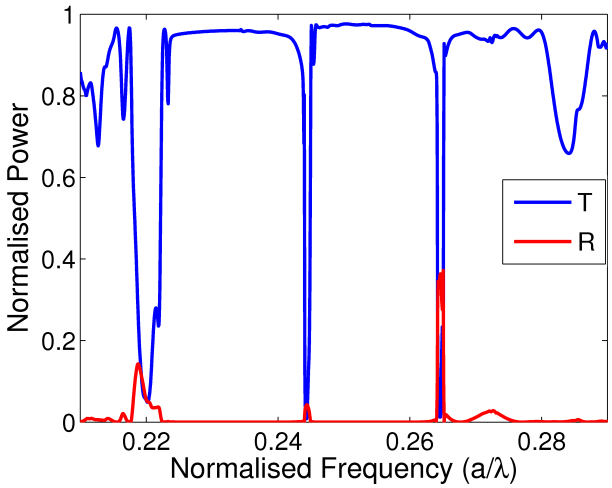

Fig. 10.5: Fundamental mode transmission and reflection for a Γ–M orientated W3/4 defect.

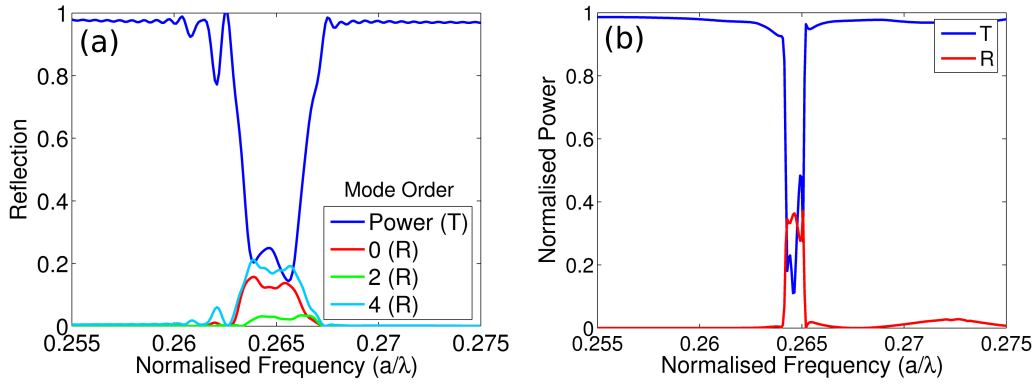

Fig. 10.6: (a) is a repeat of figure 9.10(b) and shows the spectral reflection of a W3 mirror. (b) shows the fundamental mode transmission and reflection for a Γ–M orientated W3/4 defect over the same frequency range.

The spectral tuning of the reflection peak with defect width was then studied using further FDTD simulations. This was necessary to see if $d\lambda/dW$ was sufficiently low enough to allow the fabrication of a mirror that would give a good

approximation to a smooth chirp as explained in section 1.2.3 (equation 1.3). The simulated results are shown in figure 10.7 and show an interesting trend: the reflection becomes significantly stronger when we reduce the defect width. This was an unexpected and interesting result that warranted experimental investigation.

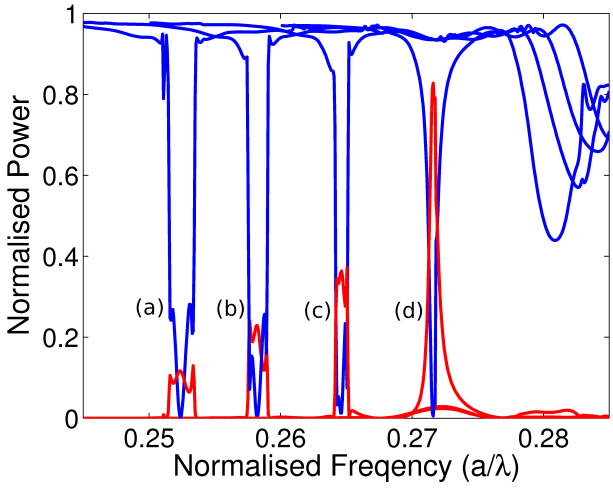

Fig. 10.7: Variation of fundamental transmission and reflection with defect width for Γ–M orientated defect. (a), (b), (c) and (d) correspond to widths of 1.08, 1.04, 1.00 and 0.96 times a W3/4 width respectively.

10.3.3 Γ–M Initial Experimental Results

The high reflectivity of the MSB of the reduced width Γ–M defect seen in figure 10.7 was considered to be an ideal cw laser mirror. The high reflectivity could be confirmed experimentally by a low threshold or high slope efficiency in a cw laser.

Passive Transmission

Initially a set of passive devices were fabricated. These consisted of Γ–M defect waveguides with a width of 0.96 times that of a W3/4 with a range of periods. The measured transmission spectra are shown in figure 10.8 along with the FDTD simulated spectra for the same structure. The experimental

transmission dip at a normalised frequency of ∼0.28 had a full width half maximum (FWHM) of only 7 nm. This narrow dip was assumed to be the narrow high reflecting MSB in the simulated spectrum (at a normalised frequency of ∼0.27) with a small error in frequency[3].

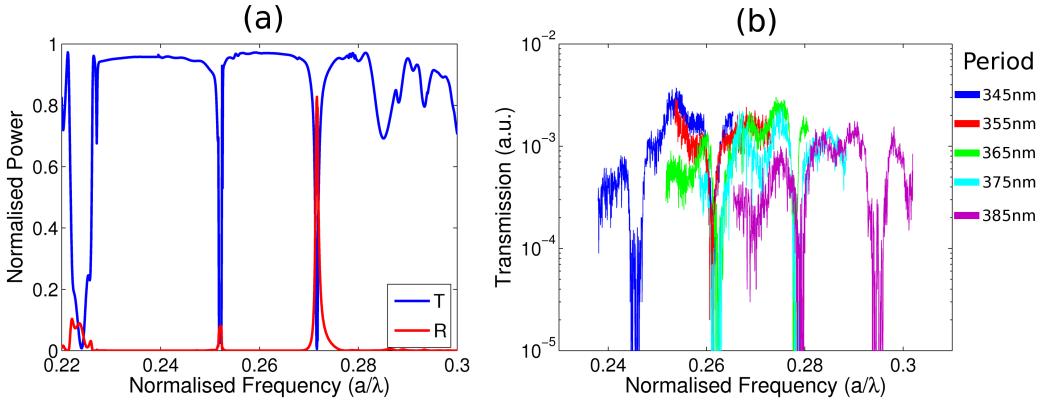

Fig. 10.8: Transmission spectra of a Γ–M defect waveguide. The waveguide has a defect width of 0.96 times that of a standard W3/4 waveguide. (a) is the simulated FDTD transmission spectrum and (b) is an experimental measurement.

Laser Devices

Several attempts were made to fabricate cw lasers with the high reflecting Γ-M defect mirror. The results were disappointing with high threshold currents and low slope efficiencies. Furthermore, lasing never occurred from the centre of the MSB. This was evident when the back end of the laser device was cleaved to study transmission through the crystal. Such a spectrum is shown in figure 10.9 where the lasing appears to occur anywhere but inside the MSB. Further devices with different defect widths and periods yielded similarly poor results. Furthermore, the spectra appeared inconsistent and difficult to match to simulations. One possible problem was a variation in hole radius (due to variation in electron beam exposure dose) from sample to sample. To investigate this, the variation of hole radius on reflectivity was studied.

[3] This assumption proved to be incorrect due to inaccuracies in the simulation (see figure 10.14) and a resulting mis-identification of MSB.

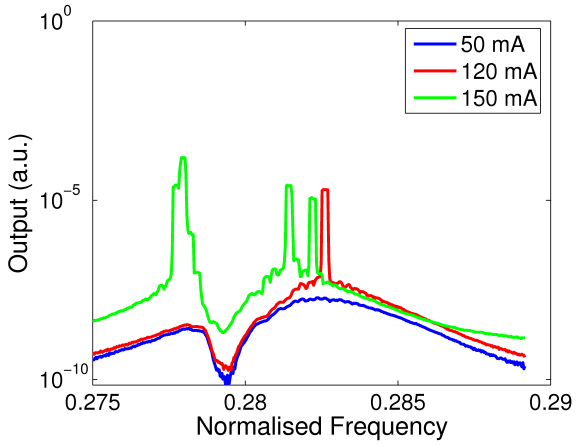

Fig. 10.9: An example of a Γ–M laser device that did not lase inside the MSB.

10.3.4 Further Simulation

FDTD simulations were performed to study the variation of hole radius on MSB reflectivity. Figure 10.10 shows the reflectivity as a function of hole radius and defect width. The figure clearly shows that the MSB can be high reflecting for any defect width by suitable choice of hole radius. With this knowledge experimental work could be continued.

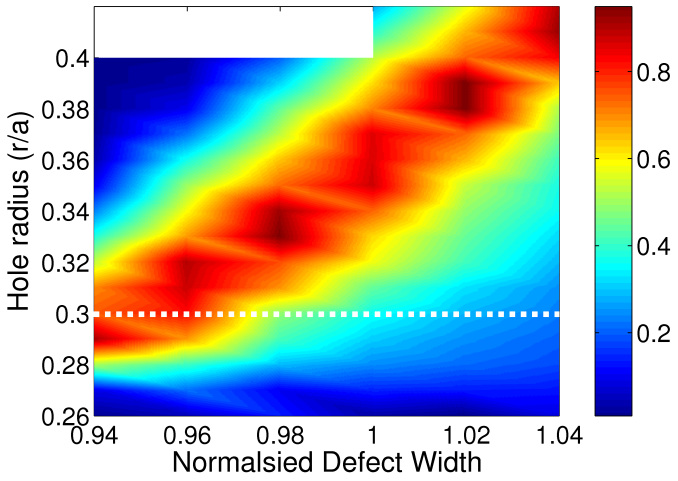

Fig. 10.10: Simulated MSB reflectivity as a function of defect width and hole radius for a Γ–M defect waveguide. The plot contains around 50 points and the shading has been interpolated, a valid approximation for such an obvious trend. The horizontal line highlights the simulation results from figure 10.7.

10.3.5 Further Experiment

Variation in the electron beam exposure dose, and therefore hole radii, was the biggest source of error in the photonic crystal fabrication. The change in hole size shifts the spectrum of any photonic crystal device. To allow for this, a range of periods was always made to ensure that the MSB of one device overlapped with the quantum-dot gain peak.

Figure 10.10 shows that for a given defect width the MSB can be scanned through the reflectivity peak by varying the hole radius. It is therefore possible to work with a fixed period and defect width and vary the hole radius. This helps repeatability: the period and defect width are independent of electron beam exposure dose and consistent from sample to sample.

The next experiment was to fabricate another set of passive devices, this time with fixed period and defect width and a range of hole radii. This would allow me to know exactly where the MSB would lie for a given period, radius and defect width and make future experimental work much simpler. Figure 10.11 shows the resulting transmission spectrum. One immediately notices a significant result: while the wide transmission dip around a normalised frequency of 0.265 tunes as expected with radius ($d\lambda/dr = 2.3$), the dip at a normalised frequency of ∼0.278 tunes much slower ($d\lambda/dr = 0.4$). The significance of this result is the subject of the next section.

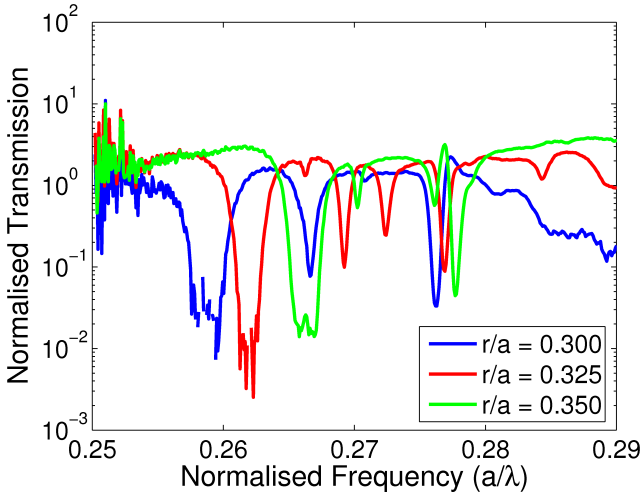

Fig. 10.11: Passive transmission of a Γ–M defect waveguide with a range of different hole radii.

10.3.6 Revision of Band Identity and the Origin of the High Reflection Peak

After some consideration, I realised that the slowly tuning transmission dip in figure 10.11 was probably the MSB arising from the fundamental fold at the MSB. The reason for this can be understood by examination of the field profiles in figure 10.4. The field penetrates very little into the crystal and as a result a change in the crystal parameters will have very little effect on this mode.

A consequence of this was the realisation that the MSB studied in the FDTD simulations was not this folding fundamental band but that of the anti-crossing of the fundamental and sixth order modes (seen at a lower normalised frequency in figure 10.3). The fact that the spectral position of this simulated MSB tuned significantly with hole radius confirmed this. This tuning was observed during the simulations used to obtain figure 10.10 and is plotted for a W3/4 defect in figure 10.12(a). Re-examination of the same simulation data also revealed that the spectral position of the peak reflection was always at a normalised frequency of 0.273 as shown in figure 10.12(b).

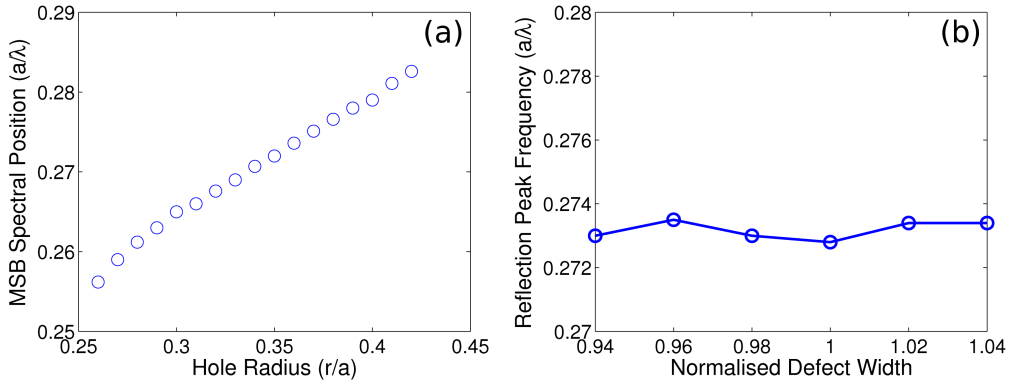

Fig. 10.12: Further data extracted from FDTD simulations displayed in figure 10.10. (a) shows the spectral tuning of the MSB with hole radius for a W3/4 defect and (b) shows the spectral position of the peak reflectivity for each defect width.

At this point I realised the origin of the high reflection peak seen in the FDTD simulations. As mentioned above, the spectral position of the peak reflection was always around the same normalised frequency of 0.273 and the MSB in the

simulations was the one resulting from the anti-crossing of the fundamental and sixth order modes. The spectral position of the fundamental fold in figure 10.3 is also at a normalised frequency close to 0.273. I hypothesised that the peak reflection in the FDTD simulations was observed when the spectral position of the fundamental–sixth MSB overlapped with that of the fundamental–fold MSB. To show this, further band structures were calculated using MPB with different hole radii. Figure 10.13 displays the calculated band structures. The figure shows that as the hole radius is increased, the fundamental–sixth MSB moves to higher normalised frequency and coincides with the fundamental–fold MSB at a radius of $0.36a$. This agrees well with the FDTD simulations in figure 10.10 which also show peak reflection at $r/a = 0.36$ for a W3/4 defect.

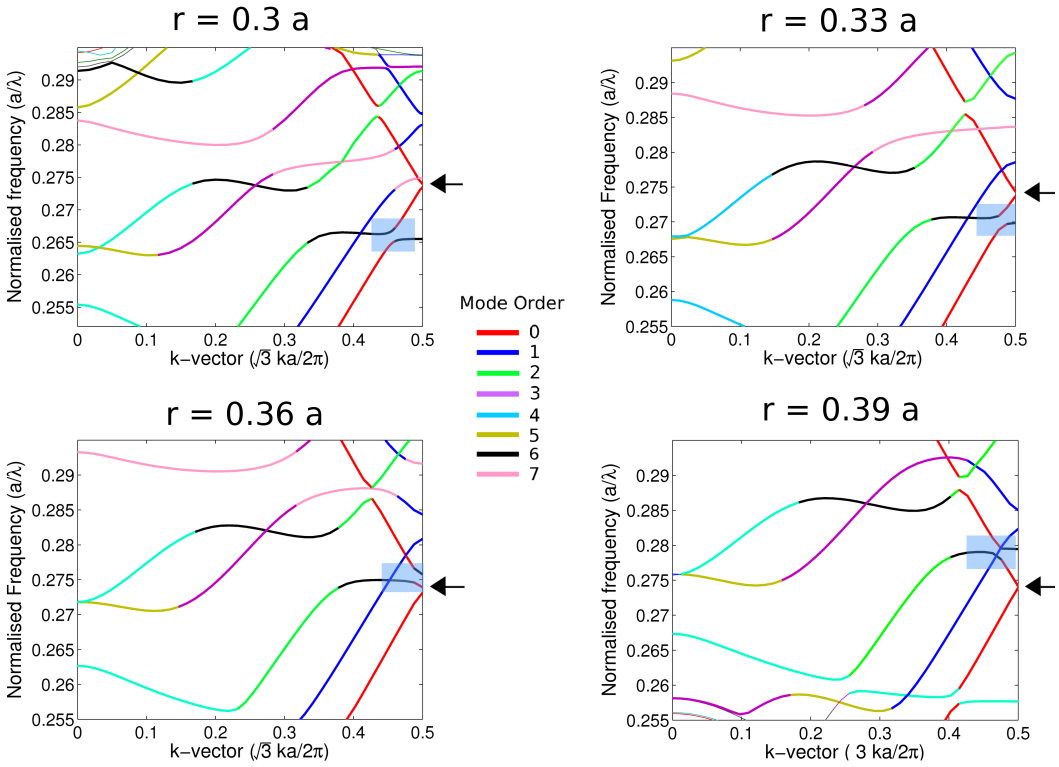

Fig. 10.13: Calculated band structures for a Γ–M W3/4 defect for a range of hole radii. The fundamental–fold MSB is highlighted with an arrow and the fundamenatal–sixth order MSB is highlighted as a shaded box.

One advantage of all of this is that the spectral position of the fundamental–fold MSB does not vary much with hole radius or defect width. This was con-

firmed by re-examination of experimental data which always showed a transmission dip around a normalised frequency of 0.278, such as in figures 10.9 and 10.11. This means devices can be designed with a fixed period of $1280 \times 0.278 = 356$ nm to match the MSB to the gain peak.

There is one unanswered question that arises from these conclusions: Why does the fundamental–fold MSB not appear on the FDTD simulations? There were two possible causes. Firstly if the fundamental–fold MSB is particularly narrow then the resolution of the simulations might be too low to fully resolve the peaks. This was unlikely as the resolution was quite high, as evidenced by the high detail in figure 10.5. The other possibility is that it is a weak interaction and that the crystal was not long enough. To check this, the simulation used for figure 10.5 was repeated with the photonic crystal length doubled to 60 periods. The resulting spectrum is shown in figure 10.14 together with a repeat of figure 10.5. A transmission dip and reflection peak are clearly seen at a normalised frequency of ∼0.273 in the longer crystal spectrum. The simulations would therefore suggest that the fundamntal–fold MSB is therefore a relatively weak interaction. However, as described above, by combining the MSB with the fundamental—sixth MSB we can enhance the reflectivity. The next step was to attempt to show this experimentally.

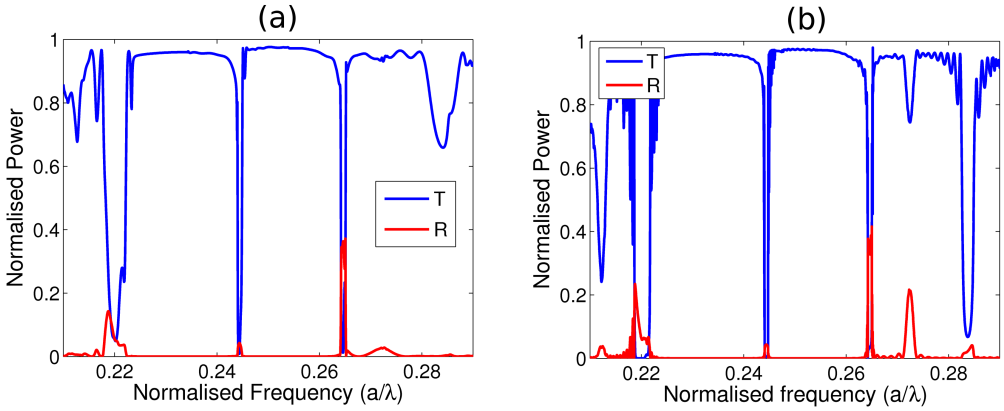

Fig. 10.14: Fundamental mode transmission and reflection for a Γ–M orientated W3/4 defect for a crystal length of (a) 30 periods and (b) 60 periods.

10.3.7 Further Experimental Work

A sample of laser devices with a fixed period of 355 nm and hole radii ranging from 0.27 to 0.43 in a W3/4 defect were fabricated and characterised. The blue plot in figure 10.15(a) shows the theoretical reflection as a function of hole radius for a W3/4 defect. This plot is just an extraction from figure 10.10. The laser with hole radii of $0.37a$ operated with the lowest threshold and highest slope efficiency suggesting the photonic crystal was behaving as expected. The red plot in figure 10.15(a) shows the measured slope efficiency for each laser. Figure 10.15(b) shows the IR camera image of the $r = 0.37a$ device during lasing operation. A bright spot is seen at the photonic crystal, with very little light penetrating through the crystal.

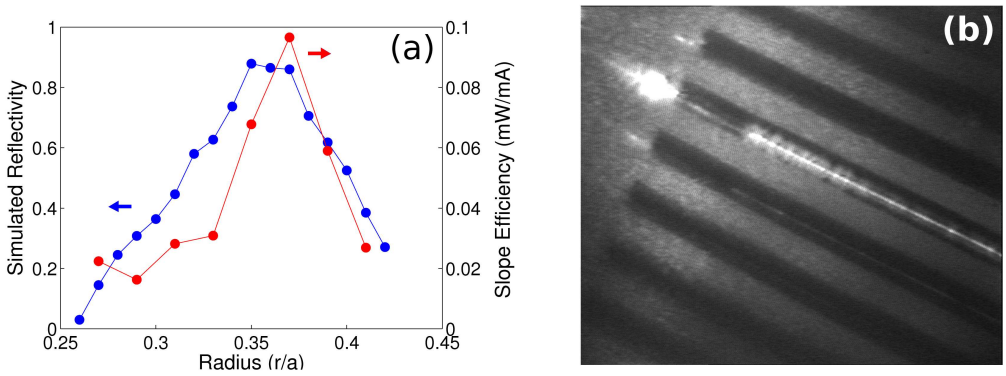

Fig. 10.15: (a) Simulated reflection for a Γ–M W3/4 defect and corresponding slope efficiency for cw lasers for a range of hole radii and (b) IR camera image of the $r - 0.37a$ device above threshold.

To confirm lasing was due to the fundamental–fold MSB, the back end of the device was cleaved and transmission through the crystal was examined. A transmission dip was observed around 1285 nm for every device. The MSB tuned slowly to higher frequencies with increasing hole radius as expected ($d\lambda/dr = 0.45$). The six devices surrounding the peak in figure 10.15(a) all lased at the centre of the MSB, however the others did not. Figure 10.16 highlights this.

For reference a device that was identical to the others but had an etched facet instead of a photonic crystal mirror, had a threshold of 46.7 mA and a slope efficiency of 0.033 mW/mA. By comparison the device with hole radius

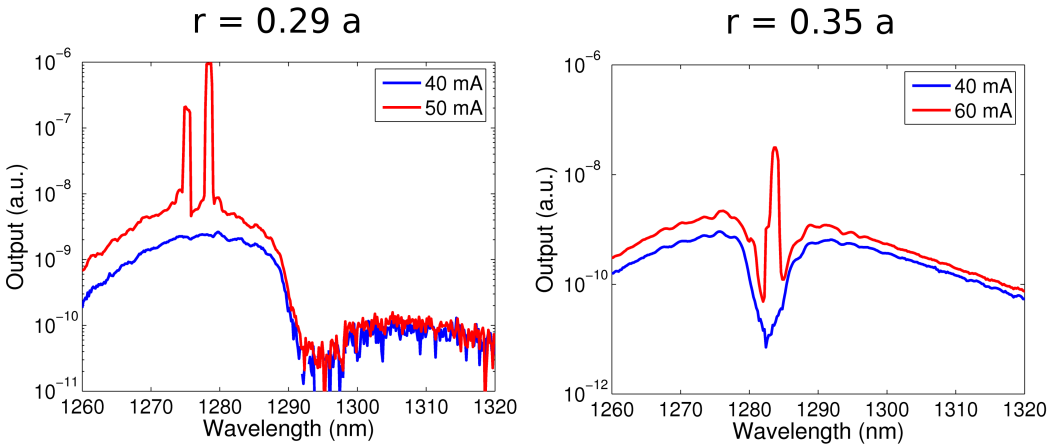

Fig. 10.16: Spectral transmission through photonic crystal mirror of Γ–M defect lasers with hole radii of (a) $0.29a$ and (b) $0.35a$.

$0.37a$ had a threshold of 34.9 mA and a slope efficiency of 0.1 mW/mA. The main improvement is seen in the slope efficiency due to the long laser length; the threshold of long lasers is typically dominated by the optical loss and not the mirror reflectivity. Close inspection of figure 10.15 reveals only three lasers outperformed the etched facet indicating that reflectivity is only enhanced for hole radii within the range $0.33a < r < 0.41a$.

10.3.8 Γ–M Summary

The switch to the Γ–M orientated defect was motivated by the need for a narrower MSB for a dispersion compensating mirror. The above work demonstrates that the Γ–M defect does indeed provide a narrower MSB (see figure 10.17) that has sufficient reflectivity for use as a laser mirror. Furthermore, we can tailor the strength of this reflectivity by adjustment of the hole radius. With this new photonic crystal mirror, the potential of fabricating a dispersion compensating mirror was re-explored.

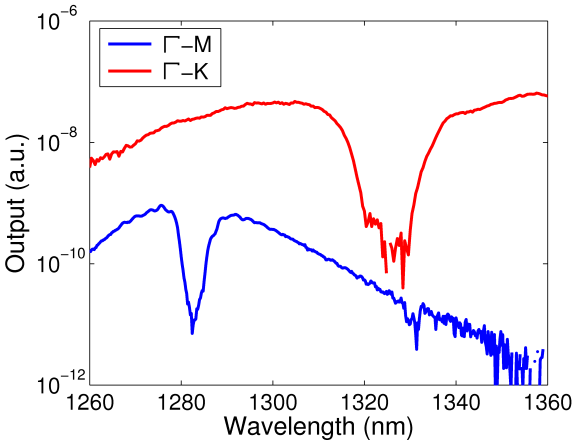

Fig. 10.17: Comparison of Γ–M W3/4 MSB and Γ–K W3 MSB.

10.4 A Pulse Compressing Chirped Γ–M Mirror?

10.4.1 FDTD Simulations

FDTD simulations were performed upon the fundamental–sixth MSB when I still believed it was the fundamental–fold MSB. However, given that both MSBs have a similar width experimentally and that the reflectivity of the fundamental–fold MSB can be tailored by adjusting the hole radii, I believe the results are worth presenting.

A few different chirped Γ–M mirror designs were simulated. The best result was obtained with eight sections each with a defect width 1 nm wider than the previous and the first section being a W3/4. The incident and reflected pulse are shown in figure 10.18(a). The incident pulse has a duration of 3 ps and a bandwidth of 5 nm while the reflected pulse has a duration of only 800 fs. The figure clearly shows that the peak pulse level in the reflected pulse is over twice that of the incident pulse, despite the mirror reflectivity being only 0.4. This is a clear indication of pulse compression. Figure 10.18(b) shows the spectral profile of the incident and reflected pulse. The distortion of the reflected pulse is a consequence of the imperfect chirp and highlights the technology imposed limit of sectioning the mirror. However, most of the spectral bandwidth is maintained.

Although the simulation was calculated upon the wrong MSB, it is an im-

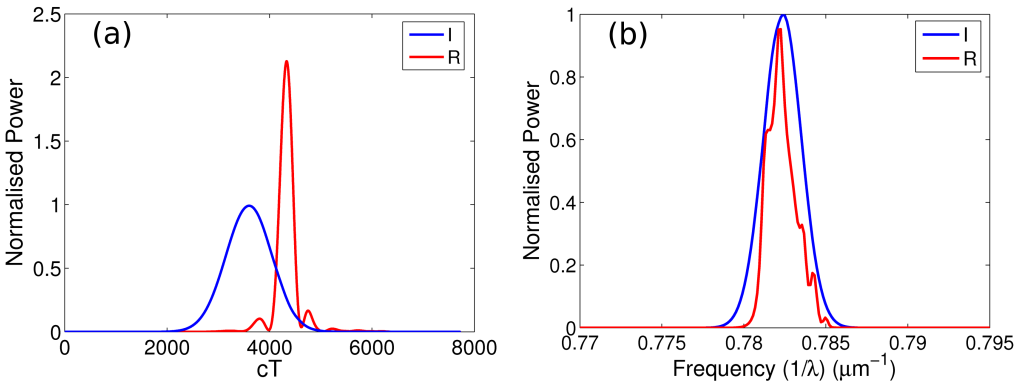

Fig. 10.18: Simulated pulse reflection from a chirped Γ–M defect mirror.

portant proof of principle. Pulse compression is possible with a spectrally narrow (∼10 nm) reflection peak with a maximum value of 0.4. With a similar chirp, pulse compression should be possible with the fundamental–fold MSB. A sample of devices with a range of hole radii would ensure that at least one device has the correct peak reflectivity for pulse compression.

10.4.2 Initial Experimental Results

Cleaved Facet Mode-Locked Lasers

Before attempting any mode-locked photonic crystal lasers, I first fabricated a set of simple, deeply etched, cleaved facet lasers. Deeply etched quantum-dot mesa lasers have previously been successfully mode-locked with pulse durations of 7 ps [16].

Fabricating passive mode-locked lasers requires a few extra process steps. Firstly, the contact stripes are defined with a 50 μm split to form to separate contacts. After evaporation and lift-off this gap is then etched approximately 100 nm through the highly doped cap layer. This provides electrical isolation between the two contact pads with a resistance of a few kΩs. The devices are then cleaved to create an absorber length of a few hundred microns and a gain section of about 2 mm.

The first set of devices fabricated were 5 μm wide mesas. A drawback of such narrow mesas is that they cannot be driven at high operating currents. At high current densities, the carriers form in the first excited state [83]. The

5 μm devices did mode-lock but the mode-locking was very unstable.

A device consisting of a narrow 4 μm wide absorber section and then a flared waveguide gain section was used as alternative. This allows operation at high pump currents and the flared waveguide provides more gain and thus higher output power. This design was first proposed by Thomson et al [26] on shallow etched ridge lasers. The narrow absorber section is single mode for shallow etched lasers and therefore acts as a transverse mode filter. However, in mesa lasers, a 4 μm waveguide is multi-modal and therefore the absorber section will not act as a mode filter. In chapter 9, I demonstrated the single mode nature of a photonic crystal waveguide fundamental MSB. Therefore, the mode filtering in my lasers can be provided by the photonic crystal mirror.

Figure 10.19 shows the optical spectrum of a mode-locked flared mesa laser under cw and pulsed operation. In cw mode, with no reverse bias, a few longitudinal modes dominate the spectrum and contain most of the optical power. In mode-locked operation, with a reverse bias voltage, the power is distributed across many longitudinal modes with a gaussian profile. This is a clear sign of mode-locked operation as is the reduction in operating power. To fully confirm mode-locked operation, the laser output was analysed with a RF spectrum analyser which showed a strong peak at 19 GHz which corresponds to the repetition rate of the laser.

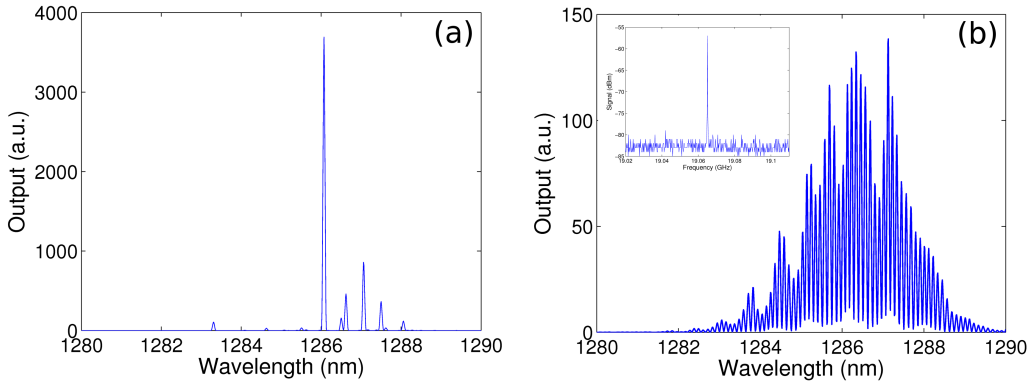

Fig. 10.19: Optical spectrum of a flared two-section laser operating under (a) cw condition at 300 mA and (b) mode-locked condition at 270 mA and a reverse bias of 2.7 V.

The flared design was found to be much more stable than the initial narrow

design. A higher output power was also obtained. The stability was further enhanced when I fabricated a thermally controlled stage. This allowed me to keep the lasers at a constant operating temperature of 25 ^{o}C.

Γ–*M Mode-Locked Lasers*

Only one set of devices were tested before the submission of this report. The devices contained a flared gain section, 1.7 mm long, and a narrow absorber section, 300 μm long. The photonic crystal mirror was placed behind the absorber section. Unfortunately their design was based on the FDTD simulation above and therefore at the wrong spectral position. However mode-locking was achieved in all the devices indicating that there is no fundamental problem with mode-locking a laser with a photonic crystal mirror. Figure 10.20 shows the mode-locked spectra of a Γ–M defect laser and of a laser with an etched facet instead of a photonic crystal mirror. The bandwidth of both devices is very narrow (1 nm) indicating long pulse durations. The spectrum of the photonic crystal laser is much cleaner than that of the etched facet although this was possibly due to the etched facet laser operating with a higher reverse bias voltage.

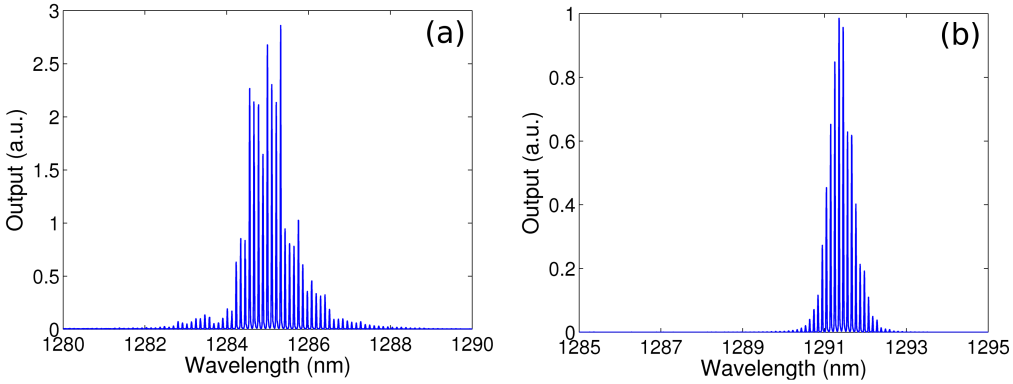

Fig. 10.20: Optical spectrum of mode-locked lasers with (a) an etched facet mirror operating at 100 mA with a reverse bias of 4 V and (b) a photonic crystal Γ–M W3/4 defect mirror operating at 138 mA and a reverse bias of 1 V.

Although there is no sign of pulse compression (no change in spectral bandwidth), the mode-locking of a laser with a photonic crystal mirror is an important step. This result together with the above simulation results indicate

that pulse compression with a Γ–M defect mirror should be possible in future.

10.5 Summary

This chapter has explored the properties of a Γ–M photonic crystal defect. Several iteration steps of simulation and experiment led to an improved understanding of the physics involved. A variation in hole radius was shown to result in a variation of MSB reflectivity. This reflectivity reaches a peak value for an overlapping of two MSBs. This was shown experimentally by a dramatic improvement in laser efficiency. The potential of fabricating a dispersion compensating mirror for mode-locked lasers was also explored. Initial results were promising and mode-locking was achieved with a photonic crystal mirror. No pulse compression was observed, but a redesign of the mirror chirp with the enhanced knowledge of Γ–M defects, will hopefully lead to pulse compression in a passively mode-locked quantum-dot laser in the future.

11. SILICON BASED DBR ORGANIC LASER

11.1 Introduction

This chapter moves away form quantum-dot lasers and reports the fabrication and characterisation of a silicon based visible laser. The laser design consists of an active light emitting polymer combined with a distributed bragg reflector (DBR) resonator (a one dimensional photonic crystal). The work was done in collaboration with Andreas Vasdekis and was published in reference [84]. Andreas was responsible for the polymer processing and measurements. The design and fabrication of the resonator and the experimental results of the hybrid device are discussed as part of this thesis.

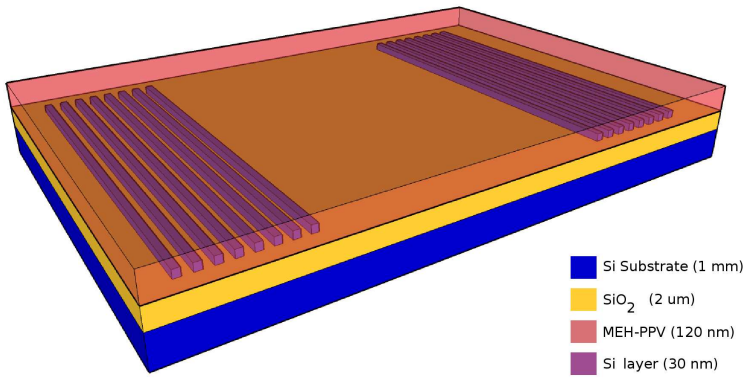

Fig. 11.1: Schematic of the hybrid silicon-organic DBR laser design

A DBR laser typically consists of an active medium placed between two Bragg mirrors. In our design the active medium is the polymer and the Bragg mirrors are two silicon–air gratings. The silicon mirrors are formed on a silicon on insulator (SOI) wafer. A SOI wafer consists of a thin (a few hundred

nanometres) crystalline silicon layer on top of a silica buffer layer and a silicon substrate. The mirrors are formed by etching a Bragg mirror into the top silicon layer. The remainder of the silicon layer is removed. The light emitting polymer, with an emission peak centred at 625 nm, is deposited onto the resonator. A schematic of the design is shown in figure 11.1. The design is not an obvious choice for a silicon emitter, due to the high absorption of silicon at the emission wavelength. However the silicon has a high Fresnel reflectivity and the polymer exhibits high gain. The challenge was to see if these advantages would overcome the high absorption.

Silicon has a poor emission efficiency due to its indirect band-gap and the development of active silicon photonic devices has been hindered as a consequence. Current approaches include optically excited Raman lasers [85, 86], nanopatterned silicon lasers [87], the use of rare earth dopants [88] and the hybrid bonding of III-V semiconductor lasers to silicon chips [89]. The hybrid device discussed in this chapter provides an alternative approach that would integrate well with current silicon processing technology. The deposition of the solution-processable polymer can be performed by the addition of a simple fabrication step. There is also potential for chip-to-chip communication as the emission wavelength of the polymer lies within the absorption band of a silicon photodetector.

11.2 Fabrication

Photonic crystal rods (dielectric rods in air) had been considered as a potential periodic structure for laser mirrors. An initial feasibility study in SOI yielded no results, but an excellent SOI fabrication process was developed. Figure 11.2 shows a SEM image of such a photonic crystal and highlights the good processing conditions. This process suited the fabrication of the SOI resonator perfectly. The individual steps of the process are described below.

11.2.1 Design

The Bragg mirrors were designed to have a lattice constant of 360 nm, a fill factor of 30 % and a top silicon layer thickness of 30 nm. At the polymer emission wavelength of 630 nm, the stop-band of such a mirror originates from

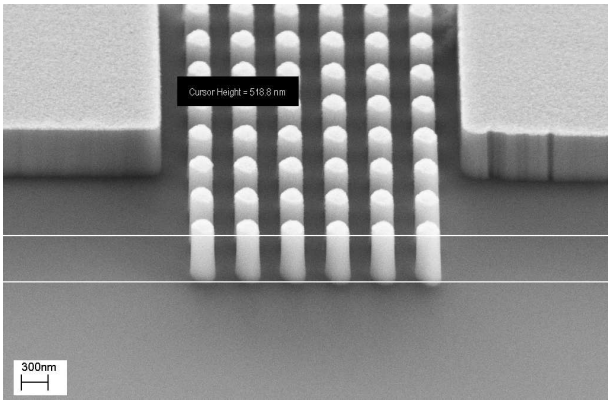

Fig. 11.2: SEM image of SOI photonic crystal rods. The rods are etched to a depth of 725 nm. The image highlights the good fabrication process that was applied to the SOI resonator.

second order diffraction and provides feedback while the first order diffraction provides coupling of the laser mode to free space radiation [90].

11.2.2 Wafer Preparation

The SOI substrates available had a 220 nm thick undoped top silicon layer on top of a 2 μm thick silicon dioxide layer on a silicon substrate. A thinner top layer was desired to minimise absorption of the visible laser radiation. Reactive ion etching (RIE) was used with a gas mixture of CHF_3 and SF_6 at a ratio of 1:1. The etch rate was calculated by etching several samples for a range of times and measuring the remaining silicon layer thickness using ellipsometry. The results shown in figure 11.3 gave an etch rate of $\sim$2.5 nm/s. When the layer thickness reduces below a value of $\sim$50 nm the etch rate decreases due to surface effects.

11.2.3 Pattern Definition and Masking

The Bragg mirrors were defined in polymethylmethacrylate (PMMA) resist using electron-beam lithography. After development, 30 nm of nickel (Ni) was laid down using electron-beam evaporation. A lift-off step (section 4.5.2) was then performed to leave a Nickel mirror mask. The Nickel mask was then exposed to an Oxygen plasma to form a harder Nickel Oxide (NiO_X) mask.

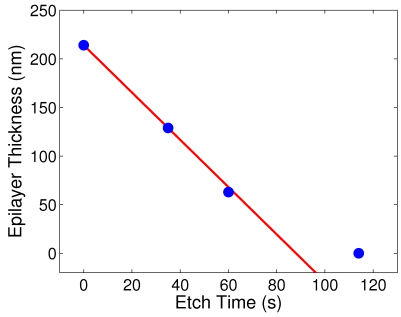

Fig. 11.3: Graph showing etch rate of top silicon layer using RIE

A range of other metal masks and metal/hardmask combinations were tested as etch masks. The NiO_X mask technique was discovered when using a Ni/photo-resist combination. The pattern was transferred to the photo-resist hard mask with an oxygen plasma (RIE) and then transferred into the top silicon layer (RIE, see next section). The Ni mask remained after the silicon etching. This suggested that the oxygen plasma had oxidised the Ni making it much more resistant to silicon etching. The photo-resist hard mask was therefore unnecessary and 30 nm of NiO_X was found to be an excellent mask for silicon etching.

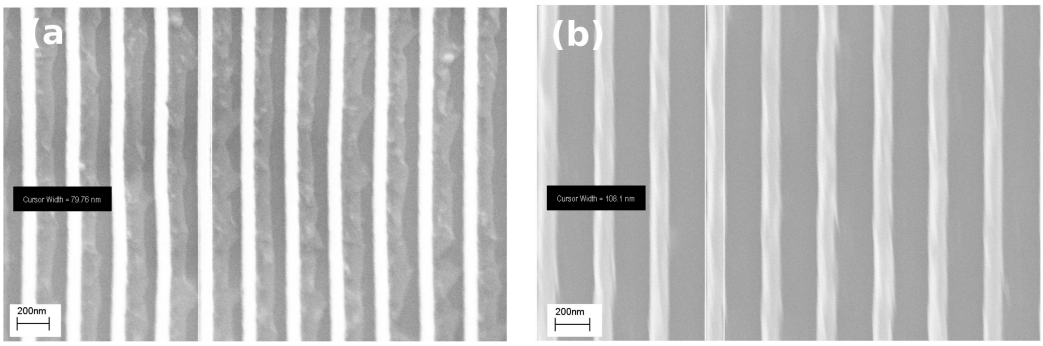

Fig. 11.4: SEM images of Nickel masks created from (a) SPL line design and (b) Polygon design.

Two e-beam lithography design techniques were available for defining the Bragg mirrors. The first of these is to write an array of single pixel lines (SPLs). This is the best method to obtain very narrow lines from the e-beam lithography machine. The disadvantage with SPLs is that they cannot be corrected for the proximity effect. The alternate method is to draw the Bragg

mirrors as an array of rectangular polygons. The resulting NiO_X masks from both techniques are shown in figure 11.4. The figure shows that the SPL technique can produce very narrow lines (∼70 nm), but with rough edges. The area technique still produces narrow lines (∼100 nm) but with much smoother edges. This smoother edge combined with their ability to be proximity corrected made the area technique the most appropriate for defining the Bragg mirrors.

11.2.4 Silicon Etching

Once the NiO_X mask had been defined, the pattern could be transferred to the top silicon layer. This was achieved using RIE with a gas mixture of CHF_3 and SF_6 at a ratio of 1:1. A SEM image of a cross-section and angled profile of an etched Bragg mirror is shown in figure 11.5. After the etch, the remaining NiO_X was removed by a 120 s dip in hydrochloric acid.

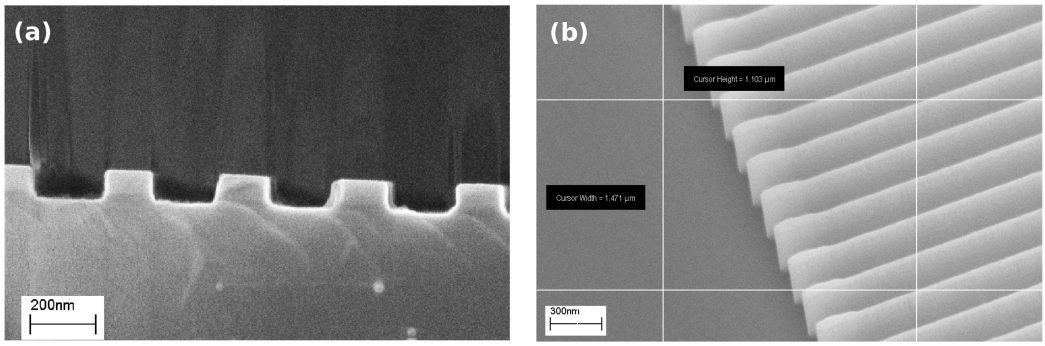

Fig. 11.5: SEM images of silicon etching of Bragg mirrors. Images are of (a) a cross-section and (b) an angled perspective.

11.2.5 Active Polymer Deposition

A 120 nm film of the prototypical conjugated polymer poly[2-methoxy-5-(2'-ethylhexyloxy)-p-phenylene vinylene] (MEH-PPV) was spun on top of the SOI resonator. This is a common light emitting polymer used in polymer lasers. Further details on this process step can be found in reference [84].

11.3 Results

Andreas Vasdekis was responsible for the measurements and further details can be found in his thesis. The hybrid laser structures were characterised by optical excitation. The pump laser produced 1.2 ns pulses at a wavelength of 532 nm and was focused between the Bragg mirrors. The emission from the polymer laser was collected from the surface using a fiber-coupled charge-coupled device (CCD) spectrometer. To avoid photo-oxidation of the polymer films, the structures were kept under vacuum during operation.

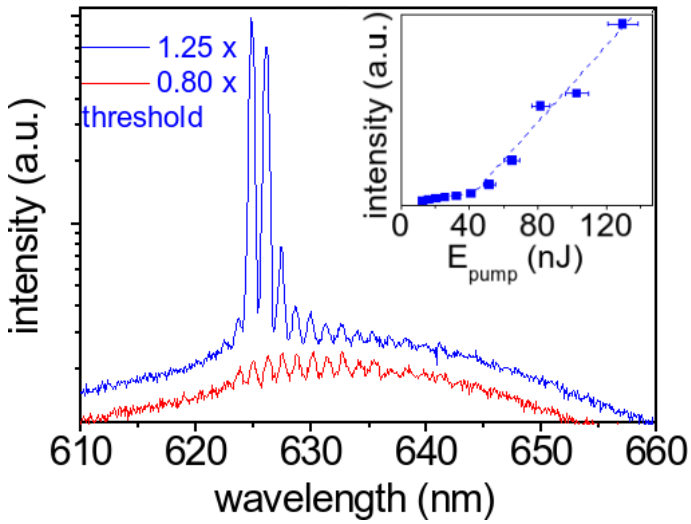

Fig. 11.6: Emission spectra for 50 μm cavity above and below threshold. Inset: Input/output relationship.

The emission spectra for a resonator with a 50 μm mirror separation is shown in figure 11.6. Below threshold, the spontaneous emission from the polymer couples to longitudinal modes of the cavity whose frequencies lie within the stop band of the Bragg mirrors. These longitudinal modes are evident in the figure as a series of narrow peaks. The frequency spacing of these mode peaks, the free spectral range (FSR) can be calculated by:

$$FSR = \Delta F = \frac{c}{2nL} \tag{11.1}$$

or in wavelength terms:

$$\Delta\lambda = \frac{\lambda^2}{2nL} \tag{11.2}$$

where λ is the operating wavelength (625 nm), n is the group index and L is the cavity length (50 μm). A value for the group index can be obtained by studying a range of cavity lengths. Figure 11.7 shows the spectra for three different cavity lengths along with the relationship between optical cavity length, nL, and cavity length, L. The optical cavity length was calculated from equation 11.2 using the longitudinal mode spacing. The gradient of figure 11.7(b) is equal to the group index, n, and is 3.15. The y-intercept of the plot is non-zero, indicating penetration of the cavity mode into the DBR mirror. The actual penetration depth is this y-intercept divided by the effective mirror index. The y-intercept is 2.5 μm and the effective refractive index of the mirror is $\sim$3.15[1], giving a penetration depth of 397 nm at each mirror. The figure also shows that increasing the mirror separation leads to an increase in the number of resonant modes and therefore a broader lasing spectrum.

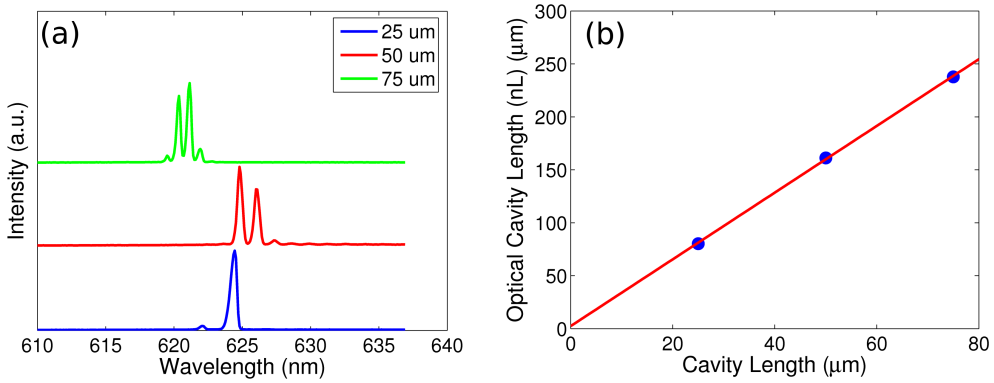

Fig. 11.7: (a) Emission spectra of hybrid resonator devices for three different resonator lengths and (b): relationshiip between optical cavity length and mirror separation.

In figure 11.6, the onset of lasing is seen in the lower wavelength modes, as the excitation energy is increased, with a threshold of about 45 nJ (inset of figure). This threshold is an order of magnitude higher than similar devices fabricated on fused silica substrates [84]. Andreas calculated the reflectivities

[1] Here I have neglected the small contribution from the silicon (refractive index of 3.88 (λ=625 nm)) and used the group index of 3.15 extracted from figure 11.7(b).

of the silicon and silica mirrors to be 0.17 and 0.26 respectively [84]. The difference could be a consequence of the higher absorption loss in silicon. A rough estimate of this mirror absorption factor, L_m can be calculated via:

$$L_m = e^{-2FF\Gamma_z \alpha_i L_p} = 0.965 \tag{11.3}$$

where α_i is the silicon absorption at the lasing wavelength, taken to be 5×10^3 cm^{-1} [91], L_p is the mirror penetration depth, calculated above (370 nm), FF is the silicon fill factor in the mirror (0.3) and Γ_z is the modal overlap with the silicon in the vertical direction, assumed to be 0.3[2]. Equation 11.3 highlights that the absorption loss in the mirror is very low. L_m should be equal to the ratio of the two mirror reflectivities[3] which is 0.65. The discrepancy indicates that there is an additional loss mechanism that reduces the silicon mirror reflectivity. Scattering loss is the most likely cause for the discrepancy. It should be noted that whatever this loss is, it is the dominant loss mechanism; the absorption loss is low. This is encouraging for future development as scattering losses can be reduced with a better mirror design and improved fabrication process.

Not all of the longitudinal modes reach threshold and this is attributed to the different scattering that each mode experiences.

The tunability of the hybrid device was also studied. Changing the lattice constant from 360 nm to 330 nm resulted in a blue shift of almost 20 nm in the lasing spectrum.

11.3.1 Summary

In summary a hybrid light emitting polymer SOI-DBR laser has been developed. The fabrication of the SOI-DBR resonator has been described in detail including silicon thinning, mirror mask material, pattern definition and silicon etching. A 50 μm cavity device lased at the polymer emission wavelength of 625 nm with a threshold of 45 nJ. The relatively high threshold was not due to silicon absorption in the Bragg mirrors as was initially hypothesised. It was a result of some unknown, dominant loss mechanism, probably scattering which

[2] This is a rough approximation calculated from the ratio of silicon thickness (30 nm) to polymer thickness (100 nm).

[3] The absorption of silica at 625 nm is negligible.

can be reduced by appropriate design. Therefore, future devices may exhibit thresholds comparable to or better than silica resonator devices. The design is a novel approach to obtain active devices on a silicon platform.

It is debatable whether the hybrid silicon laser device discussed here will be the solution to the emitter problem in silicon photonics. However, the work in this chapter has attracted some wider media interest [92, 93]. This highlights the huge interest in the subject and the importance of obtaining silicon emitters.

12. CONCLUSION

This thesis has reported a range of research related to photonic crystal laser mirrors. The research has involved both one- and two-dimensional photonic crystals with the majority of study on quantum-dot material.

A variety of fabrication processes and techniques have been developed and optimised. These have resulted in high quality photonic crystals (figure 12.1) and high performance laser diodes. I have also gained a better understanding of the underlying physics of the fabrication steps and an appreciation of the necessity of patience and care that is required for good micro-fabrication.

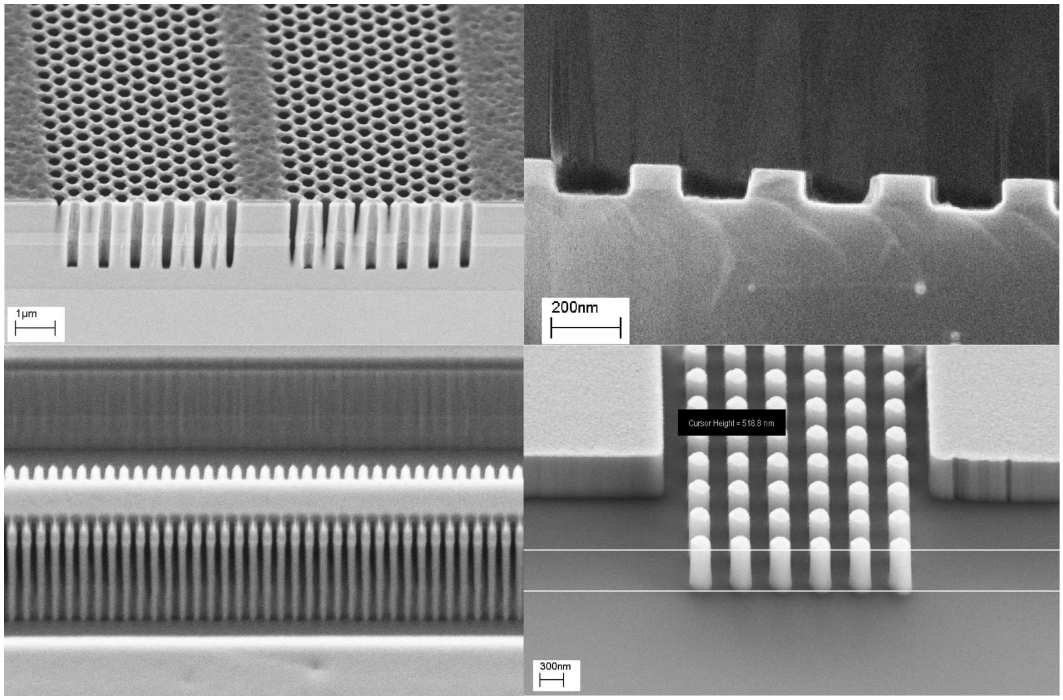

Fig. 12.1: SEM images highlighting the high quality photonic crystal fabrication achieved during this thesis.

The first significant result from this thesis was the experimental demon-

stration of low surface recombination and diffusion in quantum-dot material (chapter 6). A theoretical model was developed to extract exact values for the surface recombination velocity and carrier diffusion length. The surface recombination velocity was found to be 5×10^4 cms^{-1}, a similar value to InP. This result implied that GaAs based quantum-dot material could be used in fine structured photonic crystal lasers without high threshold penalties. Most active photonic crystal research had previously been constrained to an InP platform.

A range of photonic crystal laser mirrors were studied. The first structure studied was a one-dimensional finned waveguide that was anticipated to behave as a simple one-dimensional Bragg grating. Laser devices were operated cw, but exhibited very high threshold currents. Fabrication was very sensitive and this made repeatability difficult.

The main photonic crystal laser mirror studied was a two dimensional W3 defect waveguide. Initially a defect in the Γ–K crystal plane was investigated. Single fundamental mode mesa lasers were developed. The mode filtering capacity of the W3 mirror was demonstrated in multi-mode wide area mesa lasers (figure 12.2(b)) allowing the fabrication of wide area, high power single mode lasers.

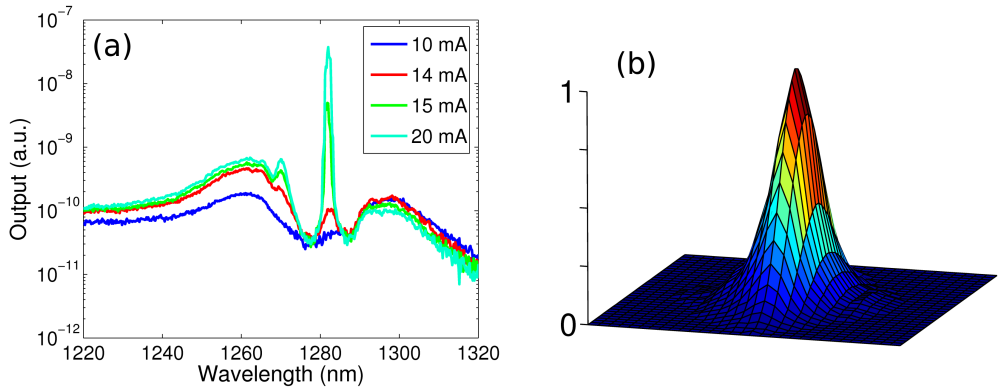

Fig. 12.2: Review of W3 laser mirrors. (a) shows a laser operating from the centre of the mini-stopband and (b) shows the mode profile of a 20 μm wide mesa laser with a W3 mirror.

The potential of the W3 Γ-K defect as a dispersion compensating mirror was explored. Simulations showed that the spectrum of the mini-stopband (MSB)

was too broad. The narrower MSB of the Γ-M orientated mirror was explored instead. It was discovered that the reflectivity of the Γ-M defect could be varied by changing the hole radius. This was a result of the spectral shift of one MSB through another. Simulations indicated that the narrow reflection peak from the Γ-M MSB could be used for pulse compression by suitable chirp of the defect width. An initial experimental attempt to realise this was unsuccessful, but a new design method has been proposed.

The final photonic crystal mirror studied was a one dimensional distributed bragg reflector on a silicon platform. The active medium was a conjugated polymer and the silicon resonator provided feedback. The study was a novel demonstration of a silicon emitter in the visible spectrum.

Future Work

Two research areas stand out as opportunities for future study. The first is the high reflecting Γ-M waveguides. Much of the previous work on photonic crystal lasers has focused on tiny laser cavities as emitters for photonic circuits. Most devices rely on a strongly reflecting bulk crystal end mirror. The only devices offering mode filtering require a DFB type defect waveguide that is difficult to pump electrically.

I propose that the Γ-M defect can provide both the high reflectivity and mode filtering together. This can then be combined with a flared gain section to maximise power output. This flare will be much easier to pump electrically than a photonic crystal defect waveguide.

The other research area with future potential is the development of a dispersion compensating chirped Γ-M mirror. As described at the end of chapter 10 the design of a dispersion compensating mirror is possible. By designing the correct chirp and fabricating a set of devices with a range of hole radii, the correct condition for pulse compression should be obtainable.

In summary the functionality that photonic crystal mirrors can bring to existing semiconductor laser designs has been explored. Successful integration of photonic crystal mirrors with semiconductor lasers has been achieved with some interesting results and indication of future potential.

APPENDIX

A. SLAB WAVEGUIDE ANALYSIS

Here we analyse the slab waveguide and study the nature of the guided modes. The analysis is based on that of Yariv [33]. We pick up the analysis where we left it in chapter 3, with equations 3.14–3.19:

$$\frac{dE_y}{dz} = i\omega\mu H_x \tag{A.1}$$

$$\frac{dE_x}{dz} - \frac{dE_z}{dx} = -i\omega\mu H_y \tag{A.2}$$

$$\frac{dE_y}{dx} = -i\omega\mu H_z \tag{A.3}$$

$$\frac{dH_y}{dz} = -i\omega\epsilon E_x \tag{A.4}$$

$$\frac{dH_x}{dz} - \frac{dH_z}{dx} = i\omega\epsilon E_y \tag{A.5}$$

$$\frac{dH_y}{dx} = i\omega\epsilon E_z, \tag{A.6}$$

where we grouped the vector equations into TE modes (those containing E_y, H_x, H_z) and TM modes (those containing H_y, E_x, E_z). The analysis is very similar for both groups, so here we just consider the TE modes. As we consider propagation in the z-direction, we can replace d/dz by $-ik_z$. We can therefore write the two TE equations A.1 and A.3 as:

$$E_y = -\frac{\omega\mu}{k_z} H_x \tag{A.7}$$

$$\frac{dE_y}{dx} = -i\omega\mu H_z \tag{A.8}$$

As the waveguide is symmetric in x, we can assume that the solutions have either odd or even symmetry in the x-direction, such that:

$$E_y(x, y, t) = E_y(-x, y, t) \quad even \tag{A.9}$$

$$E_y(x,y,t) = -E_y(-x,y,t) \quad odd \tag{A.10}$$

For the even guided modes, we postulate a solution of the form of an exponential decay outside the slab and an oscillatory form within:

$$E_y = Ae^{[-p(|x|-a)-ik_z z]} \quad x \geq |a| \tag{A.11}$$
$$E_y = B\cos(qx)e^{-ik_z z} \quad x \leq |a| \tag{A.12}$$

where p and q are positive real constants to be determined. From equation A.8 we then obtain

$$H_z = \pm\frac{ipA}{\omega\mu}e^{[-p(|x|-a)-ik_z z]} \quad x \geq |a| \tag{A.13}$$
$$H_z = -\frac{iqB}{\omega\mu}\sin(qx)e^{-ik_z z} \quad x \leq |a| \tag{A.14}$$

where the + sign in the top equation is used for $x \leq -d$ and the − sign for $x \geq d$. The tangential field components, E_y and H_Z, should be continuous at the slab boundary, $x = |a|$ and from equations A.11–A.14 we obtain

$$A = B\cos(qa) \tag{A.15}$$
$$pA = qB\sin(qa) \tag{A.16}$$

and then

$$pa = qa\tan(qa) \tag{A.17}$$

The above equation gives us one condition on the values of p and q. To obtain a second condition, we note that our postulated solutions (equations A.11 and A.12) must obey the wave equation (A.18), repeated here:

$$\frac{d^2E(x,y)}{dx^2} + (\frac{n_i^2\omega^2}{c^2} - k_z^2)E(x,y) = 0 \qquad n_i = \begin{cases} n_1, & x > |a| \\ n_2, & x < |a| \end{cases} \tag{A.18}$$

Combining these equations, we obtain:

$$k_z^2 = \frac{n_2^2\omega^2}{c^2} - q^2 \tag{A.19}$$
$$k_z^2 = \frac{n_1^2\omega^2}{c^2} + p^2 \tag{A.20}$$

which further combine to give:

$$(pa)^2 + (qa)^2 = (n_2^2 - n_1^2)\frac{\omega^2 a^2}{c^2} \tag{A.21}$$

which is the equation of a circle in the $pa - qa$ plane with radius $\sqrt{n_2^2 - n_1^2}\frac{\omega a}{c}$. This is the second condition imposed on p and q. The easiest way to demonstrate the discrete nature of the guided modes is to consider the graphical solution of equations A.17 and A.21 as in figure A.1. For a fixed ω, n_1, n_2 and a equation A.21 forms a circle and the intersection of this circle with equationeq:tan corresponds to an even guided mode. In figure A.1 we have plotted equation A.17 (blue lines) and equation A.21 (red circles) for $\sqrt{n_2^2 - n_1^2}\frac{\omega a}{c}$ equal to 1–6. Also shown are the odd mode solutions, these take a $\cot(qa)$ form and are the green lines in the figure. Increasing the frequency, ω, is equivalent to increasing the radius of the circle, which will in turn increase the number of supported modes. Increasing a and $n_2 - n_1$ has a similar effect.

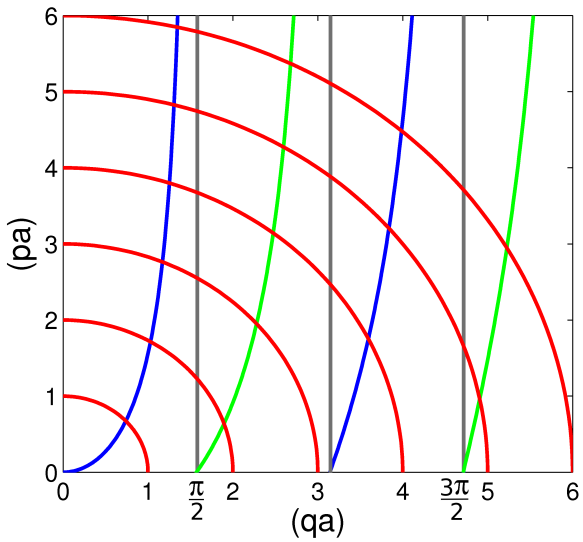

Fig. A.1: Graphical solution for guided modes of a slab waveguide. The circles of increasing radius correspond to equation A.21 with $\sqrt{n_2^2 - n_1^2}\frac{\omega a}{c}$ set to 1, 2, 3, 4, 5 and 6. The blue and green lines correspond to even and modes respectively.

B. PHOTONIC CRYSTAL LASER RECIPE

This appendix is meant to be a step-by-step guide for any member of the microphotonics research group wishing to continue my research. I have tried to be as detailed as possible, but feel free to contact me with any uncertainties at **stephenmoore730@googlemail.com**.

HSQ Deposition

This recipe creates a layer of HSQ approximately 400 nm thick. A slightly thicker layer would be more desireable for deeper CAIBE etching.

- Clean a quarter of a quantum-dot wafer in acetone and rinse in IPA.
- Spin coat a layer of FOX-14 HSQ @ 1000 rpm for 60 s.
- Bake @ 180^{o}C for 5 mins, then 300^{o}C for 5 mins, then 450^{o}C for 3 hours.
- Ramp Temperature back down to 100^{o}C and remove sample.

E-Beam Lithography Pattern Exposure

GDSII patterns, MATLAB scripting files and proximity correction parameters are available on XTAL in folder \ ∼data\STEVEM\W3\Passive Devices\Imp Files.

- Cleave approximately 6 mm×6 mm piece of HSQ coated wafer.
- Clean in acetone and rinse in IPA.
- Spin Coat a layer of undiluted ZEP @ 3250 rpm for 60 s.
- Bake @ 180^{o}C for 10 mins in darkness.

- Continue to keep sample in darkness until after CAIBE etch step.
- Expose layers 0 and 1 with a 7.5 μm aperture, base dose=55 μAscm^{-2}, dose factor=0.75, step size=10 nm, settling times=1 ms, write field size=50 μm, free metric exposure raster=1 nm.
- Expose layers 2 and 3 with a 30 μm aperture, base dose=55 μAscm^{-2}, dose factor=0.9, step size=100 nm, settling times=1 ms, write field size=50 μm, free metric exposure raster=1 nm.
- Write field alignment should be performed for both apertures on the same feature without moving the sample stage.
- Develop in xylene @ 23.4^{o}C for 45 s and rinse in IPA.(Do NOT use ultrasonic bath)

Pattern Transfer to HSQ with RIE Etch

With the chamber empty, run the following cleaning plasmas:

- flow=200 sccm H_2, 200 sccm Ar, power=100 W, pressure=1$\times$10^{-1} mBarr, ring=0, time=5 mins.
- flow=200 sccm O_2, power=100 W, pressure=1$\times$10^{-1} mBarr, ring=0, time=5 mins.

Load sample and perform the following HSQ etch:

- Allow base pressure to reach 3$\times$10^{-6} mBarr.
- flow=200 sccm CHF_3, power=41 W, pressure=4$\times$10^{-2} mBarr, ring=0, time=25 mins[1].

Pattern Transfer to Quantum-dot Material with CAIBE Etch

- Load sample so that photonic crystals are furthest away from exchange chamber. Etch rate is faster closer to the exchange chamber, so this orientation prevents damage of crystal when HSQ mask is worn away.

[1] Time will vary for new layers of HSQ depending on exact thickness.

- Heat sample stage to 115 ^{o}C on external hotplate in wetdeck (yellow light) and quickly transfer to CAIBE.
- Allow sample stage temperature to climb above 125^{o}C and fall back.
- When temperature drops to 125^{o}C, begin etch.
- Etch conditions: flow= 250 sccm Ar, 360 sccm Cl, beam voltage=600 kV, beam current=10 mA, acceleration ratio=0.25. (Recipe 7)
- Aim for an etch time of 20 mins, although the current HSQ thickness will allow slightly less than this. After 15 mins of etching, observe sample through left hand window of CAIBE every 30 seconds and end etch when dark area begins to form on right hand side of sample (near the exchange chamber). Final colour changes are blue–yellow–black.

Second e-beam Exposure

- Clean bottom surface of sample with acetone to remove remnants of thermal paste.
- Spin coat SU8 1:1 (2050:2000.5) @ 5000 rpm for 60s.
- Bake @ 100^{o}C for 60s. Keep sample in darkness until after development.
- Expose layer 4[2] of pattern with a 10 μm aperture, base dose=2 μAscm^{-2}, dose factor=1.0, step size=100 nm, write field size of 100 μm, using an overlay exposure (align to marks from first exposure).
- Post exposure bake @ 100^{o}C for 60 s.
- Develop in EC solvent for 60 s and rinse in IPA.

[2] Layer 4 is not included in the scripting file and needs added to each pattern. Also leave a ∼100 nm gap between the mesa edges and the layer 4 polygon. The low resolution of SU8 will mean the insulation still overlaps the mesa but not completely overlap the narrowest part of the taper.

Gain–Absorber Divider Etch

- Spin coat SR1805 @ 5000 rpm for 60s and bake @ 100^{o}C for 60s.
- Use mask aligner to expose a 50 μm window perpendicular to the waveguides approximately 200 μm[3] from the photonic crystal mirrors. Exposure time=9.5 s.
- Develop for 30 s in MF319 developer and rinse in DI water.
- RIE etch remaining HSQ from windowed part of mesa with flow = 200sccm CHF_3, power=19 W, pressure=4×10^{-2} mBarr, ring=0. time=5 mins[4].
- CAIBE etch with flow = 500sccm Ar, 250sccm Cl, beam voltage=350 kV, beam current=10 mA, acceleration ratio=0.25, temperature=120^{o}C, time=1 min[5].
- Wash SR1805 resist away with acetone. Use O_2 RIE etch if necessary as HSQ should protect sample.
- Remove remaining HSQ mask from mesas with same RIE recipe as 3 steps above.

Electrical Contacts

This recipe is for photolithography defined windows, however e-beam lift-off with PMMA could be used for a specific contact window.

- Spin coat LOR7B @ 4000 rpm and bake @ 180^{o}C for 5 mins on hotplate.
- Spin coat SR1818 @ 5000 rpm and bake @ 180^{o}C for 1 min on hotplate.
- Align separated 50μ contact windows to waveguides and divider using mask aligner. Expose for 50 s.
- Develop in MF319 for 60 s and rinse in DI water.
- Dip in 1:1 HCl:DI water for 60 s.

[3] This distance has not been optimised.
[4] adjust time depending on how much HSQ is left (pale yellow requires ∼5 mins.
[5] This time should be reoptimised.

- Load into e-beam evaporator. After pumping evaporate 20 nm Ni and 200 nm Au.
- Soak in acetone for 5 mins before agitating with plastic pipette to perform lift-off.
- Dip in 1:1 HCl:DI water for 60 s.
- Load into evaporator and evaporate 14 nm Au, 14 nm Ge, 14 nm Au, 11 nm Ni, 200nm Au.
- Cleave non-crystal end of sample and test.

BIBLIOGRAPHY

[1] R. H. Hall, G. E. Fenner, J. D. Kingsley, T. J. Soltys and R. O. Carlson, "Coherent Light Emission from GaAs Junction," *Physics Review Letters*, volume 9, p. 366, 1962.

[2] N. H. Jr and S. F. Bevacgua, "Coherent (visible) Light Emission from $Ga(As_{1-x}P_x)$ Junctions," *Applied Physics Letters*, volume 1, p. 83, 1962.

[3] M. I. Nathan, A. A. Rogachev, S. M. Ryvkin and B. V. Tsarenkov, "Recombination Radiation of Gallium Arsenic," *Soviet Physics of Solid State*, volume 4, p. 782, 1962.

[4] T. F. Krauss, R. M. D. L. Rue and S. Brand, "Two-dimensional photonic-bandgap structures operating at near-infrared wavelengths," *Nature*, volume 383, pp. 699–702, 1996.

[5] J. O'Brien, O. Painter, R. Lee, C. C. Cheng, A. Yariv and A. Scherer, "Lasers incorporating 2D photonic bandgap mirrors," *Electronics Letters*, volume 32, pp. 2243–2244, 1996.

[6] B. DUrso, O. Painter, J. OBrien, T. Tombrello, A. Yariv, and A. Scherer, "Modal reflectivity in finite-depth two-dimensional photonic-crystal microcavities," *Journal of Optical Society of America B*, volume 15, pp. 1155–1159, 1998.

[7] T. F. Krauss, O. Painter, A. Scherer, J. S. Roberts and R. M. D. L. Rue, "Photonic microstructures as laser mirrors," *Optical Engineering*, volume 37, pp. 1143–1148, 1998.

[8] T. D. Happ, M. Kamp, F. Klopf and A. Forchel, "Single mode lasers based on monolithic integration of ridge waveguides with 2D photonic

crystal waveguides," *Optical and Quantum Electronics*, volume 34, pp. 1137–1144, 2002.

[9] A. Talneau, L. LeGratiet, J. L. Gentner, A. Berrier, M. Mulot, S. Anand and S. Olivier, "High external efficiency in a monomode full-photonic-crystal laser under continuous wave electrical injection," *Applied Physics Letters*, volume 85, pp. 1913–1915, 2004.

[10] X. Checoury, P. Crozat, J.-M. Lourtioz, C. Cuisin, E. Derouin, O. Drisse, F. Poigt, L. Legouezigou, O. Legouezigou, P. Pommereau, G.-H. Duan, O. Gauthier-Lafaye, S. Bonnefont, D. Mulin, F. Lozes-Dupuy and A. Talneau, "Single-mode in-gap emission of medium-width photonic crystal waveguides on InP substrate," *Optics Express*, volume 13, pp. 6947–6955, 2005.

[11] O. Painter, R. K. Lee, A. Scherer, A. Yariv, J. D. O'Brien, P. D. Dapkus and I. Kim, "Two-Dimensional Photonic Band-Gap Defect Mode Laser," *Science*, volume 284, pp. 1819–1821, 1999.

[12] J. OBrien, W. Kuang, P.-T. Lee, J. R. Cao, C. Kim and W. Kim, "Photonic Crystal Lasers," *Encyclopedia of Nanoscience and Technology*, volume 8, pp. 1–12, 2004.

[13] L. A. Coldren and S. W. Corzine, *Diode Lasers and Photonic Integrated Circuits*, Wiley: New York, 1995.

[14] H. Y. Ryu, J. K. Hwang, D. S. Song, I. Y. Han, Y. H. Lee and D. H. Jang, "Effect of nonradiative recombination on light emitting properties of two-dimensional photonic crystal slab structures," *Applied Physics Letters*, volume 78, pp. 1174–1176, 2001.

[15] D. Ouyang, N. N. Ledenstov, D.Bimberg, A. V. Kovsh, A. E. Zhukov, S. S. Mikhrin and V. M. Ustinov, "High Performance Narrow Stripe Quantum-dot Lasers with Etched Waveguide," *Semiconductor Science and Technology*, volume 18, 2003.

[16] M. Kuntz, M. Lammlin, D. Bimberg, M. G. Thompson, K. T. Tan, C. Marinelli, R. V. Penty, I. H. White, V. M. Ustinov, A. E. Zhukov,

Y. M. Shernyakov and A. R. Kovsh, "35 Ghz Mode-locking of 1.3 μm Quantum-dot Lasers," *Applied Physics Letters*, volume 85, pp. 843–845, 2004.

[17] P. Vasil'ev, *Ultrafast Diode Lasers: Fundamentals and Applications*, Artech House, 1995.

[18] E. U. Rafailov, M. A. Cataluna, W. Sibbett, N. D. Ilinskaya, Y. M. Zadiranov, A. E. Zhukov and V. M. Ustinov, "High-power picosecond and femtosecond pulse generation from a two-section mode-locked quantum-dot laser," *Applied Physics Letters*, volume 87, p. 081107, 2005.

[19] U. Morgner, F. X. Kartner, S. H. Cho, Y. Chen, H. A. Haus, J. G. Fujimoto and E. P. Ippen, "Sub-two-cycle pulses from a Kerr-lens mode-locked Ti:sapphire laser," *Optics Letters*, volume 24, pp. 411–413, 1999.

[20] R. S. Tucker, U. Koren, G. Raybon, C. A. Burrus, B. . Miller, T. L. Koch and G. Eisenstein, "40GHz active mode-locking in a 1.5μm monolithic extended-cavity laser," *Electronics Letters*, volume 25, pp. 621–622, 1989.

[21] S. Arahira, Y. Matsui, and Y. Ogawa, "Mode-Locking at Very High Repetition Rates More than Terahertz in Passively Mode-Locked Distributed-Bragg-Reflector Laser Diodes," *IEEE Journal of Quantum Electronics*, volume 32, pp. 1211–1224, 1996.

[22] P. A. Morton, J. E. Bowers, L. A. Koszi, M. Soler, J. Lopata and D. P. Wilt, "Monolithic hybrid mode-locked 1.3 μm semiconductor lasers," *Applied Physics Letters*, volume 56, pp. 111–113, 1990.

[23] C. Harder, J. S. Smith, K. Y. Lau and A. Yariv, "Passive mode locking of buried heterostructure lasers with nonuniform current injection," *Applied Physics Letters*, volume 42, pp. 772–774, 1983.

[24] E. U. Rafailov, M. A. Cataluna and W. Sibbett, "Mode-locked quantum-dot lasers," *Nature Photonics*, volume 1, pp. 395–401, 2007.

[25] A. E. Siegman, *Lasers*, University Science Books, 1986.

[26] M. G. Thompson, A. Rae, R. L. Sellin, C. Marinelli, R. V. Penty, I. H. White, A. R. Kovsh, S. S. Mikhrin, D. A. Livshits and I. L. Krestnikov, "Subpicosecond high-power mode locking using flared waveguide monolithic quantum-dot lasers," *Applied Physics Letters*, volume 88, p. 133119, 2006.

[27] G. H. C. New, "Mode-locking of quasi-continuous lasers," *Optics Communications*, volume 6, pp. 188–192, 1972.

[28] D. J. Derickson, R. J. Helkey, A. Mar, J. R. Karin, J. G. Wasserbauer and J. E. Bowers, "Short Pulse Generation Using Multisegment Mode-Locked Semconductor Lasers," *IEEE Journal of Quantum Electronics*, volume 28, pp. 2186–2202, 1992.

[29] J. Yu, M. Schell, M. Schulze and D. Bimberg, "Generation of 290 fs pulses at 1.3 μm by hybrid mode-locking of a semiconductor laser and optimization of the time-bandwidth product," *Applied Physics Letters*, volume 65, pp. 2395–2397, 1994.

[30] P. J. Delfyett, L. Florez, N. Stoffel, T. Gmitter, N. Andreadakis, G. Alphonse and W. Ceislik, "200 fs optical pulse generation and intracavity pulse evolution in a hybrid mode-locked semiconductor diode-laser/amplifier system," *Optics Letters*, volume 17, pp. 670–672, 1992.

[31] J. D. Joannopoulos, *Photonic Crystals: Molding the Flow of Light*, Princeton University Press, 1995.

[32] K. Sakoda, *Optical Properties of Photonic Crystals*, Springer, 2001.

[33] A. Yariv, *Optical Electronics in Modern Communications*, Oxford University Press, 5 edition, 1997.

[34] C. Kittel, *Introduction to Solid State Physics*, Wiley [New York], 2005.

[35] Y. Akahane, T. Asano, B. S. Song and S. Noda, "High-Q photonic nanocavity in a two-dimensional photonic crystal," *Nature*, volume 425, pp. 944–947, 2003.

[36] B. S. Song, S. Noda, T. Asano and Y. Akahane, "Ultra-high-Q photonic double-heterostrucure nanocavity," *Nature Materials*, volume 4, pp. 207–210, 2005.

[37] Y. A. Vlasov, M. O'Boyle, H. F. Hamann and S. J. McNab, "Active control of slow light on a chip with photonic crystal waveguides," *Nature*, volume 438, pp. 65–69, 2005.

[38] C. Dix, P. G. Flavin, P. Hendy and M. E. Jones, "0.1 μm Scale Lithography using a Conventional Electron Beam System," *Journal of Vacuum Science and Technology B*, volume 3, pp. 131–135, 1985.

[39] L. Stevens, R. Jonckheere, E. Froyen, S. Decoutere and D. Lanneer, "Determination of Proximity Correction Parameters using the Doughnut Method," *Microelectronic Engineering*, volume 5, pp. 141–150, 1986.

[40] S. V. Dubonos, B. N. Gaifullin, H. F. Raith, A. A. Svintsov and S. I. Zaitsev, "Evaluation, Verification and Error Determination of Proximity Parameters α, β and η in Electron Beam Lithography," *Microelectronic Engineering*, volume 21, pp. 293–296, 1993.

[41] L. O'Faolain, M. V. Kotlyar, N. Tripathi, R. Wilson and T. F. Krauss, "Fabrication of Photonic Crystals using a Spin-coated Hydrogen Silsesquioxane Hard Mask," *Journal of Vacuum Science and Technology B*, volume 22, pp. 336–339, 2006.

[42] J. D. Thomson, H. D. Summers, P. J. Hulyer, P. M. Smowton and P. Blood, "Determination of single-pass optical gain and internal loss using a multisection device," *Applied Physics Letters*, volume 75, pp. 2527–2529, 1999.

[43] Z. I. Alferov and R. F. Kazarinov, "Semiconductor Lasers with Electrical Pumping," *Inventors Certificate No. 181737*, 1963.

[44] H. Kroemer, "A Proposed Class of Heterojunction Injection Lasers," *Proc. IEEE*, volume 51, p. 1782, 1963.

[45] Z. I. Alferov, V. M. Andreev, D. Z. Garbuzov, Y. V. Zhilyaev, E. Morozov, E. L. Portnoi and V. G. Trofim, "Investigation of the influence of the

AlAs-GaAs heterostructure parameters on the laser threshold current and realization of continuous emission at room temperature," *Soviet Physics of Semiconductors*, volume 4, p. 1573, 1971.

[46] Z. I. Alferov, V. M. Andreev, V. I. Korol'kov, D. N. Trat'yakov and V. M. Tuchkevich, "High Voltage p-n junctions in $Ga_xAl1 - xAs$ Crystals," *Soviet Physics of Semiconductors*, volume 1, p. 1313, 1968.

[47] H. S. Rupprecht, J. M. Woodall and G. D. Pettit, "Efficient Visible Electroluminescence at 300K from $Ga_{1-x}Alx$As p-n Junctions Grown by Liquid Phase Epitaxy," *Applied Physics Letters*, volume 11, p. 81, 1967.

[48] W. T. Tsang, "Extremely low threshold (AlGa)As graded-index waveguide seperate confinement heterostructure lasers grown by molecular beam epitaxy," *Applied Physics Letters*, volume 40, p. 217, 1982.

[49] A. Y. Cho, "Film deposition by molecular beam techniques," *Journal of Vacuum Science and Technology*, volume 8, p. 31, 1971.

[50] M. Asada, Y. Miyamoto and Y. Suematsu, "Gain and the threshold of three-dimensional quantum-box lasers," *IEEE Journal of Quantum Electronics*, volume QE-22, pp. 1915–1921, 1986.

[51] N. N. Ledentsov, V. M. Ustinov, A. Y. Egorov, A. E. Zhukov, M. V. Maximov, I. G. Tabatadze and P. S. Kop'ev, "Optical properties of heterostructures with InGaAs–GaAs quantum clusters," *Semiconductors*, volume 28, pp. 832–834, 1994.

[52] E. P. O'Reilly, *Quantum Theory of Solids*, CRC Press, 2002.

[53] N. N. Ledentsov, M. Grundmann, F. Heinrichsdorff, D. Bimberg, V. M. Ustinov, A. E. Zhukov, M. V. Maximov, Z. I. Alferov and J. A. Lott, "Quantum-Dot heterostrucure lasers," *IEEE Journal of Selected Topics in Quantum Electronics*, volume 6, pp. 439–451, 2000.

[54] G. T. Liu, H. Li, K. J. Malloy and L. F. Lester, "Extremely low room temperature threshold current density diode lasers using InAs dots in $In_{0.15}Ga_{0.85}$As quantum well," *Electronics Letters*, volume 35, pp. 1163–1164, 1999.

[55] N. N. Ledentsov, J. Bohrer, D. Bimberg, S. V. Zaitsev, V. M. Ustinov, Y. Egorov, A. E. Zhukov, M. V. Maximov, P. S. Kop'ev, Z. I. Alferov, A. O. Kosogov, U. Gosele and S. S. Ruvimov, "3D arrays of quantum-dots for laser applications," *Material Research Society Symposium Proceedings*, volume 421, 1996.

[56] J. Bohrer, I. V. Kochnev, Y. M. Shernyakov, S. V. Zaitsev, N. Y. Gordeev, A. F. Tsatsul'nikov, A. V. Sakharov, I. L. Krestnikov, P. S. Kop'ev, Z. I. Alferov, N. N. Ledentsov, D. Bimberg, A. O. Kosogov, P. Werner and U. Gosele, "InGaAs/GaAs quantum dot lasers with ultra high characteristic temperature (T_o = 385 K) grown by metal organic chemical vapor deposition," *Japanese Journal of Applied Physics*, volume 36, pp. 4221–4223, 1997.

[57] P. Borri1, S. Schneider, W. Langbein and D. Bimberg, "Ultrafast carrier dynamics in InGaAs quantum dot materials and devices," *JOURNAL OF OPTICS A*, volume 8, pp. S33–S46, 2006.

[58] E. U. Rafailov, S. J. White, A. A. Lagatsky, A. Miller, W. Sibbett, D. A. Livshits, A. E. Zhukov and V. M. Ustinov, "Fast Quantum-Dot Saturable Absorber for Passive Mode-Locking of Solid-State Lasers," *Photonics Technology Letters*, volume 16, pp. 2439–2441, 2004.

[59] D. B. Malins, A. Gomez-Iglesias, S. J. White, W. Sibbett, A. Miller and E. U. Rafailov, "Ultrafast electroabsorption dynamics in an InAs quantum dot saturable absorber at 1.3 μm," *Applied Physics Letters*, volume 89, p. 171111, 2006.

[60] T. C. Newell, D. J. Bossert, A. Stintz, B. Fuchs, K. J. Malloy and L. F. Lester, "Gain and Linewidth Enhancement Factor in InAs Quantum-Dot Laser Diodes," *Photonics Technology Letters*, volume 11, pp. 1527–1529, 1999.

[61] A. Markus, J. X. Chen, O. Gauthier-Lafaye, J. G. Provost, C. Paranthoen and A. Fiore, "Impact of intraband relaxation on the performance of a quantum-dot laser," *IEEE Journal of Selected Topics in Quantum Electronics*, volume 9, pp. 1308–1314, 2003.

[62] M. Gioannini and I. Montrosset, "Numerical Analysis of the Frequency Chirp in Quantum-Dot Semiconductor Lasers," *IEEE Journal of Quantum Electronics*, volume 43, pp. 941–949, 2007.

[63] M. A. Cataluna, E. U. Rafailov, A. D. McRobbie, W. Sibbett, D. A. Livshits and A. R. Kovsh, "Stable Mode-Locked Operation up to 80 ^{o}C From an InGaAs Quantum-Dot Laser," *Photonics Technology Letters*, volume 18, pp. 1500–1502, 2006.

[64] S. A. Moore, L. O'Faolain, M. A. Cataluna, M. B. Flynn, M. V. Kotlyar and T. F. Krauss, "Reduced surface sidewall recombination and diffusion in quantum dot lasers," *Photonics Technology Letters*, volume 18, pp. 1861–1863, 2006.

[65] A. Oster, G. Erbert and H. Wenzel, "Gain spectra measurements by a variable stripe length method with current injection," *Electronics Letters*, volume 33, pp. 864–865, 1997.

[66] M. V. Kotlyar, L. O'Faolain, R. Wilson and T. F. Krauss, "Hogh-aspect-ratio chemically assisted ion beam etching for photonic crystals using a high beam voltage-current ratio," *Journal of Vacuum Science and Technology B*, volume 22, pp. 1788–1791, 2004.

[67] P. McIlroy, A. Kurobe and Y. Uematsu, "Analysis and Application of Theoretical Gain Curves to the design of Multi-quantum-well lasers," *IEEE Journal of Quantum Electronics*, volume 21, pp. 1958–1963, 1985.

[68] M. V. Kotlyar, T. Karle, M. D. Settle, L. O'Faolain and T. F. Krauss, "Low-loss Photonic Crystal Defect Waveguides in InP," *Applied Physics Letters*, volume 84, pp. 3588–3590, 2004.

[69] H. Hillmer, A. Forchel, S. Hansmann, M. Morohashi, E. Lopez, H. P. Meier and K. Ploog, "Optical Investigations on the Mobility of two-dimensional Excitons in GaAs/GaAlAs Quantum-wells," *Physical Review B*, volume 39, pp. 10901–10912, 1989.

[70] M. Sugawara, K. Mukai, Y. Nakata, H. Ishikawa and A. Sakamoto, "Effect of Homogeneous Broadening of Optical Gain on Lasing Spectra in Self-

assembled InGaAs Quantum-dot Lasers," *Physical Review B*, volume 61, pp. 7595–7603, 2000.

[71] D. P. Popescu, P. G. Eliseev, A. Stintz and K. J. Malloy, "Carrier Migration in Structures with InAs Quantum-dots," *Journal of Applied Physics*, volume 94, pp. 2454–2458, 2003.

[72] M. L. Povinelli, S. G. Johnson and J. D. Joannopoulos, "Slow-light, band-edge waveguides for tunable time delays," *Optics Express*, volume 13, pp. 7145–7159, 2005.

[73] T. Segawa, S. Matsuo, Y. Ohiso, T. Ishii, Y. Shibata and H. Suzuki, "Fast tunable optical filter using cascaded Mach-Zehnder Interferometers with apodized sampled gratings," *Photonics Technology Letters*, volume 17, pp. 139–141, 2005.

[74] S.-H. Jeong, H.-C. Kim, T. Mizumoto, J. Wiedmann, S. Arai, M. Takenaka and Y. Nakano, "Polarization-independent all-optical switching in a nonlinearGaInAsP-InP highmesa waveguide with a vertically etched Bragg reflector," *Journal of Quantum Electronics*, volume 38, pp. 706–714, 2002.

[75] T. Segawa, S. Matsuo, Y. Ohiso, T. Ishii and H. Suzuki, "Apodised sampled grating using InGaAsP/InP deep-ridge waveguide with vertical-groove surface grating," *Electronics Letters*, volume 40, pp. 804–805, 2004.

[76] H. C. Kim, J. Weidmann, J. Matsui, K. Tamura and S. Arai, "1.5μm wavelength distributed feedback lasers with deeply etched first-order vertical gratings," *Japanese Journal of Applied Physics*, volume 40, pp. L1107–L1109, 2001.

[77] C. L. Timmons, *Fluorocarbon Post-Etch Residue Removal Using Radical Anion Chemistry*, Georgia Institute of Technology, 2004.

[78] C. J. M. Smith, H. Benisty, S. Olivier, M. Rattier, C. Weisbuch, T. F. Krauss, R. M. D. la Rue, R. Houdre and U. Oesterle, "Low-loss channel waveguides with two-dimensional photonic crystal boundaries," *Applied Physics Letters*, volume 77, pp. 2813–2815, 2000.

[79] S. Olivier, H. Benisty, C. Weisbuch, C. J. M. Smith, T. F. Krauss and R. Houdre, "Coupled-mode theory and propagation losses in photonic crystal waveguides," *Optics Express*, volume 11, pp. 1490–1496, 2003.

[80] S. Olivier, M. Rattier, H. Benisty, C. Weisbuch, C. J. M. Smith, R. M. D. L. Rue, T. F. Krauss, U. Oesterle and R. Houdre, "Mini-stopbands of a one-dimensional system: The channel waveguide in a two-dimensional photonic crystal," *Physical Review B*, volume 63, p. 113311, 2001.

[81] S. G. Johnson and J. D. Joannopoulos, "Block-iterative frequency-domain methods for Maxwell's equations in a planewave basis," *Optics Express*, volume 8, pp. 173–195, 2001, http://www.opticsexpress.org/abstract.cfm?URI=OPEX-8-3-173.

[82] S. A. Moore, L. OFaolain, T. P. White and T. F. Krauss, "Photonic crystal laser with mode selective mirrors," *Optics Express*, volume 16, pp. 1365–1370, 2008.

[83] M. V. Maximov, L. V. Asryan, Y. M. Shernyakov, A. F. Tsatsul'nikov, I. N. Kaiander, V. V. Nikolaev, A. R. Kovsh, S. S. Mikhrin, V. M. Ustinov, A. E. Zhukov, Z. I. Alferov, N. N. Ledenstov and D. Bimberg., "Gain and threshold characterisitcs of long wavelength lasers based on InAs/GaAs quantum dots formed by activated allow phase separation," *IEEE Journal of Quantum Electronics*, volume 37, pp. 676–683, 2000.

[84] A. E. Vasdekis, S. A. Moore, A. Ruseckas, T. F. Krauss, I. D. W. Samuel and G. A. Turnbull, "Silicon based organic semiconductor laser," *Applied Physics Letters*, volume 91, p. 051124, 2007.

[85] O. and B. Jalali, "Demonstration of a silicon Raman laser," *Optics Express*, volume 12, pp. 5269–5273, 2004.

[86] H. Rong, R. Jones, A. Liu, O. Cohen, D. Hak, A. Fang and M. Paniccia, "A continuous-wave Raman silicon laser," *Nature*, volume 433, pp. 725–728, 2005.

[87] S. Cloutier, P. A. Kossyrev and J. Xu, "Optical gain and stimulated emission in periodic nanopatterned crystalline silicon," *Nature Materials*, volume 4, pp. 887–891, 2005.

[88] H. Ennen, G. Pomrenke, A. Axmann, K. Eisele, W. Haydl and J. Schneider, "1.54-m electroluminescence of erbium-doped silicon grown by molecular beam epitaxy," *Applied Physics Letters*, volume 46, pp. 381–383, 1985.

[89] A. W. Fang, H. Park, O. Cohen, R. Jones, M. J. Paniccia and J. E. Bowers, "Electrically pumped hybrid AlGaInAs-silicon evanescent laser," *Optics Express*, volume 14, pp. 9203–9210, 2006.

[90] A. E. Vasdekis, G. Tsiminis, J.-C. Ribierre, L. O. Faolain, T. F. Krauss, G. A. Turnbull and I. D. W. Samuel, "Diode pumped distributed Bragg reflector lasers based on a dye-to-polymer energy transfer blend," *Optics Express*, volume 14, pp. 9211–9216, 2006.

[91] G. E. J. Jr. and F. A. Modine, "Optical absorption of silicon between 1.6 and 4.7 eV at elevated temperatures," *Applied Physics Letters*, volume 41, pp. 180–182, 1982.

[92] "Silicon/organic hybrid laser produces red light," *Laser Focus World*, volume 43, pp. 37–41, Oct 2007.

[93] "Organic semiconductors aid quest for silicon laser," *Optics & Lasers Europe*, volume 154, pp. 21–24, Oct 2007.